A PANCHROMATIC VIEW OF THE RESTLESS SN 2009ip REVEALS THE EXPLOSIVE EJECTION OF A MASSIVE STAR ENVELOPE

Citation: Margutti, R., D. Milisavljevic, A. M. Soderberg, R. Chornock, B. A. Zauderer, K. Murase, C. Guidorzi, et al. "A PANCHROMATIC VIEW OF THE RESTLESS SN 2009ip REVEALS THE EXPLOSIVE EJECTION OF A MASSIVE STAR ENVELOPE." The Astrophysical Journal 780, no. 1 (December 10, 2013): 21. © 2014 The American Astronomical Society

As Published: http://dx.doi.org/10.1088/0004-637x/780/1/21

Publisher: IOP Publishing

Persistent URL: http://hdl.handle.net/1721.1/92944

Version: Final published version: final published article, as it appeared in a journal, conference proceedings, or other formally published context

The Astrophysical Journal, 780:21 (38pp), 2014 January 1 doi:10.1088/0004-637X/780/1/21

A PANCHROMATIC VIEW OF THE RESTLESS SN 2009ip REVEALS THE EXPLOSIVE EJECTION OF A MASSIVE STAR ENVELOPE

R. Margutti[1], D. Milisavljevic[1], A. M. Soderberg[1], R. Chornock[1], B. A. Zauderer[1], K. Murase[2], C. Guidorzi[3], N. E. Sanders[1], P. Kuin[4], C. Fransson[5], E. M. Levesque[6], P. Chandra[7], E. Berger[1], F. B. Bianco[8], P. J. Brown[9], P. Challis[7], E. Chatzopoulos[10], C. C. Cheung[11], C. Choi[12], L. Chomiuk[14,13,34], N. Chugai[15], C. Contreras[16], M. R. Drout[1], R. Fesen[17], R. J. Foley[1], W. Fong[1], A. S. Friedman[1,18], C. Gall[19,20], N. Gehrels[20], J. Hjorth[19], E. Hsiao[21], R. Kirshner[1], M. Im[12], G. Leloudas[19,22], R. Lunnan[1], G. H. Marion[1], J. Martin[23], N. Morrell[21], K. F. Neugent[24], N. Omodei[25], M. M. Phillips[21], A. Rest[26], J. M. Silverman[10], J. Strader[13], M. D. Stritzinger[27], T. Szalai[28], N. B. Utterback[17], J. Vinko[10,28], J. C. Wheeler[10], D. Arnett[29], S. Campana[30], R. Chevalier[31], A. Ginsburg[6], A. Kamble[1], P. W. A. Roming[32,33], T. Pritchard[33], and G. Stringfellow[6]

[1] Harvard-Smithsonian Center for Astrophysics, 60 Garden St., Cambridge, MA 02138, USA
[2] Institute for Advanced Study, Princeton, NJ 08540, USA
[3] Department of Physics, University of Ferrara, via Saragat 1, I-44122 Ferrara, Italy
[4] University College London, MSSL, Holmbury St. Mary, Dorking, Surrey RH5 6NT, UK
[5] Department of Astronomy and the Oskar Klein Centre, Stockholm University, AlbaNova, SE-106 91 Stockholm, Sweden
[6] CASA, Department of Astrophysical and Planetary Sciences, University of Colorado, 389-UCB, Boulder, CO 80309, USA
[7] National Centre for Radio Astrophysics, Tata Institute of Fundamental Research, Pune University Campus, Ganeshkhind, Pune 411007, India
[8] Center for Cosmology and Particle Physics, New York University, 4 Washington Place, New York, NY 10003, USA
[9] George P. and Cynthia Woods Mitchell Institute for Fundamental Physics & Astronomy, Texas A. & M. University, Department of Physics and Astronomy, 4242 TAMU, College Station, TX 77843, USA
[10] Department of Astronomy, University of Texas at Austin, Austin, TX 78712-1205, USA
[11] Space Science Division, Naval Research Laboratory, Washington, DC 20375-5352, USA
[12] CEOU/Department of Physics and Astronomy, Seoul National University, Seoul 151-742, Korea
[13] Department of Physics and Astronomy, Michigan State University, East Lansing, MI 48824, USA
[14] National Radio Astronomy Observatory, P.O. Box O, Socorro, NM 87801, USA
[15] Institute of Astronomy, Russian Academy of Sciences, Pyatnitskaya 48, 119017, Moscow, Russian Federation
[16] Centre for Astrophysics & Supercomputing, Swinburne University of Technology, P.O. Box 218, Hawthorn, VIC 3122, Australia
[17] Department of Physics & Astronomy, Dartmouth College, 6127 Wilder Lab, Hanover, NH 03755, USA
[18] Massachusetts Institute of Technology, 77 Massachusetts Ave., Bldg. E51-173, Cambridge, MA 02138, USA
[19] Dark Cosmology Centre, Niels Bohr Institute, University of Copenhagen, Juliane Maries Vej 30, DK-2100 Copenhagen, Denmark
[20] NASA, Goddard Space Flight Center, 8800 Greenbelt Road, Greenbelt, MD 20771, USA
[21] Carnegie Observatories, Las Campanas Observatory, Colina El Pino, Casilla 601, La Serena, Chile
[22] The Oskar Klein Centre, Department of Physics, Stockholm University, SE-10691 Stockholm, Sweden
[23] Astronomy/Physics MS HSB 314, One University Plaza Springfield, IL 62730, USA
[24] Lowell Observatory, 1400 W Mars Hill Road, Flagstaff, AZ 86001, USA
[25] W. W. Hansen Experimental Physics Laboratory, Kavli Institute for Particle Astrophysics and Cosmology, Department of Physics and SLAC National Accelerator Laboratory, Stanford University, Stanford, CA 94305, USA
[26] Space Telescope Science Institute, 3700 San Martin Dr., Baltimore, MD 21218, USA
[27] Department of Physics and Astronomy, Aarhus University, Ny Munkegade, DK-8000 Aarhus C, Denmark
[28] Department of Optics and Quantum Electronics, University of Szeged, Dóm tér 9., Szeged H-6720, Hungary
[29] Department of Astronomy and Steward Observatory, University of Arizona, Tucson, AZ 85721, USA
[30] INAF/Brera Astronomical Observatory, via Bianchi 46, I-23807 Merate (LC), Italy
[31] Department of Astronomy, University of Virginia, P.O. Box 400325, Charlottesville, VA 22904-4325, USA
[32] Southwest Research Institute, Department of Space Science, 6220 Culebra Road, San Antonio, TX 78238, USA
[33] Department of Astronomy & Astrophysics, Penn State University, 525 Davey Lab, University Park, PA 16802, USA
Received 2013 May 31; accepted 2013 September 26; published 2013 December 10

ABSTRACT

The double explosion of SN 2009ip in 2012 raises questions about our understanding of the late stages of massive star evolution. Here we present a comprehensive study of SN 2009ip during its remarkable rebrightenings. High-cadence photometric and spectroscopic observations from the GeV to the radio band obtained from a variety of ground-based and space facilities (including the Very Large Array, *Swift*, *Fermi*, *Hubble Space Telescope,* and *XMM*) constrain SN 2009ip to be a low energy ($E \sim 10^{50}$ erg for an ejecta mass $\sim 0.5\,M_{\odot}$) and asymmetric explosion in a complex medium shaped by multiple eruptions of the restless progenitor star. Most of the energy is radiated as a result of the shock breaking out through a dense shell of material located at $\sim 5 \times 10^{14}$ cm with $M \sim 0.1\,M_{\odot}$, ejected by the precursor outburst $\sim$40 days before the major explosion. We interpret the NIR excess of emission as signature of material located further out, the origin of which has to be connected with documented mass-loss episodes in the previous years. Our modeling predicts bright neutrino emission associated with the shock break-out if the cosmic-ray energy is comparable to the radiated energy. We connect this phenomenology with the explosive ejection of the outer layers of the massive progenitor star, which later interacted with material deposited in the surroundings by previous eruptions. Future observations will reveal if the massive luminous progenitor star survived. Irrespective of whether the explosion was terminal, SN 2009ip brought to light the existence of new channels for sustained episodic mass loss, the physical origin of which has yet to be identified.

Key words: stars: mass-loss – supernovae: individual (SN2009ip)

Online-only material: color figures

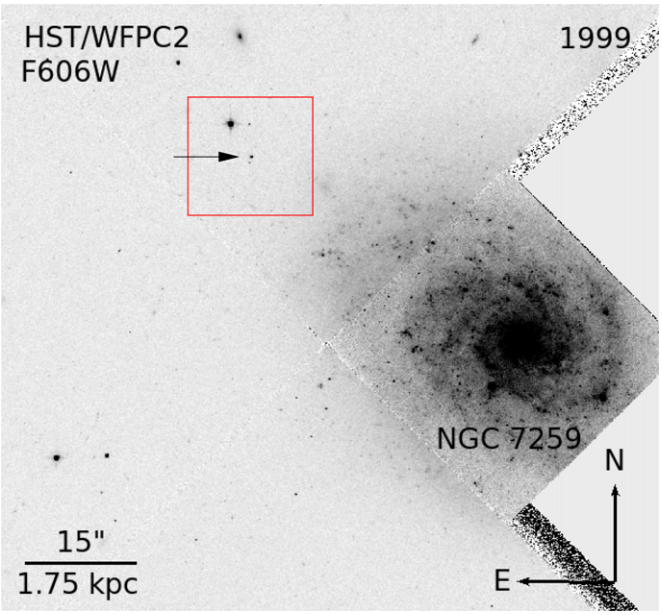

Figure 1. *Hubble Space Telescope* (*HST*) preexplosion image acquired in 1999 (Program 6359; PI: Stiavelli). The location of the progenitor of SN 2009ip is marked by an arrow. SN 2009ip exploded in the outskirts of its host galaxy NGC 7259 at an angular distance of ∼43″.4 from the host center, corresponding to ∼5 kpc.

(A color version of this figure is available in the online journal.)

1. INTRODUCTION

Standard stellar evolutionary models predict massive stars with $M \gtrsim 40\,M_\odot$ to spend half a Myr in the Wolf-Rayet phase before exploding as supernovae (SNe; e.g., Georgy et al. 2012 and references therein). As a result, massive stars are *not* expected to be H rich at the time of explosion. Yet, recent observations have questioned this picture, revealing the limitations of our current understanding of the last stages of massive star evolution and in particular the uncertainties in the commonly assumed mass-loss prescriptions (Humphreys & Davidson 1994; Smith & Owocki 2006). Here, we present observations from an extensive, broadband monitoring campaign of SN 2009ip (Figure 1) during its double explosion in 2012 that revealed extreme mass-loss properties, raising questions about our understanding of the late stages of massive star evolution.

An increasingly complex picture is emerging connecting SN progenitor stars with explosion properties. The most direct link arguably comes from the detection of progenitor stars in preexplosion images. These efforts have been successful connecting Type IIP SNe with the death of red supergiants ($M \sim 8$–$15\,M_\odot$; Smartt 2009). However, massive progenitor stars have proven to be more elusive (e.g., Kochanek et al. 2008): SN 2005gl constitutes the first direct evidence for a massive ($M > 50\,M_\odot$) and H rich star to explode as a core-collapse SN, contrary to theoretical expectations (Gal-Yam et al. 2007, 2009).

SN 2005gl belongs to the class of Type IIn SNe (Schlegel 1990). Their spectra show evidence for strong interaction between the explosion ejecta and a dense circumstellar medium (CSM) previously enriched by mass loss from the progenitor star. In order for the SN to appear as a Type IIn explosion, the mass loss and the core collapse have to be timed, with mass loss occurring in the decades to years before the collapse. This timing requirement constitutes a further challenge to current evolutionary models and emphasizes the importance of the progenitor mass loss in the years before the explosion in determining its observable properties.

Mass loss in massive stars can either occur through steady winds (on typical timescales of 10^4–10^7 yr) or episodic outbursts lasting months to years, as it occurs in luminous blue variable (LBV) stars. The LBV evolutionary state has a typical duration of $\sim 10^4$ yr, and it is characterized by eruptions on timescales of years to decades (see Humphreys & Davidson 1994 for a review). Based on the luminosity of the progenitor star, Gal-Yam et al. (2009) report that the progenitor of SN 2005gl was likely an LBV, thus supporting a connection between SNe IIn and LBVs.[35] On the other hand, there are controversial objects like SN 1961V, highlighting the present difficulty in distinguishing between a giant eruption and a genuine core-collapse explosion even 50 yr after the event (e.g., Van Dyk & Matheson 2012; Kochanek et al. 2011). The dividing line between SNe and impostors can be ambiguous.

Here we report on our extensive multiwavelength campaign to monitor the evolution of SN 2009ip, which offers an unparalleled opportunity to study the effects and causes of significant mass loss in massive stars in real time. Discovered in 2009 (Maza et al. 2009) in NGC 7259 (spiral galaxy with brightness $M_{\rm B} \sim -18$ mag; Lauberts & Valentijn 1989), it was first mistaken as a faint SN candidate (hence the name SN 2009ip). Later observations by Miller et al. (2009), Li et al. (2009), and Berger et al. (2009a) led these authors to associate the variable behavior of SN 2009ip to an LBV state. Preexplosion *Hubble Space Telescope* (*HST*) images constrain the progenitor to be a massive star with $M \gtrsim 60\,M_\odot$ (Smith et al. 2010b; Foley et al. 2011), consistent with an LBV nature. The same studies showed that SN 2009ip underwent multiple explosions in rapid succession in 2009. Indeed, a number of eruptions were also observed in 2010 and 2011: a detailed summary can be found in Levesque et al. (2012), and a historic light-curve is presented by Pastorello et al. (2013). Among the most important findings is the presence of blue-shifted absorption lines corresponding to ejecta traveling at a velocity of 2000–7000 km s^{-1} during the 2009 outbursts (Smith et al. 2010b; Foley et al. 2011), extending to $v \sim 13,000$ km s^{-1} in 2011 September (Pastorello et al. 2013).

Velocities this large have never been associated with LBV outbursts and giant LBV-like eruptions to date. These high-velocity features have been observed in (1) SN explosions or (2) might result from blast waves from successive "failed SNe" (nuclear eruptions) or (3) might arise from shocks that are not connected with a SN or failed SN (i.e., nonnuclear eruptions). This last possibility was suggested for the Type IIn SN 2011ht by Humphreys et al. (2012) and might also apply to the giant eruption of η-Carinae (e.g., Davidson & Humphreys 2012).

SN 2009ip rebrightened again on 2012 July 24 (Drake et al. 2012), only to dim considerably ∼40 days afterward (hereafter referred to as the 2012a outburst). The reappearance of high-velocity spectral features was first noted by Smith & Mauerhan

[34] L. Chomiuk is a Jansky Fellow of the National Radio Astronomy Observatory.

[35] Note, however, that, strictly speaking, a direct observational link between SNe and LBVs would require the detection of LBV-like variability (see Humphreys & Davidson 1994) of the progenitor star in the years preceding the SN.

(2012) on 2012 September 22. This was shortly followed by the major 2012 rebrightening on September 23 (2012b explosion hereafter; Brimacombe 2012; Margutti et al. 2012). SN 2009ip reached $M_V < -18$ mag at this time, consequently questioning the actual survival of the progenitor star: SN or impostor? (Pastorello et al. 2013; Prieto et al. 2013; Mauerhan et al. 2013; Fraser et al. 2013; Soker & Kashi 2013).

Here we present a comprehensive study of SN 2009ip during its remarkable evolution in 2012. Using observations spanning more than 15 decades in wavelength, from the GeV to the radio band, we constrain the properties of the explosion and its complex environment, identify characteristic timescales that regulate the mass-loss history of the progenitor star, and predict neutrino emission associated with this transient. This article is organized as follows. In Sections 2–6 we describe our follow-up campaign and derive the observables that can be directly constrained by our data. In Section 7 we present the properties of the explosion and environment that can be inferred from the data under reasonable assumptions. In Section 8 we address the major questions raised by this explosion and speculate about answers. Conclusions are drawn in Section 9.

Uncertainties are 1σ unless stated otherwise. Following Foley et al. (2011), we adopt a distance modulus of $\mu = 32.05$ mag corresponding to a distance $d_L = 24$ Mpc and a Milky Way extinction $E(B-V) = 0.019$ mag (Schlegel et al. 1998) with no additional host galaxy or circumstellar extinction. From VLT-X-shooter high-resolution spectroscopy our best estimate for the redshift of the explosion is $z = 0.005720$, which we adopt throughout the article. We use U, B, and V for the Johnson filters. u, b, and v refer to *Swift*-UVOT filters. Standard cosmological quantities have been adopted: $H_0 = 71\,\mathrm{km\,s^{-1}\,Mpc^{-1}}$, $\Omega_\Lambda = 0.73$, and $\Omega_M = 0.27$. All dates are in UT and are reported with respect to MJD 56203 (2012 October 3), which corresponds to the UV peak (t_{pk}).

2. OBSERVATIONS

Our campaign uniquely combines data from the radio band to the GeV range. The details of the data acquisition and reduction are provided in Appendix C. Here we provide a summary of our observations, describing first the UV, optical, and NIR observations (which are dominated by thermal emission processes) and then the radio, X-ray, and GeV observations, which sample the portion of the spectrum where nonthermal processes are likely to dominate.

2.1. UV Photometry and Spectroscopy

We initiated our *Swift*-UVOT (Roming et al. 2005) photometric campaign on 2009 September 10 and followed the evolution of SN 2009ip in the six UVOT filters up until 2013 April. *Swift*-UVOT observations span the wavelength range $\lambda_c = 1928$ Å ($w2$ filter) to $\lambda_c = 5468$ Å (v filter, central wavelength listed; see Poole et al. 2008 for details). Our final photometry is reported in Table 4 and shown in Figure 2.

Motivated by the bright UV emission and very blue colors of SN 2009ip we initiated extensive UV spectral monitoring on 2012 September 27, ∼6 days before maximum UV light (2012b explosion). Our campaign includes a total of 22 UVOT UV-grism low-resolution spectra (Figure 3) and two epochs of *HST* observations (PI: R. Kirshner) shown in Figure 4, covering the period $-6\,\mathrm{days} < t - t_{pk} < +34\,\mathrm{days}$. Figure 5 shows the UV portion of the spectra, renormalized using the blackbody fits derived in Section 3.

2.2. Optical Photometry and Spectroscopy

Observations in the v, b, and u filters were obtained with *Swift*-UVOT as explained in Section 2.1 (see Table 4). We complement our data set with R- and I-band photometry obtained by amateur astronomers. A single, late-time (t_{pk} + 190 days) V-band observation was obtained on 2013 April 11.40. We measure $V = 19.65 \pm 0.02$ mag.

We obtained 28 epochs of optical spectroscopy of SN 2009ip covering the time period 2012 August 26 to 2013 April 11 using a number of facilities (see Table 2 in Appendix D). The sequence of optical spectra is shown in Figure 6.

2.3. NIR Photometry and Spectroscopy

We obtained *ZYJHK* data using the Wide-field Infrared Camera on the United Kingdom Infrared Telescope (UKIRT) from September 23 ($t_{pk} - 10$ days) until 2012 December 31 (t_{pk}+89 days). Our photometry is reported in Table 6. Additional NIR photometry was obtained with PAIRITEL at the Fred Lawrence Whipple Observatory (FLWO) on Mount Hopkins, Arizona. Figure 2 presents the complete SN 2009ip NIR data set.

In addition to the X-shooter spectra, we monitored the spectral evolution of SN 2009ip acquiring a total of nine epochs of NIR spectroscopy between 2012 September 27 ($t_{pk} - 6$ days) and 2012 December 3 (t_{pk} + 61 days). The complete sequence of NIR spectra is shown in Figure 7. The observing log can be found in Table 3.

2.4. Millimeter and Radio Observations

We observed SN 2009ip at millimeter (∼85 GHz) and radio wavelengths (∼21 and ∼9 GHz) using the Combined Array for Research in Millimeter Astronomy (CARMA; Bock et al. 2006) and the Karl G. Jansky Very Large Array (VLA; Perley et al. 2011). Our monitoring samples the evolution of SN 2009ip between 2012 September 26 ($t_{pk} - 7$ days) and 2013 March 9 (t_{pk} + 157 days). A summary of the observations is presented in Table 7. No source is detected at the position of SN 2009ip during the first 50 days since the onset of the major outburst in 2012 September, enabling deep limits on the radio emission around optical maximum. A source is detected at 8.85 GHz on 2012 November 13 (t_{pk} + 41 days), indicating a rebrightening of SN 2009ip radio emission at the level of $F_\nu \sim 70$ μJy. The source position is $\alpha = 22{:}23{:}08.29 \pm 0\farcs01$ and $\delta = -28{:}56{:}52.4 \pm 0\farcs1$, consistent with the position determined from *HST* data. We merged the two observations that yielded a detection to improve the signal to noise and constrain the spectrum. Splitting the data into two 1 GHz slices centered at 8.43 GHz and 9.43 GHz, we find integrated flux densities of $F_\nu = 60.0 \pm 16.7$ μJy (8.43 GHz) and $F_\nu = 100.6 \pm 18.9$ μJy (9.43 GHz), suggesting an optically thick spectrum. The upper limit of $F_\nu < 70.5$ μJy at 21.25 GHz on 2012 December 2 indicates that the observed spectral peak frequency ν_{pk} is between 9.43 GHz and 21.25 GHz. A late-time observation obtained on March 9 shows that the radio source faded to $F_\nu < 9.6$ μJy at 9 GHz, pointing to a direct association with SN 2009ip (see Figure 8).

2.5. X-Ray Observations

We observed SN 2009ip with the *Swift*-X-Ray Telescope (XRT; Burrows et al. 2005) from 2012 September 4 until 2013 January 1, for a total exposure of 260 ks, covering the time period of $-29\,\mathrm{days} < t - t_{pk} < +90\,\mathrm{days}$. No X-ray source

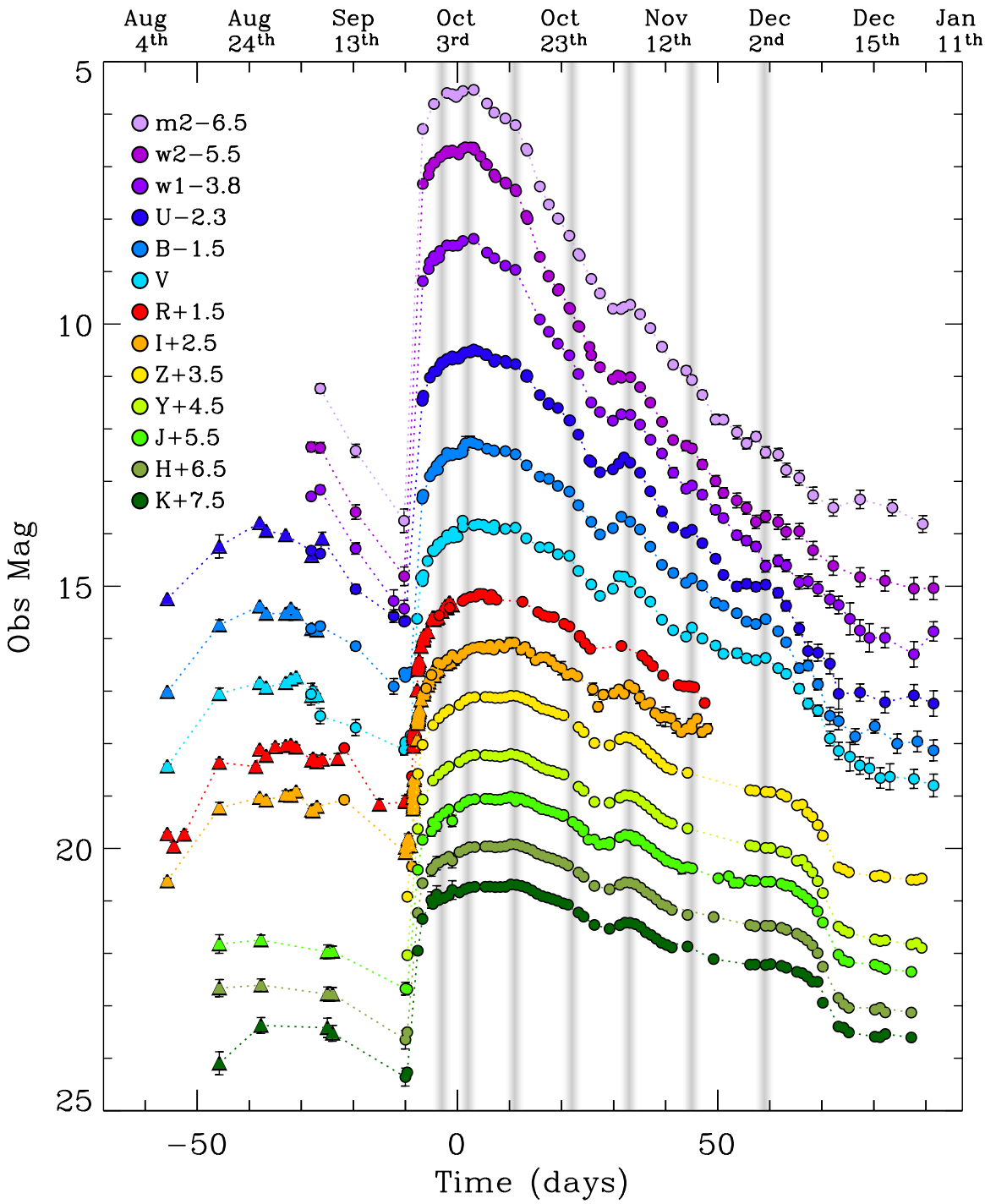

Figure 2. Photometric evolution of SN 2009ip in the UV, optical, and NIR (filled circles). We add NIR observations of the 2012a outburst published by Pastorello et al. (2013) for $t < -10$ days (triangles) together with *R*- and *I*-band photometry from Prieto et al. (2013) obtained during the rise time (triangles). The shaded gray vertical bands mark the time of observed bumps in the light curve. Our late-time UVOT photometry from 2013 April is not shown here.

(A color version of this figure is available in the online journal.)

is detected at the position of SN 2009ip during the decay of the 2012a outburst ($t < -11$ days) and during the rise time of the 2012b explosion (-11 days $< t - t_{\rm pk} < -2$ days). X-ray emission is detected at a position consistent with SN 2009ip starting from $t_{\rm pk} - 2$ days, when the 2012b explosion approached its peak luminosity in the UV/optical bands (Figures 8 and 9). Starting from $t_{\rm pk} + 17$ days, the source was too faint for XRT. We therefore activated our *XMM-Newton* program (PI: P. Chandra). *XMM* observations obtained on 2012 November 3 ($t_{\rm pk} + 31$ days) yielded a detection. From January until 2013 April the source was Sun constrained. 10 ks of *Swift*-XRT data obtained on 2013 April 4.5 ($t_{\rm pk} + 183$ days, when SN 2009ip became observable again) showed no detectable X-ray emission at the position of the transient.

We use the *XMM* observations and the *Swift*-XRT observations obtained around the peak to constrain the spectral parameters of the source and flux calibrate the count-rate light-curve. Both spectra are consistent with a thermal bremsstrahlung model

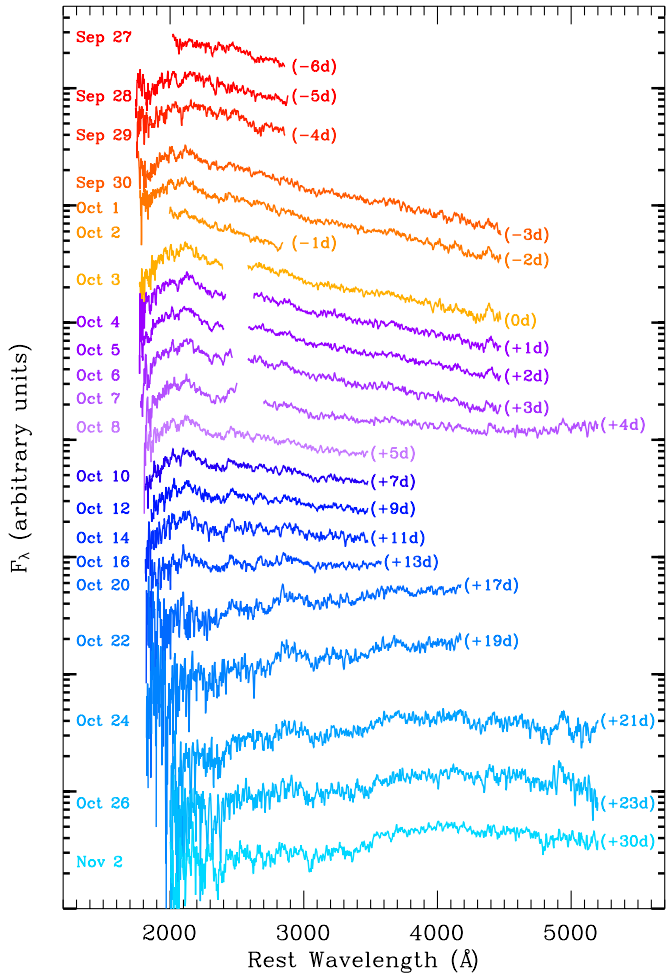

Figure 3. Sequence of *Swift*-UVOT spectra of SN 2009ip covering the rise time (red to orange), peak time (shades of purple), and decay time (shades of blue) of the 2012b explosion.

(A color version of this figure is available in the online journal.)

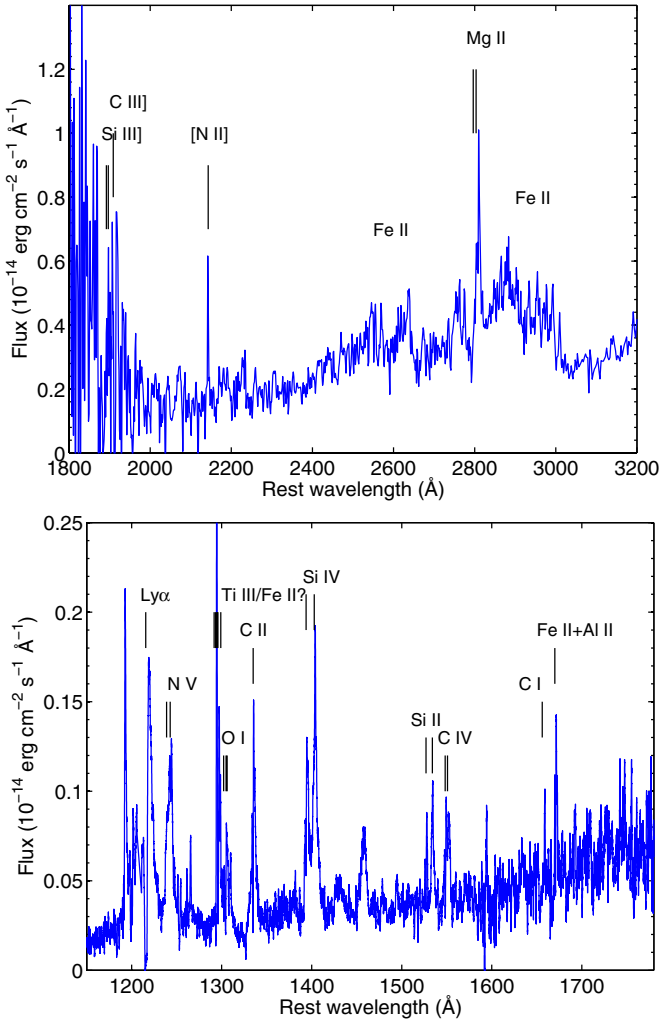

Figure 4. Upper panel: *HST*-STIS spectrum obtained on 2012 October 29 (t_{pk} + 26 days). The C III] and Si III] identifications are in a noisy part of the spectrum and are therefore uncertain. Lower panel: *HST*-COS spectrum obtained on 2012 November 6 (t_{pk} + 34 days).

(A color version of this figure is available in the online journal.)

with $kT = 60$ keV and intrinsic neutral hydrogen absorption $NH_{int} = 0.10^{+0.06}_{-0.05} \times 10^{22}$ cm^{-2}. The spectra are displayed in Figure 10 and show some evidence for an excess of emission around ∼7–8 keV (rest-frame), which might be linked to the presence of Ni or Fe emission lines (see, e.g., SN2006jd and SN2010jl; Chandra et al. 2012a, 2012b).

We note that at the resolution of *XMM* and *Swift*-XRT we cannot exclude the presence of contaminating X-ray sources at a distance $\lesssim 10''$. Observations obtained with the *Chandra X-ray Observatory* (PI: D. Pooley) on $t_{pk} + 19$ days reveal the presence of a contaminating X-ray source lying $\approx 6''$ from SN 2009ip and brighter than SN 2009ip at that time. SN 2009ip is also detected (D. Pooley 2012, private communication). Our contemporaneous *Swift*-XRT observations constrain the luminosity of the contaminating source to be $\lesssim 1.5 \times 10^{39}$ erg s^{-1}, $\lesssim$30% the X-ray luminosity of SN 2009ip at peak. We conclude that the contaminating source is not dominating the X-ray emission of SN 2009ip around peak, *if* stable. The temporal coincidence of the peaks of the X-ray and optical emission of SN 2009ip suggests that the detected X-ray emission is physically associated with SN 2009ip. Given the uncertain contamination, in the following section we conservatively assume $L_x \lesssim 2.5 \times 10^{39}$ erg s^{-1} for the peak X-ray luminosity of SN 2009ip.

2.6. Hard X-Ray Observations

Stellar explosions embedded in an optically thick medium have been shown to produce a collisionless shock when the shock breaks out from the progenitor environment, generating photons with a typical energy $\gtrsim$60 keV (Murase et al. 2011; Katz et al. 2011). We constrain the hard X-ray emission from SN 2009ip using *Swift* Burst Alert Telescope (BAT; Barthelmy et al. 2005; 15–150 keV energy range) observations obtained between 2012 September 4 ($t_{pk} - 29$ days) and 2013 January 1 ($t_{pk} + 90$ days). Analyzing the data acquired around the optical peak we find evidence for a marginal detection at the level of 3.5σ in the time interval -0.8 days $< t - t_{pk} < +0.2$ days (corresponding to 2012 October 2.2–3.2). The simultaneity of the hard X-ray emission with the optical peak is intriguing. However, given the limited significance of the detection and the known presence of a non-Gaussian tail in the BAT noise fluctuations (H. Krimm 2012, private communication), we conservatively use $F < 7 \times 10^{-10}$ erg s^{-1} cm^{-2} ($L < 8 \times 10^{40}$ erg s^{-1}) as the 5σ upper limit to the hard X-ray emission from SN 2009ip around maximum light.

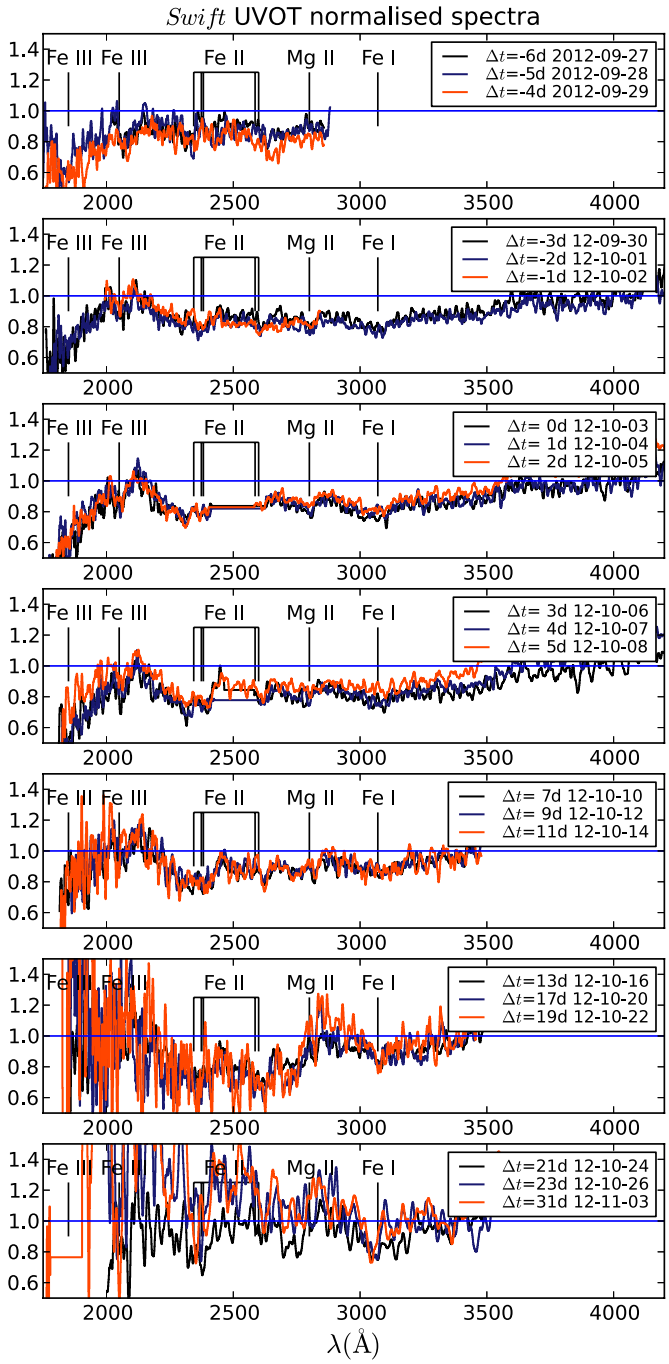

Figure 5. UV portion of the *Swift*-UVOT spectra renormalized using the blackbody fits of Section 3. Fe III absorption features become weaker with time, while Fe II develops stronger absorption features, consistent with the progressive decrease of the temperature with time (Figure 11).

(A color version of this figure is available in the online journal.)

2.7. GeV Observations

GeV photons are expected to arise when the SN shock collides with a dense circumstellar shell of material, almost simultaneous with the optical light-curve peak (Murase et al. 2011; Katz et al. 2011). We searched for high-energy γ-ray emission from SN 2009ip using all-sky survey data from the *Fermi* Large Area Telescope (LAT; Atwood et al. 2009), starting from 2012 September 3 ($t_{\rm pk} - 30$ days) until 2012 October 31 ($t_{\rm pk} + 28$ days). We find no significant emission at the position of SN 2009ip. Assuming a simple power-law spectrum with photon index $\Gamma = 2$, the typical flux upper limits in one-day intervals are $\lesssim$(1–3) $\times 10^{-10}$ erg cm^{-2} s^{-1} (100 MeV–10 GeV energy range, 95% c.l.). Integrating around the time of the optical peak (-2 days $< t - t_{\rm pk} <$ +4 days) we find $F < [2.1, 1.9, 3.6] \times 10^{-11}$ erg cm^{-2} s^{-1} for three energy bands (100 MeV–464 MeV, 464 MeV–2.1 GeV, and 2.1 GeV–10 GeV).

3. EVOLUTION OF THE CONTINUUM FROM THE UV TO THE NIR

Our 13 filter photometry allows us to constrain the evolution of the spectral energy distribution (SED) of SN 2009ip with high accuracy from the UV to the NIR.[36] We model the SED with a blackbody spectral model, keeping in mind that a blackbody is an approximation to a likely more complex spectral distribution.

For $t > t_{\rm pk} - 7$ days the UV + *BVRI* SED is well fitted by a blackbody spectrum with a progressively larger radius ("hot" blackbody component in Figure 11). The temperature evolution tracks the bolometric luminosity, with the photosphere becoming appreciably hotter in correspondence with light-curve bumps. Around $t_{\rm pk}$ + 70 days the temperature settles to a floor around 5000 K and remains nearly constant in the following 20 days. The temperature has been observed to plateau at similar times in some SNe IIn (e.g., SN 2005gj and SN 1998S where the blackbody temperature reached a floor at ~6000–6500 K; Prieto et al. 2007; Fassia et al. 2000) and in SNe IIP as well (e.g., SN 1999em, with a plateau at ~5000 K; Leonard et al. 2002).

The radius of the photosphere increases from $\sim 5.1 \times 10^{14}$ cm to $\sim 6.3 \times 10^{14}$ cm in ~0.3 days (from $t = t_{\rm pk} - 6.8$ days to $t = t_{\rm pk} - 6.5$ days), then makes a transition to a linear evolution followed by a plateau around $R_{\rm HOT} = 1.6 \times 10^{15}$ cm. A rapid decrease in radius is observed around $t_{\rm pk}$ + 70 days. After this time the $R_{\rm HOT}$ mimics the temporal evolution of the bolometric light-curve (see Figure 11). In SNe dominated by interaction with preeexisting material, the photospheric radius typically increases steadily with time, reaches a peak and then smoothly transitions to a decrease (see, e.g., SN 1998S, Fassia et al. 2000; SN 2005gj, Prieto et al. 2007). The more complex behavior we observe for SN 2009ip likely results from a more complex structure of the immediate progenitor environment (Section 8).

Starting from $t_{\rm pk}$ + 16 days, the best-fitting blackbody model tends to overpredict the observed flux in the UV, an effect likely due to increasing line blanketing. As the temperature goes below $\sim 10^4$ K, the recombination of the ejecta induces a progressive strengthening of metal line blanketing, which is responsible for partially blocking the UV light.

Starting around $t_{\rm pk}$ + 59 days the UV emission fades more slowly and we observe a change in the evolution of the UV and optical colors: from red to blue (Figure 11, lower panel; Figure 12, upper panel). This can also be seen from Figure 2, where the NIR emission displays a more rapid decay than the UV. This manifests as an excess of UV emission with respect to the blackbody fit. After $t_{\rm pk}$ + 67 days a pure blackbody spectral shape provides a poor representation of the UV to NIR SED.

We furthermore find clear evidence for excess of NIR emission with respect to a simple blackbody fit (see Figure 13) as we first reported in Gall et al. (2012), based on the analysis of the

[36] The extremely blue colors and color evolution of SN 2009ip (see Figure 11, lower panel, and Figure 12) impose nonnegligible deviations from the standard UVOT count-to-flux conversion factors. We account for this effect following the prescriptions by Brown et al. (2010).

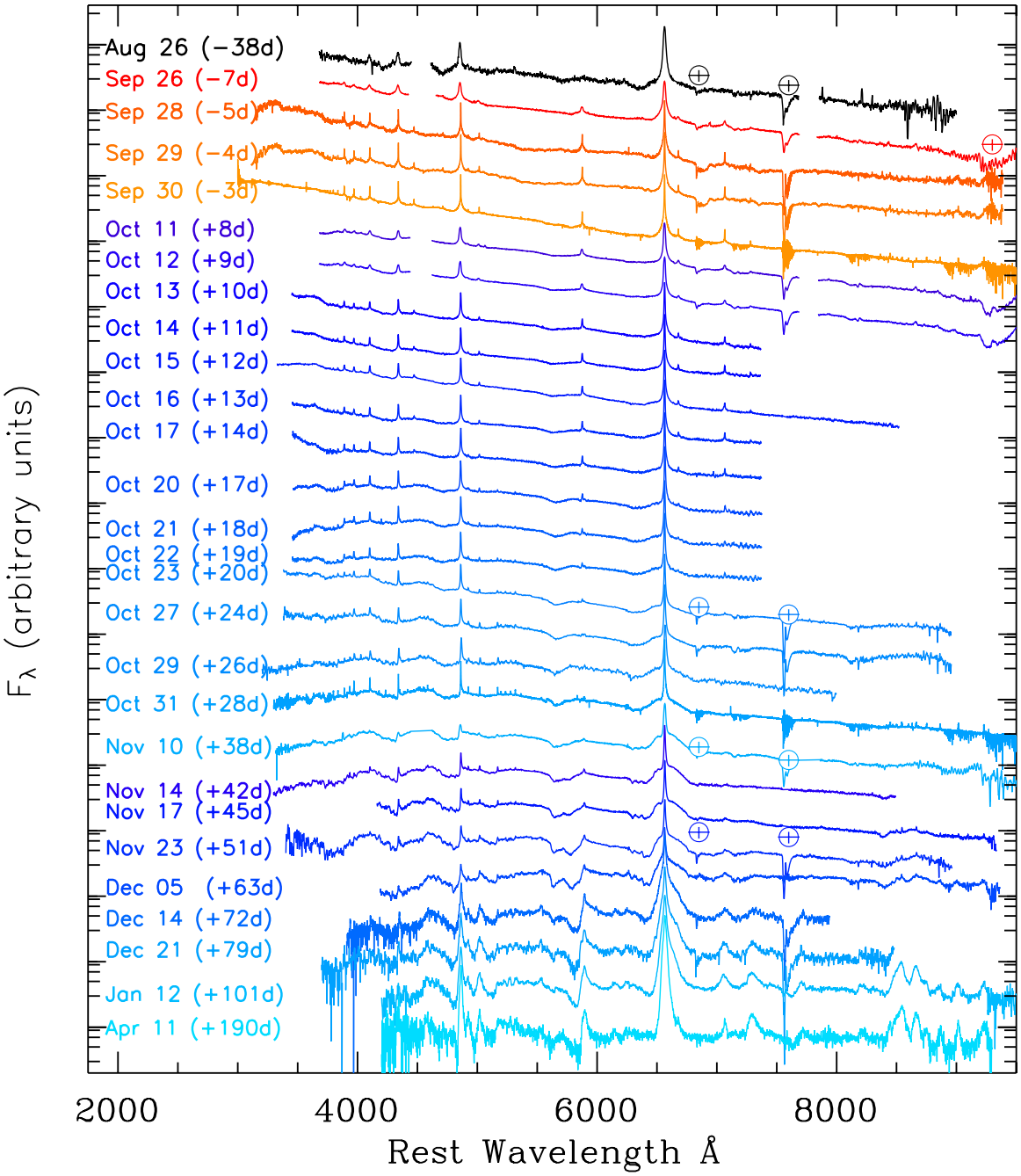

Figure 6. Optical spectra of SN 2009ip. Shades of red (blue) are used for spectra obtained during the rise (decay) time of the 2012b explosion. Black is used for the 2012a outburst.

(A color version of this figure is available in the online journal.)

VLT/X-shooter spectra (Figures 19 and 20). The NIR spectra of Figure 7 rule out line emission as a source of the excess.

Applying the same analysis to the 2012a outburst we find that the temperature of the photosphere evolved from ∼13,400 K (at $t_{\rm pk} - 56$ days) to 8000 K ($t_{\rm pk} - 12$ days), with an average decay of ∼120 K day^{-1}. Our modeling shows a slightly suppressed UV flux, which we interpret as originating from metal line blanketing. The SED at $t_{\rm pk} - 38$ days shows evidence for a NIR excess corresponding to $T_{\rm COLD} \sim 2000$ K at the radius consistent with $R_{\rm COLD} \sim 4 \times 10^{15}$ cm (as found during the 2012b explosion).

Finally, we use the SED best-fitting models above to compute the bolometric luminosity of SN 2009ip. Displayed in Figure 11 is the contribution of the "hot" blackbody. The "cold" blackbody contribution is marginal, being always (2–4)% the luminosity of the "hot" component.

4. SPECTRAL CHANGES AT UV/OPTICAL/NIR FREQUENCIES

The spectrum of SN 2009ip during the 2012a outburst is dominated by prominent Balmer lines with narrow emission components (FWHM ≈ 800 km s^{-1} for Hα) accompanied by absorption features indicating the presence of high-velocity material extending to $v \approx -14{,}000$ km s^{-1} (Pastorello et al. 2013; Mauerhan et al. 2013). By the time of the 2012b

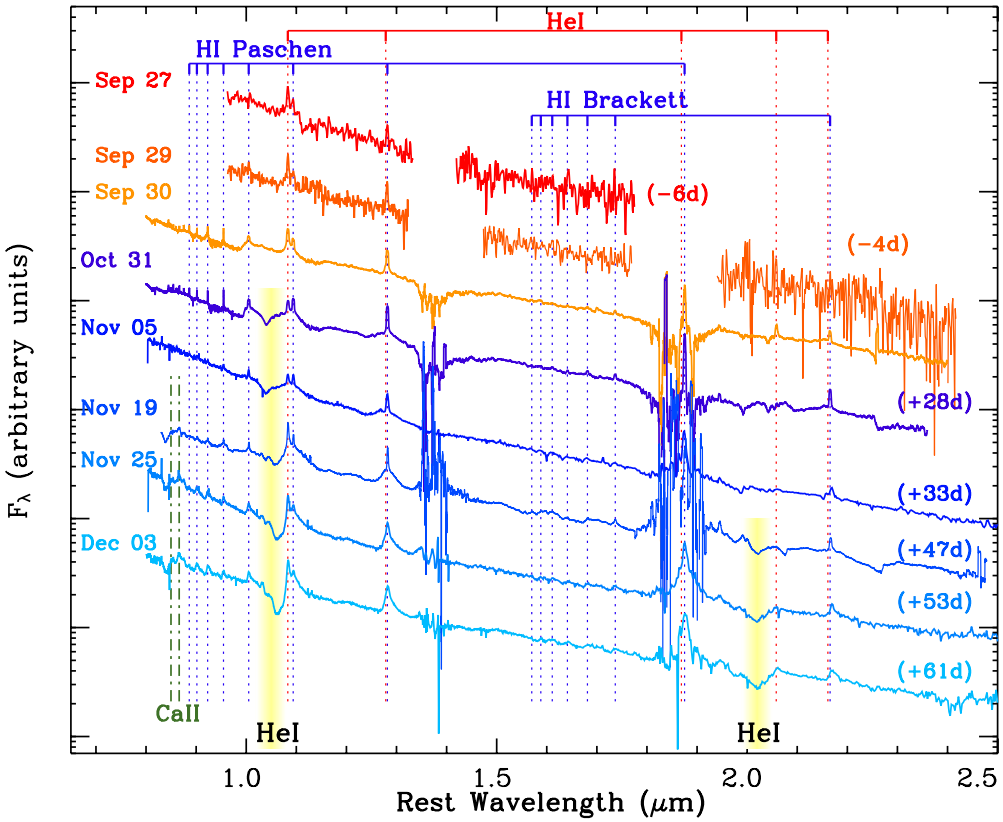

Figure 7. NIR spectral sequence with line identifications overlaid. The high-resolution spectrum obtained on 2012 November 19 has been smoothed here for display purposes. Shades of red (blue) have been used for spectra obtained during the rise (decay) time. A portion of the VLT/X-shooter spectra is also shown.

(A color version of this figure is available in the online journal.)

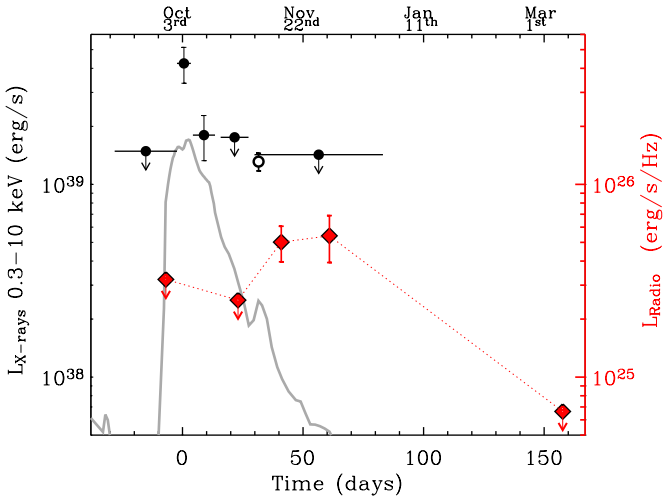

Figure 8. X-ray (*Swift*-XRT and *XMM-Newton*, filled and open circle, respectively) and 9 GHz radio light-curve (red squares, VLA) of SN 2009ip. X-rays are detected when the bolometric luminosity reaches its peak. Radio emission is detected at much later times. A rescaled version of the bolometric light-curve is also shown for comparison. This plot does not include the late-time X-ray limit obtained on 2013 April 4.5 (t_{pk} + 183 days).

(A color version of this figure is available in the online journal.)

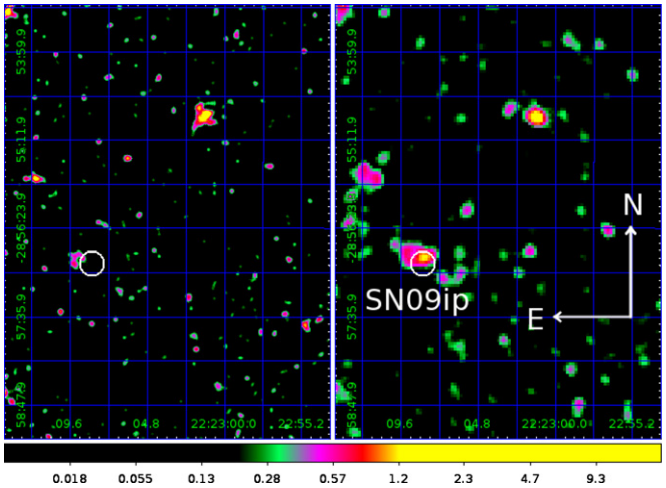

Figure 9. Left panel: *Swift*-XRT image of the field of SN 2009ip collecting data before and after the optical peak (-32 days $< t - t_{pk} < -2$ days and $+29$ days $< t - t_{pk} < +83$ days), for a total exposure time of 110 ks. Right panel: the same field imaged around the optical peak (-2 days $< t - t_{pk} < +13$ days), for a total exposure time of 86 ks. In both panels a white circle marks a 10″ region around SN 2009ip. X-rays are detected at a position consistent with SN 2009ip around the optical peak (right panel) with a significance of 6.1σ.

(A color version of this figure is available in the online journal.)

rebrightening the Hα line developed a prominent broad emission component with FWHM $\approx 8000\,\mathrm{km\,s^{-1}}$ (Mauerhan et al. 2013, their Figure 5). The broad component disappeared 3 days later: on 2012 September 26 ($t_{pk} - 7$ days) the Hα line evolved back to the narrow profile (Figure 14), it yet still retained evidence for absorption with core velocity $v \approx -5000\,\mathrm{km\,s^{-1}}$. By 2012 September 30 ($t_{pk} - 3$ days, Figures 19 and 20) the spectrum no longer shows evidence for the high-velocity components in absorption and is instead dominated by He I and H I lines with narrow profiles, likely indicating that the photosphere is imbedded within a low-speed outflow.

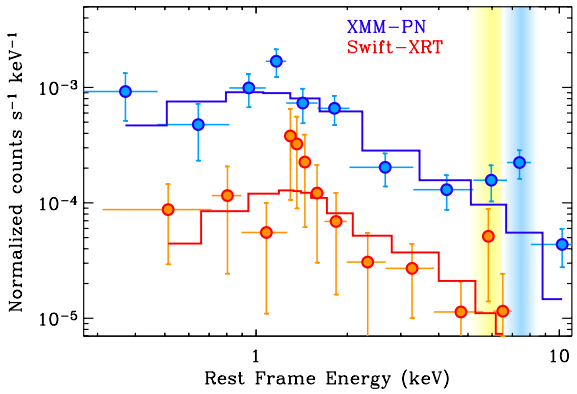

Figure 10. X-ray spectra of SN 2009ip. The *Swift*-XRT spectrum collects observations obtained around the optical peak ($t_{pk} - 2$ days until $t_{pk} + 13$ days, a total exposure time of 86 ks). The *XMM* EPIC-PN spectrum was obtained on 2012 November 3 ($t_{pk} + 31$ days, a total exposure of 55 ks). The spectral model consists of absorbed bremsstrahlung emission at $kT = 60$ keV and intrinsic absorption ($NH_{int} = 0.10^{+0.06}_{-0.05} \times 10^{22}$ cm^{-2} and $NH_{int} < 3.1 \times 10^{21}$ cm^{-2} for the *XMM* and XRT spectra, respectively). Contamination by a nearby source lying ≈6″ from SN 2009ip is expected for the *XMM* spectrum. The color-coded shaded areas highlight the presence of possible emission excess with respect to the model.

(A color version of this figure is available in the online journal.)

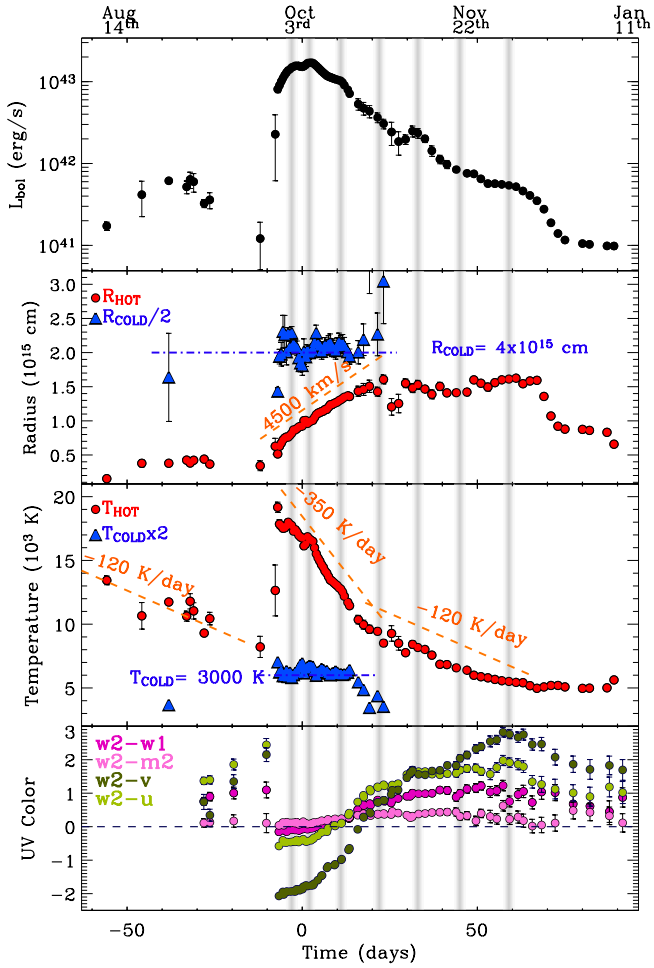

Figure 11. Upper panel: bolometric light-curve of SN 2009ip calculated from the best-fitting blackbody temperatures and radii displayed in the intermediate panels. Lower panel: UV color evolution with time. The onset of the 2012b explosion corresponds to a sudden change in UV colors. After that, the UV colors become progressively redder. Vertical shaded bands mark the time of observed bumps in the photometry of Figure 2: some are powerful enough to be clearly visible in the bolometric luminosity curve as well.

(A color version of this figure is available in the online journal.)

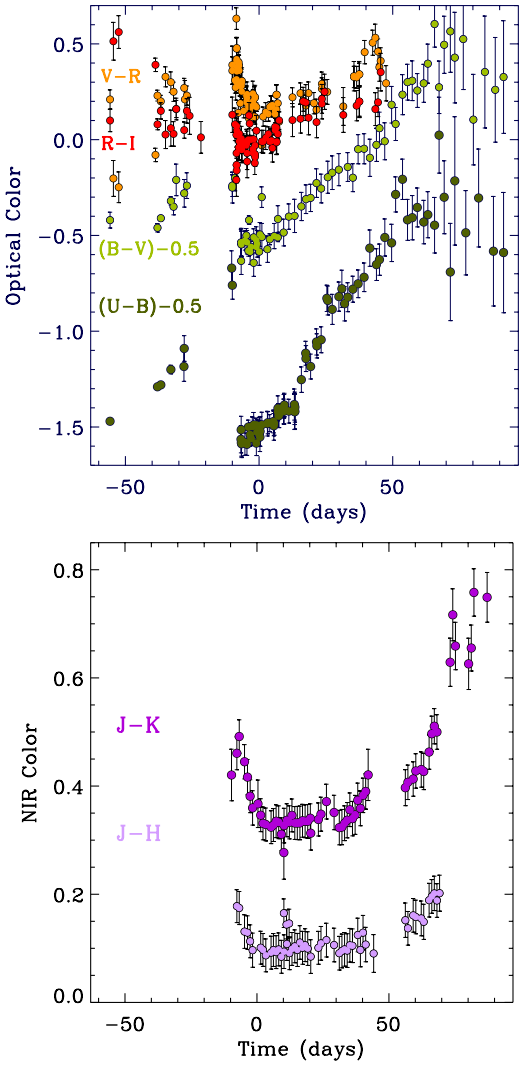

Figure 12. Evolution of the optical and NIR colors. While SN 2009ip clearly evolves toward redder optical colors starting from $t_{pk} - 3$ days, no strong evolution is apparent in the NIR colors in the same time interval.

(A color version of this figure is available in the online journal.)

In the following months, SN 2009ip progressively evolves from a typical SN IIn (or LBV-like) spectrum with clear signs of interaction with the medium to a spectrum dominated by broad absorption features, which is more typical of SNe IIP (Figure 21).

Our two X-shooter spectra (Figures 19 and 20) sample two key points in this metamorphosis, providing a broadband view of these spectral changes at high resolution. The major spectral changes during the 2012b explosion can be summarized as follows.

1. During the first week after peak, H Balmer lines showed a narrow core with extended Thomson-scattered wings (Figure 14).
2. Broad/intermediate absorption/emission features progressively reappear in the H Balmer lines, with evidence for multiple velocity components (Figures 14–16) extending to $v \sim -15{,}000\,\mathrm{km\,s^{-1}}$.
3. At no epoch do we find evidence for very narrow, low velocity blue-shifted absorption at $v \sim -100\,\mathrm{km\,s^{-1}}$, which is different from what is typically observed in

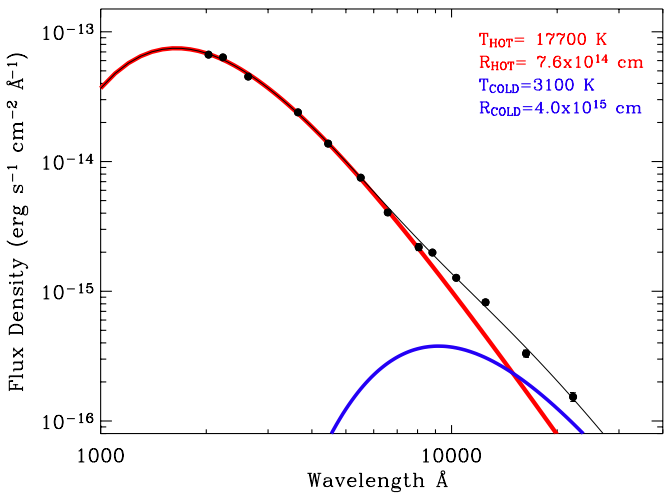

Figure 13. Black solid line: the best-fitting SED model obtained at $t_{pk}-4.5$ days, which clearly shows the presence of the "hot" (red line) and "cold" (blue line) components in the spectrum.

(A color version of this figure is available in the online journal.)

Type IIn SNe and LBVs (see, e.g., SN 2010jl, Smith et al. 2012).

4. Narrow He I lines weaken with time (Figure 17); He I later reemerges with the intermediate component only.
5. Fe II features reemerge and later develop P Cygni profiles.
6. Emission originating from Na I D is detected (Figure 17).
7. A broad near-infrared Ca II triplet feature typical of Type IIP SNe develops starting around 2012 November 15 (Figure 18).
8. More importantly, SN 2009ip progressively develops broad absorption dips that have never been observed in LBV-like eruptions, while this is typical of a variety of SN explosions (Figure 17). Broad absorption dips disappear ∼200 days after peak (Figure 30).
9. At ∼100 days after peak, emission from forbidden transitions (see, e.g., [Ca II] λλ7291, 7324 in Figure 6) starts to emerge.
10. Limited spectral evolution is observed between t_{pk} + 100 days and t_{pk} + 200 days (when SN 2009ip reemerges from the Sun constraint). However, absorbtion features migrated to lower velocities.

Each of the items above is discussed in detail in the following subsections.

4.1. Evolution of the H I Line Profiles

The Hα line profile experienced a dramatic change in morphology. Figure 14 shows the Hα line at representative epochs: at any epoch the Hα line has a complex profile resulting from the combination of a narrow component (FWHM < 1000 km s^{-1}), intermediate/broad width components (FWHM > 1000 km s^{-1}) and blue absorption features with clearly distinguished velocity components. Emission and absorption components with similar velocity are also found in the Hβ and Hγ line profiles (Figure 15). The evolution of the line profile results from changes in the relative strengths of the different components in addition to the appearance (or disappearance) of high-velocity blue absorption edges (Figure 16). The most relevant spectral changes are detailed below.

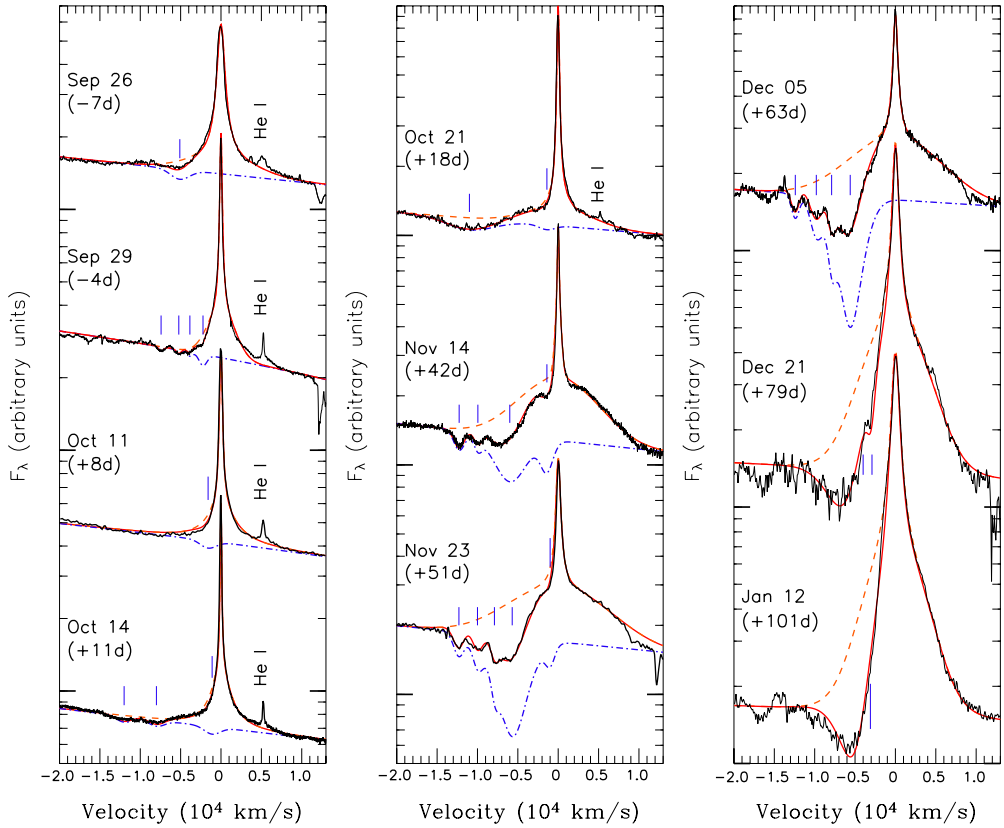

Figure 14. Evolution of the Hα line profile with time. Orange dashed line: emission components. Blue dot-dashed line: absorption components. Red thick line: composite line profile. The vertical blue lines mark the velocity of the absorption components.

(A color version of this figure is available in the online journal.)

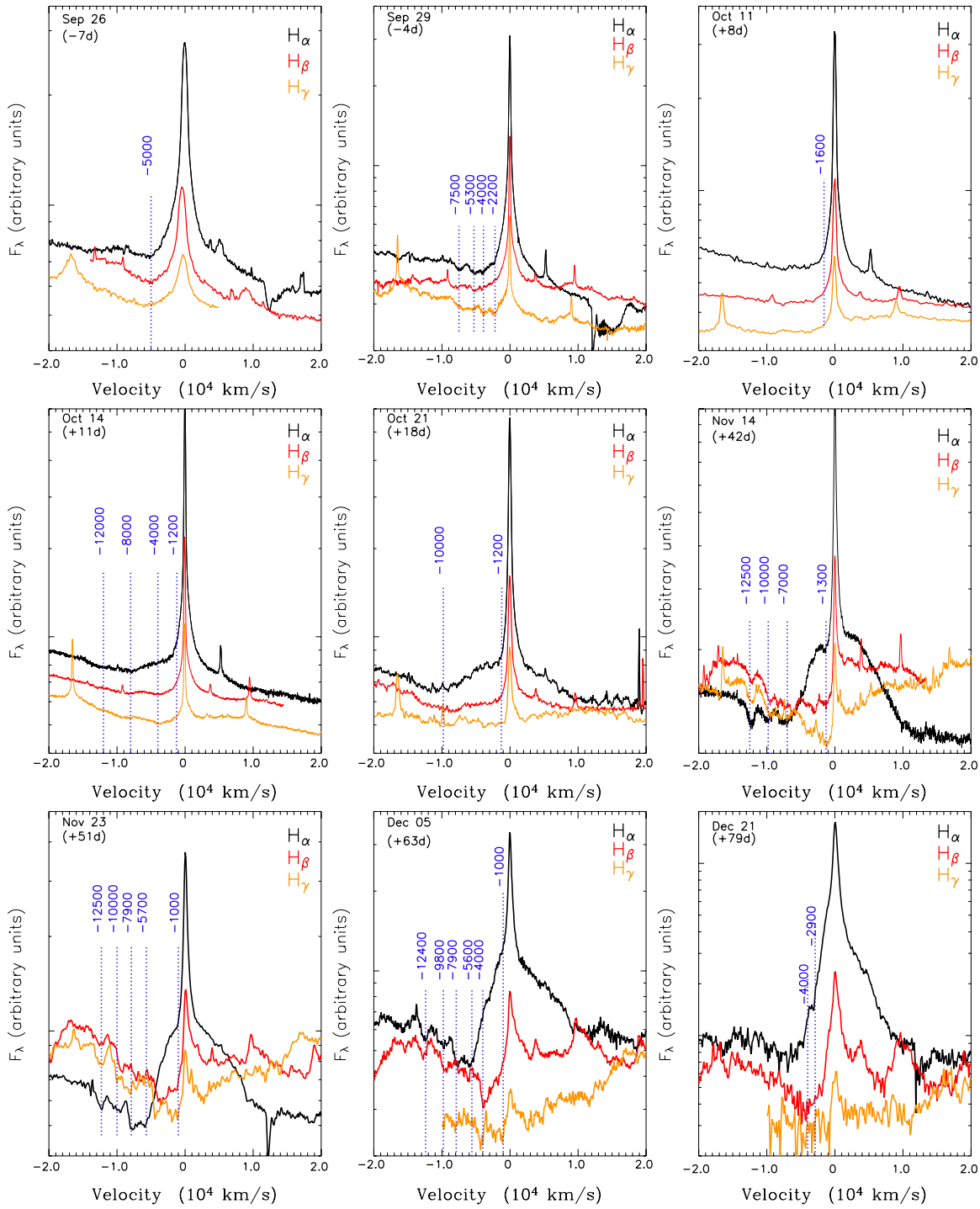

Figure 15. Hα, Hβ, and Hγ line profiles at representative epochs. Blue dotted lines: velocity of the major absorption components in the Hα line profile. For 2012 December 5 we also added two absorption components at $-1000\,\mathrm{km\,s^{-1}}$ and $-4000\,\mathrm{km\,s^{-1}}$ identified in the Hβ and Hγ lines. The late-time spectrum acquired on $t_{\rm pk}+101$ days shows limited evolution in the Hα profile with respect to the previous epoch and is not shown here.

(A color version of this figure is available in the online journal.)

By $t_{\rm pk}-7$ days the broad components dominating the line profile 10 days before (Mauerhan et al. 2013) have weakened to the level that most of the emission originates from a much narrower component with FWHM $\approx 1000\,\mathrm{km\,s^{-1}}$. Absorption from high-velocity material ($v \approx -5000\,\mathrm{km\,s^{-1}}$, measured at the minimum of the absorption feature) is still detected when the 2012b explosion luminosity is still rising. The high-resolution spectra collected on $t_{\rm pk}-5$ and $t_{\rm pk}-4$ days allow us to resolve different blue absorption components with central velocities $v \approx -2200\,\mathrm{km\,s^{-1}}$, $\approx -4000\,\mathrm{km\,s^{-1}}$, $\approx -5300\,\mathrm{km\,s^{-1}}$, and $\approx -7500\,\mathrm{km\,s^{-1}}$ with $\sigma \approx 300$–$500\,\mathrm{km\,s^{-1}}$. These absorption features are detected in the Hβ and Hγ lines as well (Figure 15). The width of the narrow component of emission decreases to FWHM $\approx 280\,\mathrm{km\,s^{-1}}$.

On 2012 September 30 ($t_{\rm pk}-3$ days) SN 2009ip approaches its maximum luminosity (Figure 11). The Hα line is well modeled by the combination of two Lorentzian profiles with FWHM $\approx 240\,\mathrm{km\,s^{-1}}$ and FWHM $\approx 2600\,\mathrm{km\,s^{-1}}$. We find

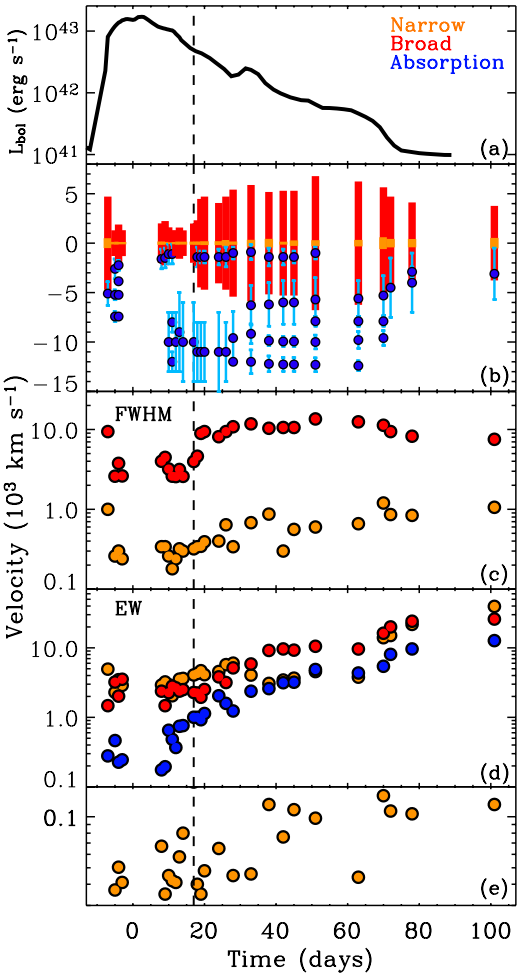

Figure 16. Evolution of the Hα line with time. We model the Hα line with a combination of Lorentzian and Gaussian functions. Orange, red, and blue is used for the narrow, broad, and blue-shifted absorption components, respectively. Panel (a): bolometric light-curve. Panel (b): the red (orange) bars span the FWHM of the broad (narrow) component. These values are also reported in panel (c). Blue dots: absorption minima as obtained by modeling the absorption with a combination of Gaussians. Negative values indicate blue-shifted components. We use light-blue bars to mark the 1σ width. Panel (d) shows the evolution of the equivalent width of the different components. The peak of the narrow component progressively shifts to larger redshifted velocities as illustrated in panel (e) and independently found by Fraser et al. (2013). The vertical dashed line marks an important time in the evolution of SN 2009ip from different perspectives: from this plot it is clear that around this time the width of broad component undergoes a remarkable transition from FWHM $\sim$3000 km s^{-1} to FWHM $\sim$10,000 km s^{-1}.

(A color version of this figure is available in the online journal.)

no clear evidence for absorption components. Interpreting the broad wings as a result of multiple Thomson scattering in the circumstellar shell of the narrow-line radiation (e.g., Chugai 2001; Dessart et al. 2009; Humphreys et al. 2012) suggests that the optical depth of the unaccelerated circumstellar shell envelope to Thomson scattering is $\tau \sim 3$. A Thomson-scattering optical depth $\tau \sim$ 2–4 is also expected if the continuum originates at locations where the thermalization depth is $\approx$1 (Davidson 1987[37]).

High-velocity absorption features in the blue wing of the Hα line progressively reappear as the luminosity enters its declining phase. The Hα line exhibits a combination of narrow (FWHM $\approx$ 340 km s^{-1}) and broad (FWHM $\approx$ 2000–3000 km s^{-1}) components, with the broad component becoming more prominent with time. At t_{pk} + 11 days (time of the third bump of the bolometric light-curve, Figure 11), high-velocity absorption features reappear, with absorption minima at $v \approx -12{,}000$ km s^{-1} and $v \approx -8000$ km s^{-1} ($\sigma \sim 1000$ km s^{-1}). The low-velocity P Cygni absorption is also detected at $v \approx -1200$ km s^{-1}.

A spectrum obtained on t_{pk} + 18 days shows the development of an even stronger broad emission component with FWHM $\approx$ 9400 km s^{-1}. We also find clear evidence for a deep minimum at $v \approx -10{,}000$ km s^{-1} with edges extending to $v \approx -14{,}000$–$15{,}000$ km s^{-1}. The broad emission component keeps growing with time and dominates the line profile at t_{pk} + 42 days. By t_{pk} + 51 days, the broad component reaches FWHM $\approx$ 13,600 km s^{-1}. High-velocity absorption features are still detected at $v \approx -12{,}500$ km s^{-1}, $v \approx -10{,}000$ km s^{-1}, and $v \approx -7000$ km s^{-1}.

At t_{pk} + 79 days we find a less prominent broad component with FWHM $\approx$ 8200 km s^{-1}. A spectrum obtained at t_{pk} + 101 days confirms this trend (broad component FWHM $\approx$ 7500 km s^{-1}): the bulk of the absorption is now at lower velocities $v \approx -3100$ km s^{-1}. At t_{pk} + 190 days the blue-shifted absorption is found peaking at even lower velocities of $v \lesssim -2400$ km s^{-1}, and the "broad" (now intermediate) component has FWHM of only $\approx$2000 km s^{-1}.

Finally, comparing the H Paschen and Brackett emission lines using our two highest resolution spectra collected around the peak (narrow-line emission dominated spectrum at $t_{pk} - 3$ days) and 28 days after peak (when broad components start to emerge, see Figures 19 and 20), we find that for both epochs the line profiles are dominated by the narrow component (FWHM $\approx$ 170 km s^{-1}) with limited evolution between the two.

We conclude by noting that, observationally, t_{pk}+17 days (i.e., 2012 October 20) marks an important transition in the evolution of SN 2009ip: around this time the broad Hα component evolves from FWHM $\sim$ 3000 km s^{-1} to FWHM $\sim$ 10,000 km s^{-1} (Figure 16); the photospheric radius R_{HOT} flattens to $R_{HOT} \sim 1.6 \times 10^{15}$ cm while the temperature transitions to a milder decay in time (Section 3, Figure 11).

4.2. The Evolution of He I Lines

He I lines are not unambiguously detected on 2012 August 26. They are however detected one month later, $\sim$3 days after SN 2009ip rebrightened. As for the H Balmer lines, high-resolution spectroscopy obtained at $t_{pk} - 5$ and $t_{pk} - 4$ days shows the appearance of multiple absorption components on the blue wing of the He I λ5876 and λ7065 lines, with velocities $v \approx -2000$ km s^{-1}, $\approx$−4800 km s^{-1}, and $\approx$−7000 km s^{-1} (to be compared with Figure 15). High-velocity absorption features disappear by $t_{pk} - 3$ days, when the He I lines show the combination of a narrow plus intermediate profiles with FWHM $\approx$ 240 km s^{-1} and FWHM $\approx$ 2000 km s^{-1}, respectively.

Starting from $t_{pk} - 3$ days He I features become weaker until He I λ7065 is not detected at t_{pk} + 28 days (Figure 19). He I later reappears at $t > t_{pk}$ + 43 days showing the broad/intermediate component only (FWHM $\approx$ 2500 km s^{-1} at t_{pk} + 63 days). At t_{pk} + 101 days He I λ7065 shows an intermediate-broad emission profile with FWHM $\approx$ 3000 km s^{-1}. Roughly 100 days later He I 7065 Å is clearly detected with considerably narrower emission (FWHM $\approx$ 1000 km s^{-1}). He I λ6678 also reemerges on the red wing of the Hα profile (Figure 30).

[37] See also http://etacar.umn.edu/Workshop2012/Talks/KD_DenseWind.pdf

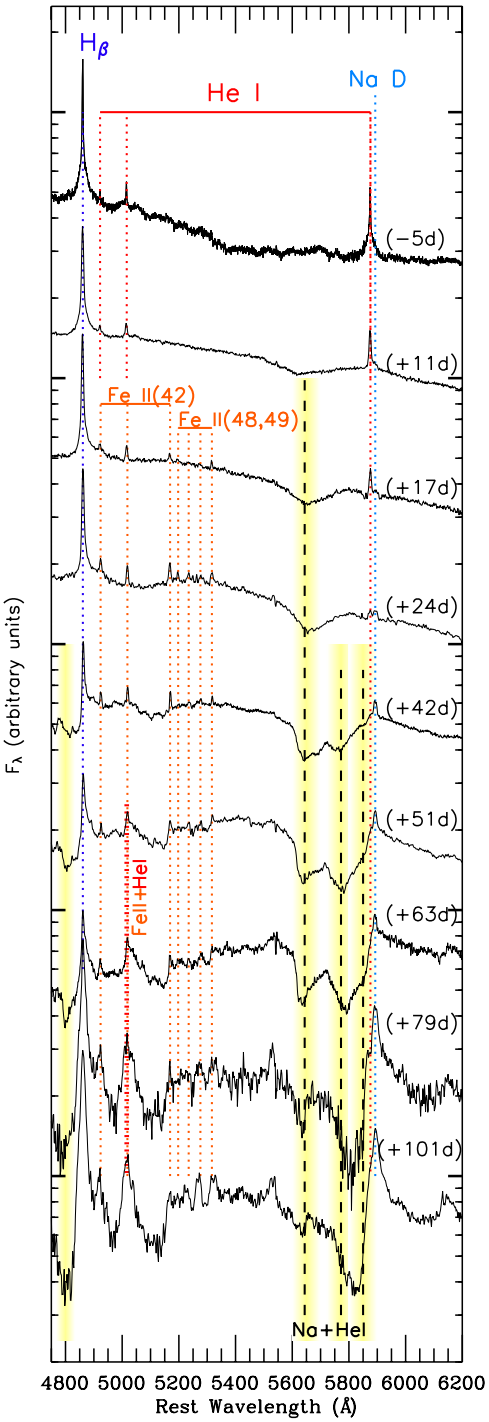

Figure 17. Key spectral changes in SN 2009ip between 4500 and 6200 Å: narrow He I emission lines subside while Na I D emission grows in strength. He I later reappears with the broad/intermediate component. Fe II emission lines emerge, while broad absorption dips develop red-ward the Na I D (and He I) lines, around 5650 Å. Starting from $\sim t_{\rm pk}$ + 30 days, additional broad absorption features around 5770 Å and 5850 Å appear, associated with the He I and the Na I D lines; H I lines develop strong blue-shifted absorption.

(A color version of this figure is available in the online journal.)

4.3. The Evolution of Fe II Lines

A number of Fe II lines have been observed during previous SN 2009ip outbursts (both in 2009, 2011, and the 2012a outburst; see Pastorello et al. 2013, their Figures 5 and 6). The Fe responsible for this emission therefore preexistents the 2012 explosion. Fe II is not detected during the 2012b outburst until $t_{\rm pk}$ + 17 days (Figure 17). At $t_{\rm pk}$ + 28 days the Fe II lines λ5018 and λ5169 (multiplet 42) have FWHM ≈ 240 km s^{-1}. As a comparison, the FWHM of the narrow Hα component from the same spectrum is ≈170 km s^{-1}. By $t_{\rm pk}$ + 63 days the Fe II emission lines develop a P Cygni profile (Figure 17), with $v \approx -1000$ km s^{-1}, possibly extending to $v \approx -4000$ km s^{-1}.

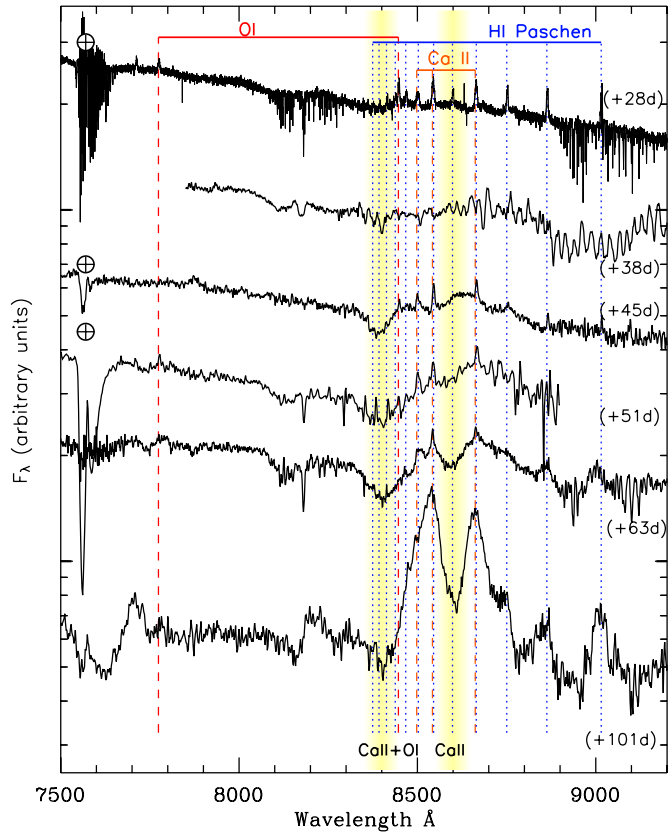

Figure 18. Beginning at $t_{\rm pk}$ + 30 days SN 2009ip develops broad emission and absorption components between 8300 Å and 9000 Å that we attribute to Ca II. NIR emission from the Ca II triplet is typical of IIP SNe.

(A color version of this figure is available in the online journal.)

4.4. The NIR Ca II Feature

Starting from ∼30 days after peak, NIR emission from the Ca II triplet λλ8498, 8542, 8662 progressively emerges (Figure 18; see also Fraser et al. 2013, their Figure 4). The appearance of this feature is typically observed during the evolution of Type II SN explosions (see, e.g., Pastorello et al. 2006). No previous outburst of SN 2009ip showed this feature (2012a outburst included; see Pastorello et al. 2013); no broad Ca II triplet feature has ever been observed in an LBV-like eruption, either. Figure 18 also shows the emergence of broad absorption dips around 8400 Å and 8600 Å, which likely results from the combination of O I and Ca II.

4.5. The Development of Broad Absorption Features

High-velocity, broad absorption features appear in our spectra starting nine days after peak (see yellow bands in Figures 7, 17, 19, and 20). Absorption features of similar strength and velocity have never been associated with an LBV-like eruption to date and are more typical of SNe (Figure 21). These absorption features are unique to the 2012b

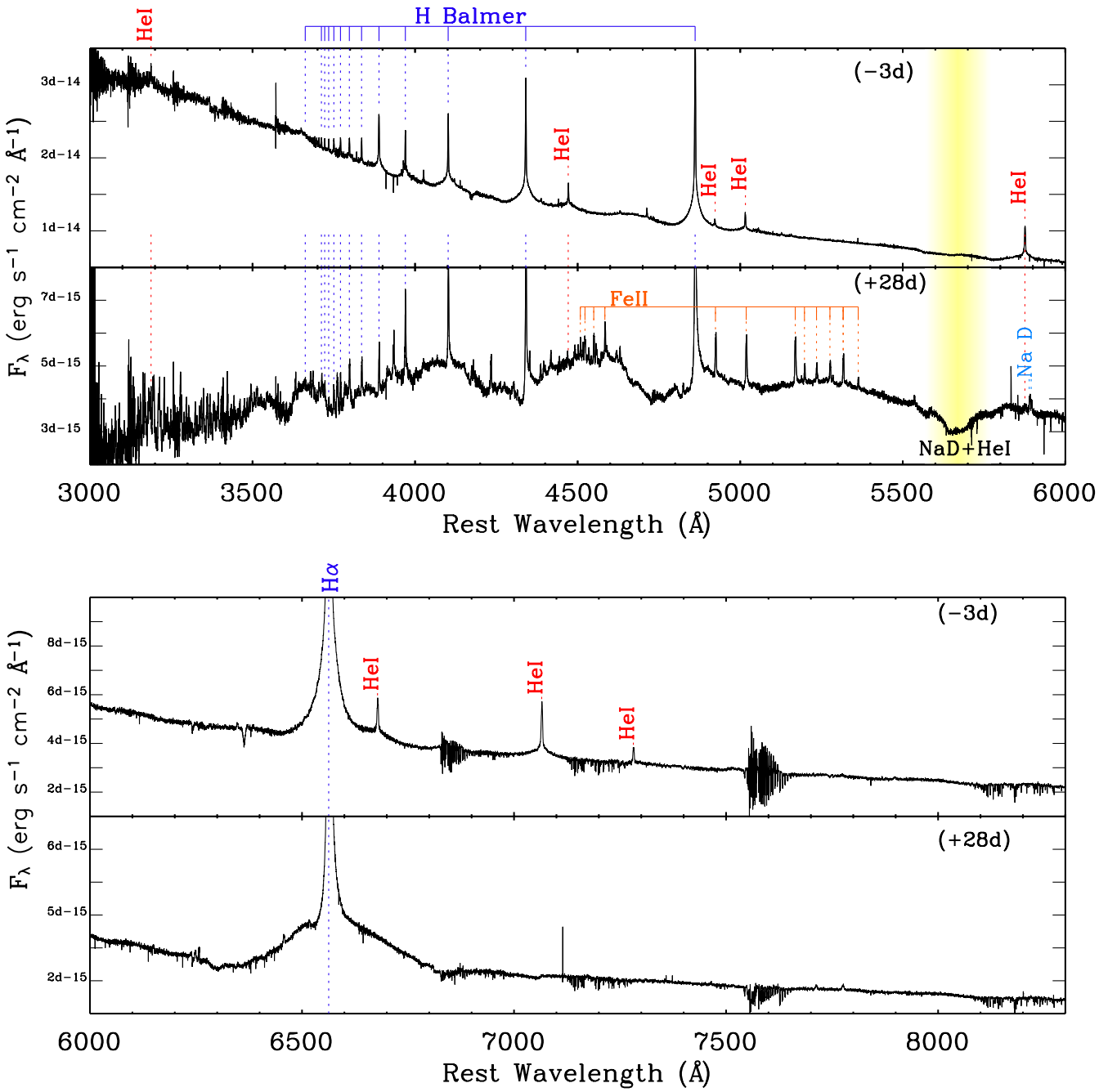

Figure 19. High-resolution VLT/X-shooter spectra captured the evolution of SN 2009ip in fine detail. Upper panel: around the optical peak, on 2012 September 30 ($t_{pk} - 3$ days), SN 2009ip shows a narrow-line dominated spectrum typical of SNe (and LBVs) interacting with a medium. One month later (lower panel of each plot) SN 2009ip started to develop broad emission components (see in particular the Hα line) and deep absorption features (e.g., the yellow-shaded band around 5650 Å) more typical of SNe IIP. The complementary 10000–24500 Å wavelength range is shown in Figure 20. Data have been corrected for Galactic extinction.

(A color version of this figure is available in the online journal.)

explosion and have not been observed during the previous outbursts of SN 2009ip (see Smith et al. 2010b; Foley et al. 2011; Pastorello et al. 2013).

As the photosphere recedes into the ejecta it illuminates material moving toward the observer with different velocities. We identify He I, Na I D and H I absorbing at three typical velocities (Figure 22). The blue absorption edge of He I plus Na I D extends to $v \approx 18{,}000\,\mathrm{km\,s^{-1}}$, as noted by Mauerhan et al. (2013). High-velocity $v \sim -12{,}000\,\mathrm{km\,s^{-1}}$ absorption appears first, around $t_{pk} + 9$ days, followed by the $v \sim -5500\,\mathrm{km\,s^{-1}}$ absorption around $t_{pk} + 28$ days, which in turn is followed by slower material with $v \sim -2500\,\mathrm{km\,s^{-1}}$, seen in absorption starting only from $\sim t_{pk}+60$ days. This happens because material with lower velocity naturally overtakes the photosphere at later times. Material moving at three distinct velocities provides an argument against a continuous distribution in velocity of the ejecta and suggests instead the presence of distinct shells of ejecta expanding with typical velocity $v \sim -12{,}000\,\mathrm{km\,s^{-1}}$, $v \sim -5500\,\mathrm{km\,s^{-1}}$, and $v \sim -2500\,\mathrm{km\,s^{-1}}$.

4.6. UV Spectral Properties

We do not find evidence for strong spectral evolution at UV wavelengths (Figures 3 and 5). As time proceeds the Fe III

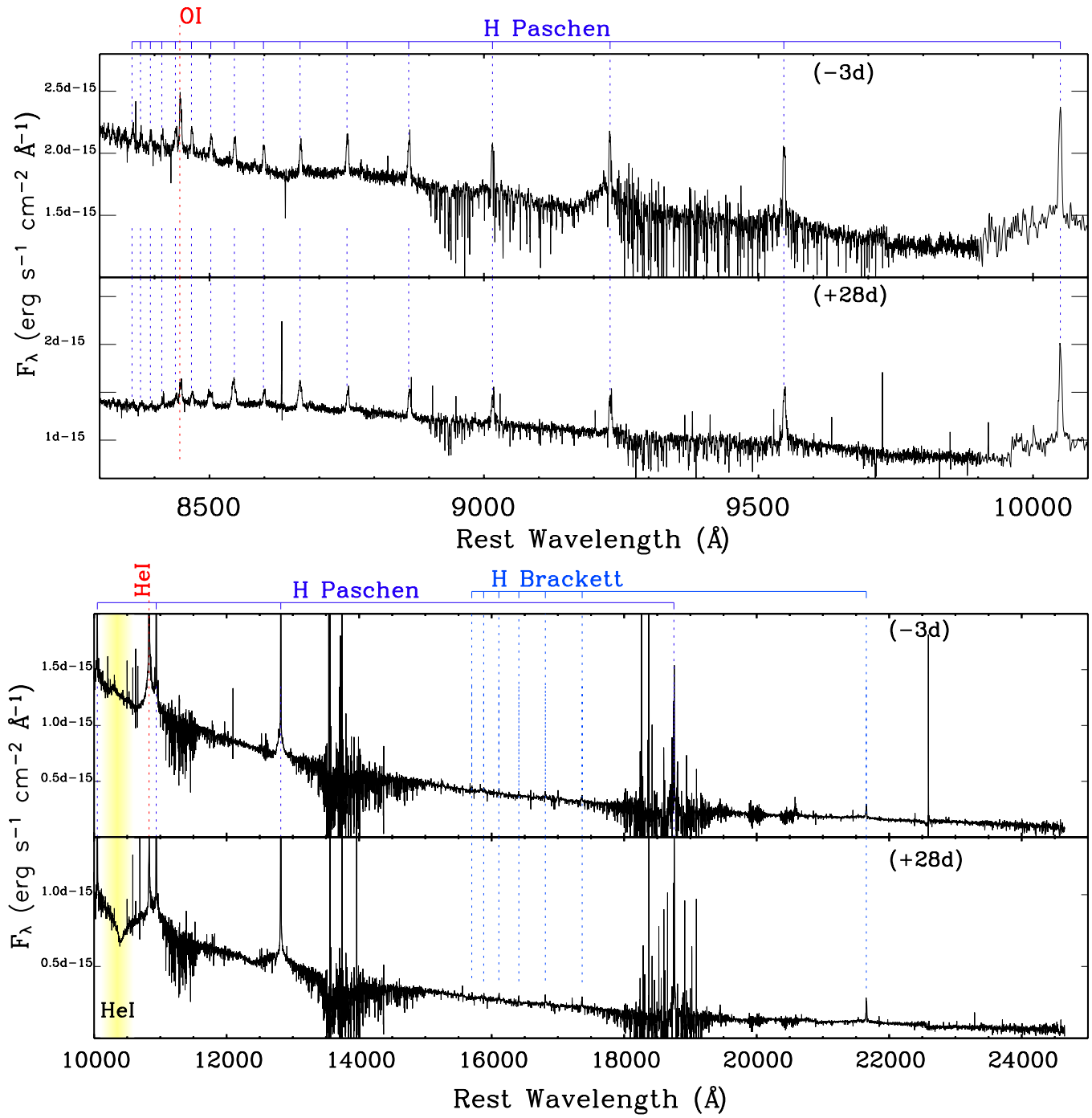

Figure 20. High-resolution VLT/X-shooter spectra from 10000 to 24500 Å . Continued from Figure 19.
(A color version of this figure is available in the online journal.)

absorption features become weaker while Fe II develops stronger absorption features, consistent with the decrease of the photosphere temperature with time (Figure 11). UVOT spectra show the emergence of emission around 2500–3000 Å that is later well resolved by *HST*/STIS as emission from Mg II λλ2796, 2803 lines as well as Fe II multiplets at ∼2550, 2630, 2880 Å (Figure 4). The Mg II line profiles are similar to the H I line profiles, with a narrow component and broad, blue-shifted absorption features.

We further identify strong, narrow emission from N II] at λλ2140, 2143 and possible emission from C III] (λ1909) and Si III] (λλ1892, 1896).

At shorter wavelengths, we find a mixture of high and low ionization lines (Figure 4, lower panel). We identify strong lines of C II (λλ1334.5, 1335.7), O I (λλ1302.2–1306.0), Si II (λλ1526.7, 1533.5). Of the higher ionization lines one notes C IV (λλ1548.2, 1550.8) and N V (λλ1238.8, 1242.8). Interestingly, N IV] λ1486.5 is either very weak or absent, which indicates a medium with density $n \gtrsim 10^9\,\mathrm{cm}^{-3}$. Fe II is also present and Lyα emission is also very well detected.

At $t \approx t_{\rm pk} + 34$ days, both the optical, NIR, and UV spectra are dominated by permitted transitions. Despite the presence of high ionization lines there are no forbidden lines of, e.g., [O III] λλ4959, 5007, N IV] λλ1486 or O III] λλ1664, which is

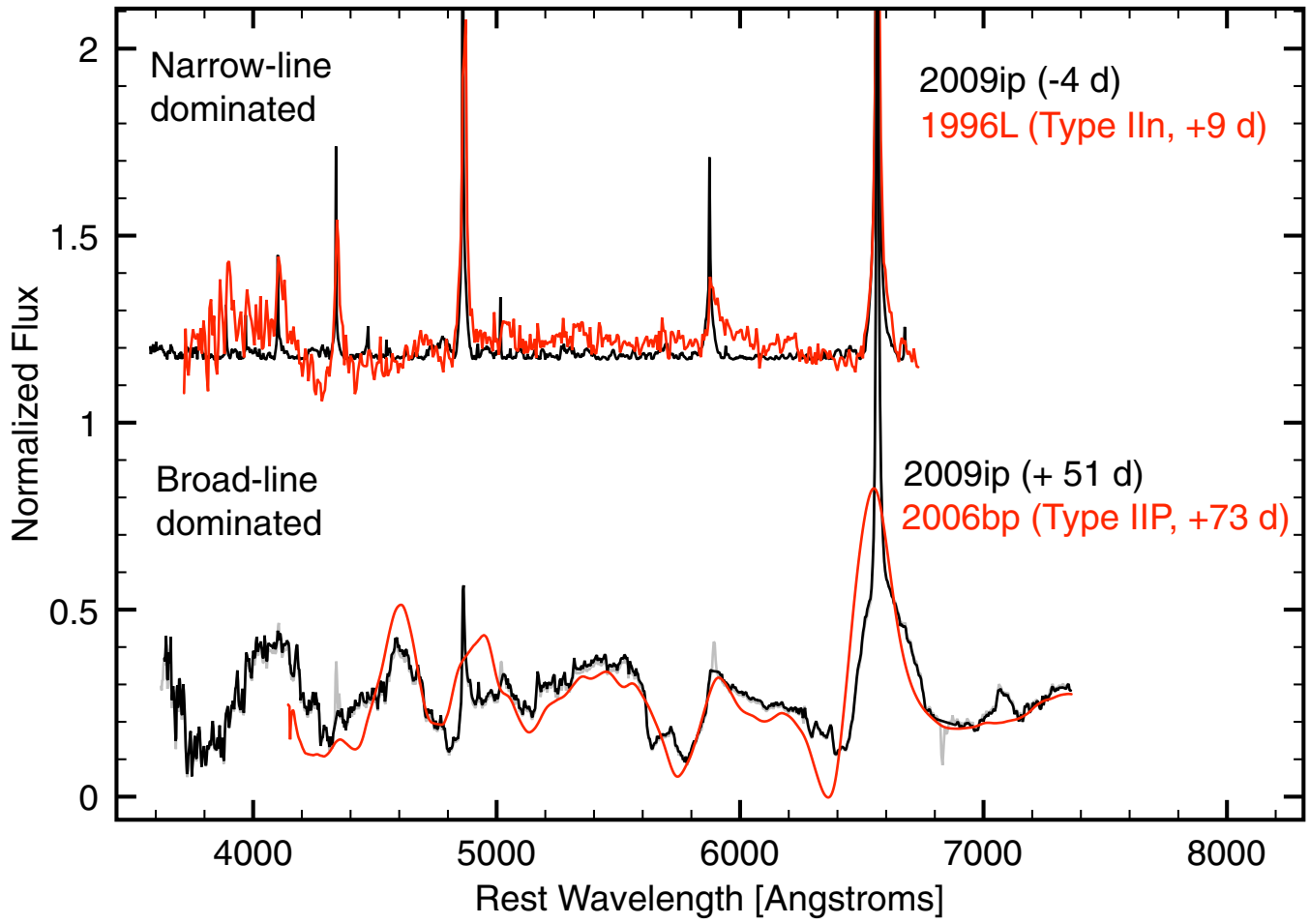

Figure 21. SN 2009ip evolved from a narrow-line dominated spectrum typical of Type IIn SN explosions (e.g., SN 1996L, Benetti et al. 1999) to a spectrum that clearly shows broad absorption features more typical of Type IIP SNe (like SN 2006bp, Quimby et al. 2007).

(A color version of this figure is available in the online journal.)

consistent with the picture of high density in the line forming region. The main exceptions are the [N II] λλ2140, 2143 lines (Figure 4). The explanation could be a comparatively high critical density, i.e., $\sim 3 \times 10^9$ cm^{-3} in combination with a high N abundance.

Interestingly, a comparison of high (C IV λλ1548.2, 1550.8 and N V λλ1238.8, 1242.8) and low (C II λ1335) ionization emission line profiles in velocity space reveals no significant difference.

The mixture of low and high ionization lines indicates that there might be different density components or different ionization zones present in the line emitting region. The similar line profiles argue for a similar location of the ionization zones, supporting the idea of a complex emission region with different density components.

5. METALLICITY AND HOST ENVIRONMENT

The final fate of a massive star is controlled by the mass of its helium core (e.g., Woosley et al. 2007), which strongly depends on the initial stellar mass, rotation, and composition. Metallicity has a key role in determining the mass-loss history of the progenitor, with low metallicity generally leading to a suppression of mass loss, therefore allowing lower-mass stars to end their lives with massive cores. SN 2009ip is positioned in the outskirts of NGC 7259 (Figure 1). The remote location of SN 2009ip has been discussed by Fraser et al. (2013). Our data reveal no evidence for an H II region in the vicinity of SN 2009ip. Thus, we inferred the explosion metallicity by measuring the host galaxy metallicity gradient. We measure the metallicity gradient of the host galaxy of SN 2009ip (NGC 7259), using our longslit spectroscopy from the Goodman Spectrograph on the SOAR telescope obtained on December 14 (see Table 2 in Appendix D). The longslit was placed along the galaxy center at parallactic angle. We extracted spectra of the galaxy at positions in a sequence across our slit, producing a set of integrated light spectra from ∼0 to 2 kpc from either side of the galaxy center.

We use the "PP04 N2" diagnostic of Pettini & Pagel (2004) to estimate gas phase metallicity using the Hα and [N II] λ6584 emission lines. We estimate the uncertainty in the metallicity measurements by Monte Carlo propagation of the uncertainty in the individual line fluxes. Robust metallicity profiles cannot be recovered in other diagnostics due to the faintness of the [O III] lines in our spectroscopy.

Figure 23 shows the resulting metallicity profile of NGC 7259. The metallicity at the galaxy center is log(O/H) + 12 = ∼8.8, ∼1.3 $Z_\odot$ on the PP04 N2 scale, but declines sharply with radius. The metallicity profiles on each side of the galaxy center in our longslit spectrum are consistent. We therefore assume azimuthal symmetry. We estimate the metallicity gradient by fitting a linear profile. The best-fit gradient intercept and slope are 8.8 ± 0.02 dex and −0.11 ± 0.02 dex kpc^{-1}, respectively.

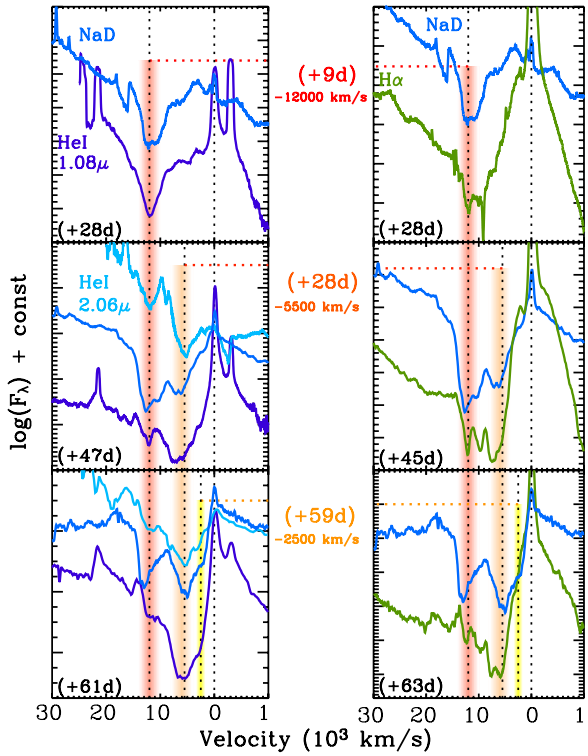

Figure 22. Evolution of the broad absorption features associated with Hα, He I, and Na I D lines. As the photosphere recedes into the ejecta broad absorption features appear in the spectra with three typical velocities: $v \sim -12{,}000\,\mathrm{km\,s^{-1}}$ (red band), $v \sim -5500\,\mathrm{km\,s^{-1}}$ (orange band), and $v \sim -2500\,\mathrm{km\,s^{-1}}$ (yellow band). Absorption features at higher velocity are revealed at earlier times.

(A color version of this figure is available in the online journal.)

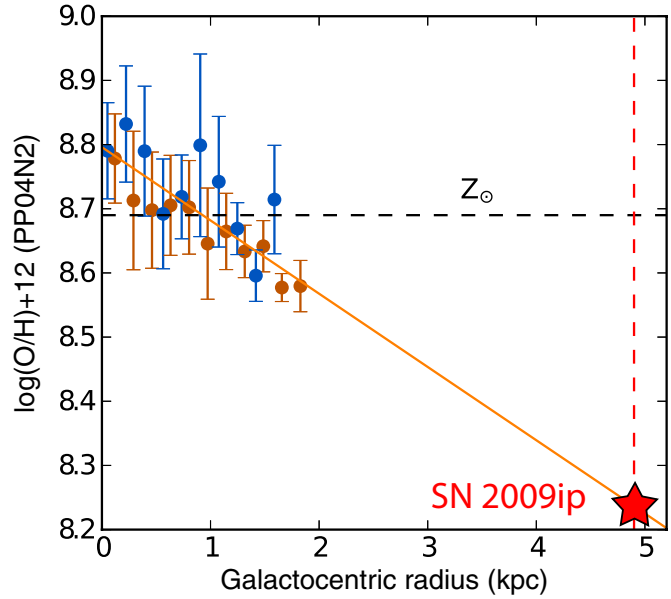

Figure 23. Metallicity profile of the host galaxy of SN 2009ip, NGC 7259, with best-fitting metallicity gradient. The vertical dashed line marks the SN galactocentric radius. The colors distinguish measurements from opposite sides of the galaxy center. We find $8.2 < \log(\mathrm{O/H}) + 12 < 8.6$ ($0.4\,Z_\odot < Z < 0.9\,Z_\odot$) at the explosion site of SN 2009ip.

(A color version of this figure is available in the online journal.)

SN 2009ip is located ~43″.4 from the center of the galaxy NGC 7259 (equal to ~5.0 kpc at $d_\mathrm{L} = 24$ Mpc). Extrapolating directly from this gradient would imply an explosion site metallicity of $\log(\mathrm{O/H}) + 12 = \sim 8.2$, or $\sim 0.4\ Z_\odot$. This metallicity would place SN 2009ip at the extreme low metallicity end of the distribution of observed host environments of Type II SN (Stoll et al. 2013), and nearer to the low metallicity regime of broad-lined Type Ic SNe (Kelly & Kirshner 2012; Sanders et al. 2012). However, the metallicity properties of galaxies at distances well beyond a scale radius have not been well studied. It is likely that a simple extrapolation is not appropriate, and the metallicity profile in the outskirts of the galaxy may flatten (Werk et al. 2011) or drop significantly (Moran et al. 2012). In either case, it is unlikely that the explosion site metallicity is significantly enriched relative to the gas we observe at $R \sim 2$ kpc, with $\log(\mathrm{O/H}) + 12 \sim 8.6$ ($\sim 0.9\ Z_\odot$). If we adopt this value as the explosion site metallicity, it is fully consistent with the observed distribution of SNe II, Ib, and Ic (Kelly & Kirshner 2012; Sanders et al. 2012; Stoll et al. 2013).

Our best constraint on the explosion site metallicity is therefore $0.4\,Z_\odot < Z < 0.9\,Z_\odot$, pointing to a (mildly) subsolar environment.

6. ENERGETICS OF THE EXPLOSION

The extensive photometric coverage allows us to accurately constrain the bolometric luminosity and total energy radiated by SN 2009ip. SN 2009ip reaches a peak luminosity of $L_\mathrm{pk} = (1.7 \pm 0.1) \times 10^{43}\,\mathrm{erg\,s^{-1}}$ (Figure 11). The total energy radiated during the 2012a outburst (from 2012 August 1 to September 23) is $(1.5 \pm 0.4) \times 10^{48}$ erg while for the 2012b explosion we measure $E_\mathrm{rad2} = (3.2 \pm 0.3) \times 10^{49}$ erg. As much as ~35% of this energy was released before the peak, while 50% of E_rad2 was radiated during the first ~15 days. Subsequent rebrightenings, (which constitute a peculiarity of SN 2009ip) only contributed to small fractions of the total energy.

The peak luminosity of SN 2009ip is not uncommon among the heterogeneous class of SNe IIn, corresponding to $M_\mathrm{R} \approx -18$ mag (Figure 24). Its radiated energy of $(3.2 \pm 0.3) \times 10^{49}$ erg falls instead into the low-energy tail of the distribution mainly because of the very rapid rise and decay times of the bolometric luminosity (Figure 25). A comparable amount of energy of $\sim 3 \times 10^{49}$ erg was radiated by the Type IIn SN 2011ht (Roming et al. 2012), which however showed a much longer rise time (~55 days) and a less luminous peak ($M_\mathrm{V} \sim -17$). As in the case of SN 2011ht (Humphreys et al. 2012), the limited energy radiated by SN 2009ip brings into question the final fate of the progenitor star: was the total energy released sufficient to fully unbind the star (i.e., terminal explosion) or does SN 2009ip results from a lower-energy ejection of only the outer stellar envelope (i.e., nonterminal explosion)? This topic is explored in Section 8. Indeed, stars might be able to survive eruptive/explosive events that reach a visual absolute magnitude of $M_\mathrm{vis} \approx -17$ mag (e.g., SN 1961V in Figure 25; Van Dyk & Matheson 2012; Kochanek et al. 2011), so that the peak luminosity is *not* a reliable indicator of a terminal versus nonterminal explosion.[38] With an estimated radiated energy of 3.2×10^{49} erg (total energy of 2×10^{50} erg; Davidson & Humphreys 1997) the "Great Eruption" of η-Carinae (see Davidson & Humphreys 2012 and references therein) demonstrated that it is also possible to survive the

[38] The same line of reasoning applies to the velocity of the fastest moving material, as pointed out by Pastorello et al. (2013): very fast material with $v \sim 12{,}500\,\mathrm{km\,s^{-1}}$ was observed during the outburst of SN 2009ip of 2011 September, proving that high-velocity ejecta can be observed even without a terminal explosion.

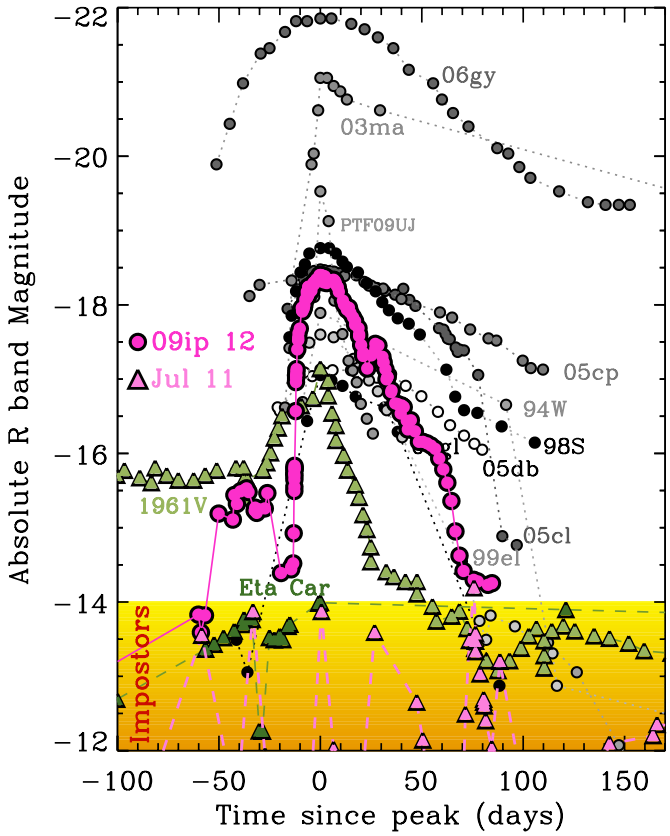

Figure 24. Absolute R-band magnitude of SN 2009ip (pink dots) compared to the sample of Type IIn SNe with R-band photometric coverage around the peak (from Kiewe et al. 2012; Ofek et al. 2010). Colored area: typical absolute magnitude of LBV-like eruption episodes. Pink triangles mark the luminosity of SN 2009ip during the 2011 outburst ($t = 0$ corresponds here to 2011 July 8 for convenience). The exceptional SN (impostor?) SN1961V (photographic plate magnitudes; from Pastorello et al. 2013) and η-Carinae during the 19th century Great Eruption ($M_{\rm vis}$ as compiled by Frew 2004; see also Smith & Frew 2011) are shown with green triangles. The comparison with SN 2010mc is shown in Figure 29.

(A color version of this figure is available in the online journal.)

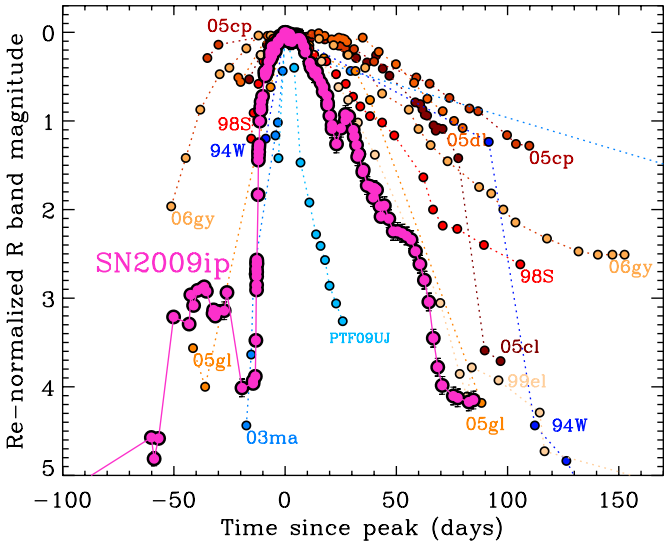

Figure 25. Renormalized R-band magnitude of SN 2009ip compared with the sample of SNe IIn of Figure 24. Shades of orange (blue) are used for SNe with a slower (faster) rise time. SN 2009ip is characterized by a fast rise and fast decay.

(A color version of this figure is available in the online journal.)

release of comparable amount of energy, even if on timescales much longer than those observed for SN 2009ip (the "Great Eruption" lasted about 20 yr). A nonterminal explosion has also been recently suggested to interpret the Type IIn SN 1994W (Dessart et al. 2009) and SN 2011ht (Humphreys et al. 2012).

SN 2010mc shows instead striking similarities to SN 2009ip both in terms of timescales and of released energy (Figure 29). As in SN 2009ip, a precursor bump was detected ∼40 days before the major outburst. Ofek et al. (2013b) calculate $E_{\rm rad} > 6 \times 10^{47}$ erg (precursor bump) and $E_{\rm rad} \sim 3 \times 10^{49}$ erg (major outburst) for SN 2010mc, compared with $E_{\rm rad1} = (1.5 \pm 0.4) \times 10^{48}$ erg and $E_{\rm rad2} = (3.2 \pm 0.3) \times 10^{49}$ erg we calculated above for SN 2009ip. The very close similarity of SN 2010mc and SN 2009ip originally noted by Smith et al. (2013) has important implications on the nature of both explosions (see Section 8).

7. SOURCE OF ENERGY AND PROPERTIES OF THE IMMEDIATE ENVIRONMENT

In the previous sections we concentrated on the properties of the explosion and its environment that can be directly measured; here we focus on properties that can be inferred from the data.

The light-curve of SN 2009ip shows two major episodes of emission: the precursor bump (2012a outburst) and the major rebrightening (2012b explosion). Is this phenomenology due to two distinct explosions or is the double-peaked light-curve the result of a single explosion? Models where the first bump in the light-curve is a SN explosion while the second peak is due to the interaction of the SN ejecta with the CSM (Mauerhan et al. 2013) belong to the "single-explosion" category. In the following we proceed instead with a two-explosion hypothesis and argue that we witnessed two separate but causally connected explosions from the progenitor of SN 2009ip. This scenario has the advantage of naturally explaining the appearance of faster moving material during the 2012b outburst.

7.1. Limit on the Nickel Mass Synthesized by the 2012b Explosion

Narrow emission lines in the optical spectra of SN 2009ip require that interaction with previously ejected material (either in the form of a stable wind or from erratic mass-loss episodes) is occurring at some level. The multiple outbursts of SN 2009ip detected in the 2009, 2011 and 2012 August (from 3 yr to ∼1 month before the major 2012 explosion) are likely to have ejected conspicuous material in the immediate progenitor surroundings so that interaction of the 2012b explosion shock with this material qualifies as an efficient way to convert kinetic energy into radiation.

The radioactive decay of ^{56}Ni represents another obvious source of energy. We employ the nebular phase formalism developed by Valenti et al. (2008; expanding on the original work by Sutherland & Wheeler 1984 and Cappellaro et al. 1997) to constrain the amount of nickel synthesized by the 2012b explosion using late-time observations. If the observed light-curve were to be entirely powered by the energy deposition of the ^{56}Ni radioactive decay chain, our latest photometry would imply $M_{\rm Ni} \sim 0.03\,M_\odot$ for a standard explosion kinetic energy of $E_k = 10^{51}$ erg. For a low-energy explosion with $E_k = 10^{50}$ erg, $M_{\rm Ni} \sim 0.08\,M_\odot$. Allowing for other possible sources of energy contributing to the observed luminosity (like interaction), we conclude $M_{\rm Ni} < 0.08\,M_\odot$. Using this value (and the photospheric formalism by Valenti et al. 2008 based on Arnett

1982) we largely underpredict the luminosity of SN 2009ip at peak for any value of mass and kinetic energy of the ejecta: the energy release of SN 2009ip is therefore not powered by ^{56}Ni radioactive decay. Fraser et al. (2013) independently derived $M_{\rm Ni} < 0.02\,M_\odot$, consistent with our findings. A very low ^{56}Ni yield (not sufficient to power the optical light-curve) was also reported by Dessart et al. (2009) and Humphreys et al. (2012) for SNe 1994W and 2011ht, respectively. Interestingly, in both cases these authors suggested a nonterminal explosion.

In the following we explore a model where the major UV-bright peak of SN 2009ip is powered by shock break-out from material ejected by the precursor bump, while continued interaction with previously ejected material is responsible for the peculiar, bumpy light-curve that follows.

7.2. Shock Break-Out Plus Continued Interaction Scenario for the 2012b Explosion

The rapid rise and decay times of the major 2012b explosion (Figure 25) suggest that the shock wave is interacting with a compact shell(s) of material (see, e.g., Chevalier & Irwin 2011, their Figure 1). The relatively fast fading of CSM-like features and subsequent emergence of Type IIP features shown in Figure 21 supports a similar conclusion. We consider a model where the ejecta from the 2012b explosion initially interact with an optically thick shell of material, generating the UV-bright, major peak in the light-curve. In our model, the light-curve is powered at later times by interaction with optically thin material.

In the shock break-out scenario the escape of radiation is delayed with respect to the onset of the explosion until the radiation is able to break-out from the shell at an optical depth $\tau_{\rm w} \approx c/v_{\rm sh}$. This happens when the diffusion time $t_{\rm d}$ becomes comparable to the expansion time. Radiation is also released on the diffusion timescale, which implies that the observed bolometric light-curve rise time is $t_{\rm rise} \approx t_{\rm d}$. Following Chevalier & Irwin (2011; see also Nakar & Sari 2010), the radiated energy at break-out $E_{\rm rad}$, the diffusion time $t_{\rm d}$ and the radius of the contact discontinuity at $t = t_{\rm d}$ ($\equiv R_{\rm bo}$) depend on the explosion energy E, the ejecta mass $M_{\rm ej}$, the environment density $\rho_{\rm w}$ (parameterized by the progenitor mass-loss rate) and opacity k. From our data we measure: $t_{\rm rise} \approx 10$ days; $R_{\rm bo} \approx 5 \times 10^{14}$ cm; $E_{\rm rad} \approx 1.3 \times 10^{49}$ erg. We solve the system of equations for our observables in Appendix A and obtain the following estimates for the properties of the explosion and its local environment. Given the likely complexity of the SN 2009ip environment, those should be treated as order of magnitudes estimates.

The onset of the 2012b explosion is around 20 days before peak (2012 September 13). Using Equations (A2) and (A3), the progenitor mass-loss rate is $\dot{M} \approx 0.07(v_{\rm w}/200\,{\rm km\,s^{-1}})\,M_\odot\,{\rm yr}^{-1}$. We choose to renormalize the mass-loss rate to $200\,{\rm km\,s^{-1}}$, which is the FWHM of the narrow emission component in the Hα line (e.g., Figure 16). We note that the inferred temporary mass-loss rate is appreciably below the expectations from a terminal explosion, but considerably higher than LBVs at maximum (which typically have $\dot{M} \approx 10^{-4}$–$10^{-5}\,M_\odot\,{\rm yr}^{-1}$; Humphreys & Davidson 1994). A similar temporary mass loss was obtained by Humphreys et al. (2012) for the Type IIn SN 2011ht in the "hot wind phase," which they interpret as a nonterminal event.

The observed bolometric luminosity goes below the level of the luminosity expected from continued interaction (Equation (A6)) around $t_{\rm pk}$+12 days. By this time she shock must have reached the edge of the dense wind shell: $t_{\rm w} \lesssim 32$ days. This constrains the wind shell radius to be $R_{\rm w} \approx 1.2 \times 10^{15}$ cm (Equation (A7)), therefore confirming the idea of a compact and dense shell of material, while the total mass in the wind shell is $M_{\rm w} \approx 0.1\,M_\odot$ (Equation (A5)).[39] The system of equations is degenerate for $M_{\rm ej}/E^2$. Adopting our estimates of the observables above and Equation (A1) we find $M_{\rm ej} \approx 50.5(E/10^{51}\ {\rm erg})^2\,M_\odot$.[40] The efficiency of conversion of kinetic energy into radiation depends on the ratio of the total ejecta to wind shell mass (e.g., van Marle et al. 2010; Ginzburg & Balberg 2012; Chatzopoulos et al. 2012). This suggests $M_{\rm ej} \approx M_{\rm w}$ as order of magnitude estimate, from which $E \sim 10^{50}$ erg.

After $t_{\rm w}$ the bolometric luminosity starts to decay faster, especially at UV wavelengths (Figure 2). Around this time the shock starts to interact with less dense, optically thin layers of material producing continued power for SN 2009ip. In this regime the observed luminosity tracks the energy deposition rate: $L = 4\pi R^2 \rho_{\rm w}(v_{\rm fs} - v_{\rm w})^3$, where R is the radius of the cold dense shell that forms as a result of the loss of radiative energy from the shocked region; $v_{\rm fs}$ is the forward shock velocity; $v_{\rm w}$ and $\rho_{\rm w}$ are the velocity and density of the material encountered by the shock wave (Chevalier & Irwin 2011, and references therein). Given the complexity of the explosion environment, we adopt a simplified shock interaction model (see, e.g., Smith et al. 2010a) and parameterize the observed luminosity as: $L = (\eta/2)wv^3$, where η is the efficiency of conversion of kinetic energy into radiation; $w(R) \equiv \dot{M}/v_{\rm w}$ (hence $\rho_{\rm w} = w(R)/4\pi R^2$); while v is a measure of the expansion velocity of the shock into the environment. We use $v \approx 5000\,{\rm km\,s^{-1}}$. Using the bolometric luminosity of Figure 11, we find that the total mass swept up by the shock from $t_{\rm w} = 32$ days until the end of our monitoring (112 days since explosion) is $M_{\rm w}^{\rm thin} \approx (0.05/\eta)\,M_\odot$. The total mass in the environment swept up by the 2012b explosion shock is therefore $M_{\rm tot} = M_{\rm w} + M_{\rm w}^{\rm thin} \approx (0.2$–$0.3)\,M_\odot$ for $\eta = 50\%$–30%. As a comparison, Ofek et al. (2013a) derive a mass of $\sim$0.1 $M_\odot$. Our analysis points to a steep density profile with $\rho_{\rm w} \propto R^{-5}$ for $R > 1.4 \times 10^{15}$ cm.

7.3. Origin of the Interacting Material in the Close Environment

During the 2012b explosion, the shock interacts with an environment that has been previously shaped by the 2012a explosion and previous eruptions. In this section we infer the properties of the pre-2012a explosion environment, using the 2012a outburst as a probe. We look to (1) understand the origin of the compact dense shell with which the 2012b shock interacted, whether it is newly ejected material by the 2012a outburst or material originating from previous eruptions, (2) constrain the nature of the slowly moving material ($v \approx$ a few $100\,{\rm km\,s^{-1}}$) responsible for narrow-line emission in our spectra.

We put an upper limit on the total amount of mass in the surroundings of SN 2009ip before the 2012a explosion assuming that the observed luminosity of the 2012a outburst is entirely powered by optically thin shock interaction with some previously ejected material of mass $M_{\rm w}^{\rm 12a}$. As before, $L = (\eta/2)wv^3$. $M_{\rm w}^{\rm 12a} = \int w(R)dR$. The evolution of the blackbody radius of Figure 11 suggests $v \approx 2500\,{\rm km\,s^{-1}}$

[39] The mass swept up by the shock by the time of break-out is $\approx$0.05 $M_\odot$.

[40] Using the line of reasoning of Section 7.1, the relation between $M_{\rm ej}$ and E just found implies $M_{\rm Ni} < 0.02\,M_\odot$ for $E = 10^{51}$ erg and $M_{\rm Ni} < 0.07\,M_\odot$ for $E = 10^{50}$ erg, consistent with the limits presented in Section 7.1.

before 2012 August 21. We apply the same line of reasoning as above and assume that the shock continues to expand with this velocity, while the photosphere transitions to the thin regime and stalls at $\approx 0.4 \times 10^{15}$ cm. In this picture, the 2012a shock sampled the environment on distances $R < 1.2 \times 10^{15}$ cm, sweeping up a total mass of $M_{\rm w}^{\rm 12a} \leqslant (0.02/\eta)\, M_\odot$. In Section 7.2 we estimated that the total mass of the dense wind shell from which the 2012b shock breaks out is $M_{\rm w} \approx 0.1\, M_\odot$ with radius $R_{\rm w} \approx 1.2 \times 10^{15}$ cm. The wind shell mass is $M_{\rm w} = M_{\rm w}^{\rm 12a}(R < R_{\rm w}) + M_{\rm ej}^{\rm 12a}(R < R_{\rm w})$, where $M_{\rm ej}^{12a}(R < R_{\rm w})$ is the portion of the ejecta mass of the 2012a explosion within $R_{\rm w}$ at $t = t_{\rm w}$. This implies $M_{\rm ej}^{12a}(R < R_{\rm w}) > 0.06\, M_\odot (>0.09\, M_\odot)$ for our fiducial efficiency $\eta = 30\%$ ($\eta = 50\%$), comparable with the mass of the dense wind shell.

We conclude that the UV-bright 2012b explosion results from shock break-out from material ejected by the 2012a explosion, therefore establishing a direct connection between the properties of the 2012a and 2012b episodes.

The previous result also implies a solid lower limit on the total ejecta mass of the 2012a outburst: $M_{\rm ej}^{12a} > 0.06\, M_\odot (>0.09\, M_\odot)$ for $\eta = 30\%$ ($\eta = 50\%$). In Section 7.2 we estimated that the total mass collected by the 2012b shock by the end of our monitoring is $M_{\rm tot} \approx 0.2$–$0.3\, M_\odot$, which constrains $0.06 < M_{\rm ej}^{12a} < 0.3\, M_\odot$ for $\eta \geqslant 30\%$. In the following we use $M_{\rm ej}^{12a} \approx 0.1\, M_\odot$ as an order of magnitude estimate for the mass ejected by the 2012a outburst.

Our spectra show evidence for narrow-line emission (Section 4) typically observed in SNe IIn (and LBVs), which is usually interpreted as signature of the ejecta interaction with material deposited by the progenitor wind before explosion. For SN 2009ip we observe during the 2012b event a velocity gradient in the narrow emission from Hα (Figure 16, panel (c)), with increasing velocity with time. This increase is consistent with being linear with time. This might suggest a Hubble-like expansion for the CSM following the simple velocity profile $v \propto R$: as time goes by, the shock samples material at larger distances from the explosion (hence with larger velocity v). Our analysis indicates that episodes of mass ejection with approximate age 11–19 months before the 2012b explosion (roughly between 2011 February and October) might reasonably account for the observed velocity gradient. We suggest that CSM material in the surroundings of SN 2009ip moving at velocities of hundreds km s^{-1} originates from this sudden episode(s) of mass ejection. Remarkably, SN 2009ip has been reported to be in eruptive phase between 2011 May and October (Pastorello et al. 2013), consistent with this picture.

The Hubble-like flow is not consistent with a steady wind and points instead to some mechanism leading to explosive mass ejections. Interestingly, it is during the 2011 September outburst that SN 2009ip showed evidence for material with unprecedented velocity, reaching $v = 12{,}500$ km s^{-1} (Pastorello et al. 2013). Since no line-driven or continuum-driven wind mechanism is known to be able to accelerate stellar surface material to these velocities (Mauerhan et al. 2013), stellar-core-related mechanisms have to be invoked. The explosive mass ejection suggested by our analysis might therefore be linked to instabilities developing deep inside the stellar core.

Davidson & Humphreys (2012) and Humphreys et al. (2012) however point out that giant eruptions driven by super-Eddington radiation might also develop a shock able to accelerate a limited amount of material to supersonic speeds. In this case, no core-related explosion would be involved. This model has been successfully applied to the Type IIn SN 2011ht (which however does not show evidence for material with $v > 600$ km s^{-1}; Humphreys et al. 2012) and might explain the giant eruption of η-Carinae (Davidson & Humphreys 2012). It is at the moment unclear if the same mechanism would be able to explain the very high velocities observed in the ejecta of SN 2009ip.

7.4. The Role of Asymmetries in SN 2009ip

The analysis of Section 4.5 indicates the presence of ejecta traveling at three distinct velocities: $v \sim -12{,}000$ km s^{-1}, $v \sim -5500$ km s^{-1}, and $v \sim -2500$ km s^{-1}. These values correspond to the velocity of material seen in absorption (i.e., placed outside the photosphere). The radius of the hot blackbody $R_{\rm HOT}$ of Figure 11 tracks the position of the photosphere with time. Assuming free expansion of the ejecta and the explosion onset time ($t_{\rm pk} - 20$ days) derived in the previous sections, we can predict at which time t_v ejecta moving at a certain velocity v will overtake the photosphere at $R_{\rm HOT}$. Only for $t \gtrsim t_{\rm v}$ can the ejecta give rise to absorption features in the spectra. Spherical symmetry is an implicit assumption in the calculation of $R_{\rm HOT}$, so that comparing the predicted $t_{\rm v}$ to the observed time of appearance of the absorption edges makes it possible to test the assumption of spherical symmetry of the explosion.

For $v \sim -2500$ km s^{-1} we find $t_{\rm v} = t_{\rm pk} + 55$ days (2012 November 27) in excellent agreement with our observations, which constrain the $v \sim -2500$ km s^{-1} absorption edge to appear between 2012 November 23 and December 5 (Figure 22). No departure from spherical symmetry needs to be invoked for slow-moving ejecta, which likely includes most of the ejecta mass.[41] Spherical symmetry is instead broken by the high-velocity material traveling at $v \sim -12{,}000$ km s^{-1}. For the 2012b explosion we detect high-velocity material in absorption starting from $\sim$1 week after peak. Around peak the spectrum of SN 2009ip is optically thick and shows no evidence for material with $v \sim -12{,}000$ km s^{-1} (Figures 19 and 20). However, in no way could a perfectly spherical photosphere with apparent $v \approx 4000$–5000 km s^{-1} mask the fast-moving ejecta at any time during the evolution, and in particular until the first week after peak, as we observed. This indicates a departure of the high-velocity ejecta from spherical geometry and might suggest the presence of a preferred direction in the explosion.

Asymmetry can also have a role in the spatial distribution of the interacting material, as supported by the observed co-existence of broad and (unresolved) intermediate components in the spectrum (Figure 14). In this respect, Chugai & Danziger (1994) proposed the possibility of an enhanced mass loss on the equatorial plane of SNe IIn to explain the intermediate velocity component in SN 1988Z, other explanations being a clumpy CSM or, again, an asymmetric flow. Humphreys et al. (2012), with reference to SN 2011ht, emphasized that an asymmetric outflow would strongly modify the observed spectrum. In this context it is worth noting that asymmetry is also a likely explanation for the discrepant mass-loss estimates found by Ofek et al. (2013a), as noted by the authors. A disk-like geometry for SN 2009ip was proposed by Levesque et al. (2012) based on the H Balmer decrement. Finally, the binary-star merger scenario proposed by Soker & Kashi (2013) to interpret SN 2009ip naturally leads to ejecta with a bipolar structure.

[41] Note, however, that in no way this argument can be used as a proof of spherical symmetry.

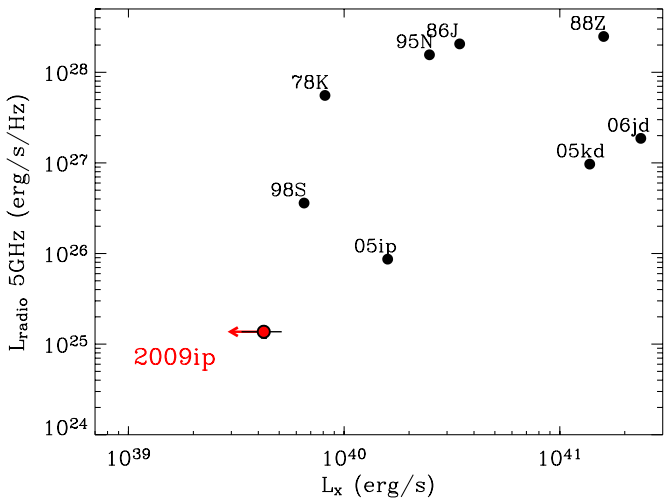

Figure 26. Radio luminosity at peak vs. X-ray luminosity at the radio peak for a sample of Type IIn SNe (black dots). SN 2009ip is shown in red. Data have been collected from the literature (Pooley et al. 2002; Smith et al. 2007; Stritzinger et al. 2012; Chandra et al. 2009, 2012a; Pooley et al. 2007; Chandra & Soderberg 2007; Zampieri et al. 2005; Houck et al. 1998; Chevalier 1987; van Dyk et al. 1993; Fabian & Terlevich 1996 and references therein).

(A color version of this figure is available in the online journal.)

7.5. X-Rays from Shock Break-Out and Continued Interaction

SN 2009ip is a weak X-ray and radio emitter (Figure 26). In the following two sections we connect the lack of high X-ray/radio luminosity to the shock break-out plus interaction scenario. This scenario gives rise to a two-component high-energy spectrum, with a hard (X-rays) and a soft (UV/optical, at the break-out velocity of interest here) component (e.g., Svirski et al. 2012; Chevalier & Irwin 2012). The hard component is generated by bremsstrahlung emission from hot electrons behind the shock. Theory predicts that $L_{\rm hard,bo} \sim 10^{-4}\,L_{\rm bo}$ (where $L_{\rm bo}$ is the break-out luminosity, resulting from the soft and hard component) as long as: (1) inverse Compton (IC) cooling dominates over bremsstrahlung; (2) high-energy photons undergo Compton degradation in the unshocked wind during their diffusion to the observer. We show in the following that both processes are relevant for SN 2009ip and provide a natural explanation for its very low X-ray to optical luminosity ratio ($L_{\rm x}/L_{\rm optical} \lesssim 10^{-4}$).

From our modeling of Section 7.2, we inferred a density parameter $D_* \approx 0.4$ (see Appendix A for a definition of D_*). With a shock velocity $v \sim 4500\,{\rm km\,s^{-1}}$ (or larger), the density measurement above implies that around break-out time the main source of cooling of the hot electrons is IC (see Chevalier & Irwin 2012). For our parameters, the bremsstrahlung (ff) to IC emissivity ratio at break-out is (Svirski et al. 2012, their Equation (17)) $\epsilon^{\rm ff}/\epsilon^{\rm IC} \approx 0.01\,(v/10^9\,{\rm cm\,s^{-1}})^{-2}$ or $\epsilon^{\rm ff}/\epsilon^{\rm IC} \approx 0.05$. IC is the dominant cooling source, suppressing the emission of hard photons in SN 2009ip. The calculations by Ofek et al. (2013a) instead assume negligible IC cooling.

Comptonization of the hard photons as they propagate through the unshocked wind region to the observer furthermore leads to a suppression of high-energy radiation. This process can effectively suppress photons with ≈keV energy if $\tau_{\rm es} \gtrsim 15$–20, the photon energy being limited by $\epsilon_{\rm max} = 511/\tau_{\rm es}^2$ keV. Our modeling of Section 7.2 implies $\tau_{\rm es} \approx 15$ for SN 2009ip around break-out. This demonstrates that both the domination of IC over bremsstrahlung (1) and Compton losses (2) are relevant to explain the weak X-ray emission in SN 2009ip. Identifying $L_{\rm x}$ with $L_{\rm hard}$ and $L_{\rm bol}$ with $L_{\rm bo}$, the shock break-out scenario therefore naturally accounts for the observed $L_{\rm x}/L_{\rm optical} \lesssim 10^{-4}$ ratio even in the absence of photo-absorption.

Chevalier & Irwin (2012) calculate that full ionization (which gives minimal photo-absorption) is achieved only for high-velocity shocks with $v \gtrsim 10^4\,{\rm km\,s^{-1}}$. Slower shocks would lead to incomplete ionization (i.e., potentially important photo-absorption), which will further reduce the escaping X-ray flux. Using the explosion observables and Equation (A8) we constrain the total neutral column density between the shock break-out radius and the observer to be $N \approx 2 \times 10^{25}\,{\rm cm^{-2}}$, which gives a bound–free optical depth $\tau_{\rm bf} \approx 2 \times 10^3$ at 1 keV (Equation (A9)). Since $\tau_{\rm bf} \propto R^{-1}$ and $R \propto t$, soft ($E \approx 2$ keV) X-ray emission would not be expected from SN 2009ip until $R \approx 2 \times 10^{16}$ cm, which happens for $\Delta t > 220$ days since the explosion, or >20 break-out timescales $t_{\rm d}$ (where $t_{\rm d} \approx t_{\rm rise}$ in our scenario).[42] This calculation assumes an extended and spherically symmetric wind profile. The Chandra detection of SN 2009ip at much earlier epochs ($\Delta t \approx 4\,t_{\rm d}$) indicates that at least one of these assumptions is invalid, therefore pointing to a truncated and/or highly asymmetric wind profile. This is consistent with the picture of a dense but compact wind shell of radius $R_{\rm w} \approx 1.2 \times 10^{15}$ cm followed by a steep density gradient $\rho_{\rm w} \propto R^{-5.3}$ we developed in Section 7.2. Asymmetry also plays a role, as independently suggested by observations in the optical (Section 7.4).

Finally, Katz et al. (2011) predict that hard-X-ray emission with typical energy of 60 keV is also produced by the collisionless shock. The details of the spectrum are however unclear. Bound–free absorption is less important at these energies giving the chance to detect hard X-rays at earlier times. Our *Swift*-BAT campaign in the 15–150 keV range revealed a tentative detection. With these observations we put a solid upper limit on the hard X-ray- to- optical luminosity around maximum light, which is $L_{\rm X,hard}/L_{\rm bol} < 5 \times 10^{-3}$ at 5σ. The broadband SED around maximum light is shown in Figure 27.

7.6. Radio Emission from Shock Break-out and Continued Interaction

The shock-CSM interaction is a well-known source of radio emission (e.g., Chevalier 1982, 1984). The high density of the wind shell derived from our modeling of Section 7.2 implies a free–free optical depth at radius R, $\tau_{\rm ff} \approx 3.8 \times 10^{54}(\nu/{\rm GHz})^{-2.1}(R/{\rm cm})^{-3}$ (Equation (A10)). With $\tau_{\rm ff} \approx 10^5$–$10^8$ at $R \approx R_{\rm bo}$, no detectable radio emission is expected around break-out, consistent with our lack of radio detection around these times. *If* the dense wind profile extends out to large distances, the calculation above shows that no radio emission is expected until very late times, when the shock reaches $R \approx 7 \times 10^{16}$ cm. Our radio detection at much earlier epochs ($\Delta t \approx 60$–80 days since explosion) demonstrates instead that the dense wind shell is not extended but truncated and adds further, independent evidence for a complex medium where inhomogeneity, asymmetry and/or low wind filling factor might also be relevant. This is consistent with the idea we suggested in Section 7.3 that the dense shell was the outcome of a short eruption, since eruptions are more likely to eject shells as opposed to a steady mass loss.

[42] Svirski et al. (2012) find that, under standard parameters, the X-ray emission is expected to dominate the energy release on timescales of the order of (10–50) $t_{\rm d}$.

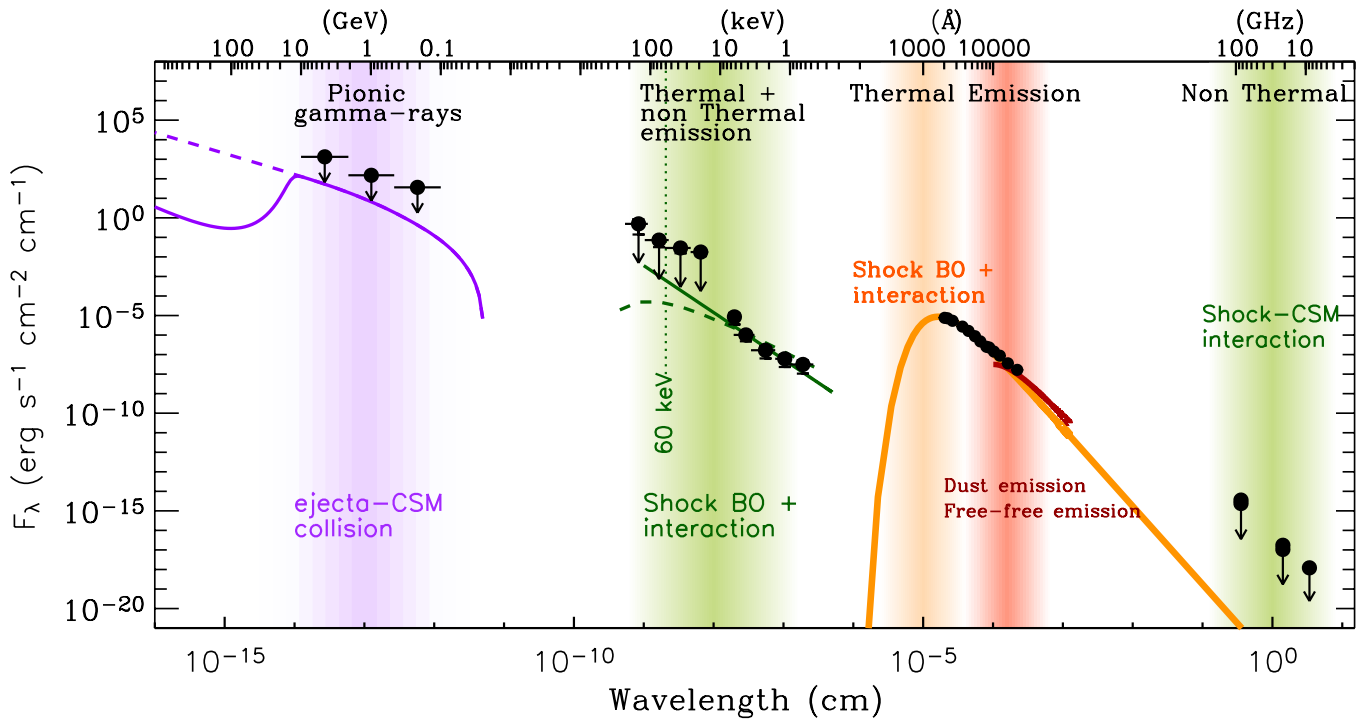

Figure 27. Broadband SED of SN 2009ip around the optical peak. Shaded bands highlight different components that dominate at different wavelengths. Neutral pion decay leads to γ-rays that are powered by the collision between the ejecta and extremely dense CSM shells. We show the limits from *Fermi*-LAT obtained between $t_{\rm pk} - 2$ days and $t_{\rm pk} + 4$ days. Dashed purple line: expected GeV emission based on Section 7.2 assuming no attenuation. The thick-line model includes partial attenuation as relevant for a clumpy and/or asymmetric medium (Section 7.4). Soft and hard X-ray emission originates from the interaction of the shock with the CSM: both thermal and nonthermal emission might arise, mainly depending on the environment density. We show here a power-law (nonthermal emission, thick line with $F_\lambda \propto \lambda^{-2.4}$) and a thermal bremsstrahlung model with $kT = 60$ keV (dashed line) that fit the *Swift*-XRT 0.3–10 keV data obtained between $t_{\rm pk} - 2$ days and $t_{\rm pk} + 4$ days. *Swift*-BAT 15–150 keV data acquired at $t_{\rm pk} \pm 1$ days are also shown. The dotted line marks the energy of 60 keV: this is the typical frequency of high-energy photons emitted by the collisionless shock that forms at shock break-out (Katz et al. 2011). Optical and UV emission is powered by the shock break-out plus continued shock interaction with the environment. Orange line: best-fitting blackbody with $T \approx 17{,}000$ K at $t \approx t_{\rm pk}$. NIR and IR emission could originate from dust (formation, vaporization, or light-echo) or free-free emission. Due to the high temperature ($T \approx 3000$ K, crimson solid line) only dust vaporization or (more likely) free-free emission from an extended outflow can explain our observations. Shock-CSM interaction is also the source of millimeter and radio photons through synchrotron emission. At these times this emission was quenched by free-free absorption by the dense shell of material.

(A color version of this figure is available in the online journal.)

7.7. GeV and Neutrino Emission at Shock Break-out

The collision of the ejecta with massive, dense shells is expected to accelerate cosmic rays (CRs) and generate GeV gamma-rays (Murase et al. 2011; Katz et al. 2011) with fluence that depends both on the explosion and on the environment parameters. The GeV emission is expected to be almost simultaneous with the UV–optical–NIR emission.

The proximity of SN 2009ip ($\approx$24 Mpc) justifies the first search for GeV emission from shock break-out. *Fermi*-LAT observations covering the period $t_{\rm pk} - 30$ days until $t_{\rm pk} + 28$ days yielded no detection (Section 2.7). Following Murase et al. (2011), we predict the GeV emission from SN 2009ip (2012b outburst) using the explosion and environment parameters inferred in Section 7.2 (shell density $\rho_{\rm w}$, corresponding to $n \approx 4 \times 10^{10}$ cm^{-3} at the break-out radius, or mass $M_{\rm w}$) together with the observables of the system ($t_{\rm rise}$, $R_{\rm bo}$). We take into account the attenuation due to $\gamma\gamma \rightarrow e^+e^-$ pair production, assuming a blackbody spectrum with $T = 20{,}000$ K. The attenuation by extragalactic background light is also included. Since n is not too large, the Bethe–Heitler pair production will be irrelevant in our case, as it happens for a clumpy or asymmetric CSM (Section 7.4). The injected CR energy $E_{\rm CR}$ is assumed to be equal to that of the radiation energy at $t_{\rm rise}$. We compare the expected GeV fluence with observations in Figure 27: the *Fermi*-LAT nondetection is consistent with our picture of ejecta crashing into a compact and dense but low-mass ($\lesssim$0.1–0.2 $M_\odot$) shell of material at small radius that we developed in the previous sections. For the detection of γ-rays, brighter SNe (closer SNe or SNe accompanying larger dissipation) are needed.

Using the set of parameters above we predict the muon and antimuon neutrino fluence from SN 2009ip in Figure 28, using the model by Murase et al. (2011). CRs produce mesons through inelastic proton–proton scattering, leading to neutrinos as well as γ-rays. As for the γ-rays, given that the explosion/ environment parameters are constrained by observations at UV/optical/NIR wavelengths, the neutrino fluence directly depends on the total energy in CRs, $E_{\rm CR}$ (or, equivalently on the CR acceleration efficiency $\epsilon_{\rm CR}$, $E_{\rm CR} \equiv \epsilon_{\rm CR} E$, being E the explosion energy). Note that the injected CR energy $E_{\rm CR}$ is assumed to be the radiation energy at $t_{\rm rise}$, but larger values of $E_{\rm CR}$ are possible. The maximum proton energy is also set to 1.5 PeV, corresponding to $\varepsilon_B = 0.01$. Our calculations show that SN 2009ip was a bright source of neutrinos if $E_{\rm CR}$ is comparable to the radiated energy. We note however that its location in the southern sky was not optimal for searches for neutrino emission by IceCube because of the severe atmospheric muon background.

With this study we demonstrate that it is possible to constrain the CR acceleration efficiency if: (1) the explosion/ environment parameters are constrained by observations at UV/optical/NIR wavelengths; (2) deep limits on muon neutrinos are available,

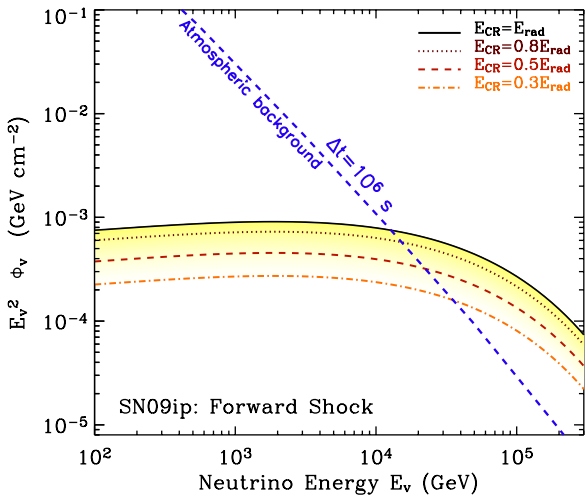

Figure 28. Predicted muon and antimuon neutrino fluence for different values of the total energy in cosmic rays E_{CR}, here parameterized as a function of the radiated energy at t_{rise}. Since $E_k > E_{rad}$, larger values of E_{CR} are also possible. Dashed blue line: atmospheric neutrino background integrated over $\Delta t \approx t_{rise}$ (zenith-angle averaged within 1°). For this event, the atmospheric neutrino background is more severe as SN 2009ip occurred in the southern hemisphere. For better localized explosions, this plot shows how limits on the neutrino emission can be used to constrain E_{CR}.

(A color version of this figure is available in the online journal.)

as will be the case also for southern sky sources once KM3Net will be online in the near future.

7.8. Origin of the NIR Excess

The time-resolved broadband SED analysis of Section 3 identifies the presence of a NIR excess of emission (Figure 13) with respect to a blackbody spectrum. Contemporaneous NIR spectroscopy (Section 2.3) shows that the NIR excess cannot be ascribed to line emission (Figure 7), therefore pointing to a physical process producing NIR continuum emission with luminosity $L \sim 4 \times 10^{41}$ erg s^{-1}. Here we discuss four different physical scenarios: (1) dust formation, (2) light echo from dust, (3) dust vaporization, and (4) radiation from gas in an extended outflow. The last of these seems most likely.

We first adopt a blackbody spectral model to obtain rough estimates of the temperature and location of the dust and constrain the dust-related scenarios. In a more realistic dust emission model, we would need to consider the dust grain properties and composition, leading to a spectrum that is not a true blackbody (e.g., Fox et al. 2011, 2013). This is material for a dedicated article (R. Margutti et al., in preparation). Here we use a simplified approach. From the SED analysis of Section 3 we find that the equivalent NIR blackbody radius is $R_{COLD} \sim 4 \times 10^{15}$ cm with very limited evolution with time (Figure 11). The cold blackbody temperature is also stable, with $T_{COLD} \sim 3000$ K. Considering that our simplified approach overestimates the true dust temperature of hundreds of degrees (up to 20% according to Nozawa et al. 2008) the real dust temperature should be closer to ∼2500 K.

A clear signature of dust formation is the development of highly asymmetric and blue-shifted line profiles (see, e.g., Smith et al. 2008, their Figure 4), which is not observed. The temperature of ∼2500–3000 K is also prohibitively high for dust to form. At this very early epochs the shock radius is also $< R_{COLD}$, implying that the NIR emission cannot originate from dust created behind the reverse shock. The dust creation scenario is therefore highly unlikely, leading to the conclusion that the NIR excess originates from preexisting material ejected by the progenitor before the 2012b explosion. Since the geometry of the NIR emitting material can be non spherical (Section 7.4) and/or have low filling factor (i.e., the material can be clumpy), we do not expect this material to necessarily produce absorption along our line of sight.

Our SED fitting indicates the presence of a NIR excess with similar radius during the 2012a eruption as well (Figure 11), suggesting that the origin of the preexisting material is rather linked to the eruption episodes of the progenitor of SN 2009ip in the years before. The same conclusion was independently reached by Smith et al. (2013). We note that the size of the cool emitting region of SN 2009ip is remarkably similar to the preoutburst dust radii of other optical transients linked to eruption episodes of their progenitor stars like NGC 300 OT2008-1 ($R \sim 5 \times 10^{15}$ cm) and SN 2008S ($R \sim 2 \times 10^{15}$ cm; seem e.g., Berger et al. 2009b, their Figure 28).

A light echo from dust (i.e., preexisting dust heated up by the UV and optical radiation from the explosion) would require the dust grains to survive the harsh environment (see however Smith et al. 2013). At the high temperature of $T \sim 2500$–3000 K this is however unlikely, while dust vaporization is more likely to happen (see, e.g., Draine & Salpeter 1979). We speculate on the dust vaporization scenario below.

In this picture a cavity is excavated by the explosion radiation out to a radius R_c: this radius identifies the position of the vaporized dust, while it does not track the outer dust shell radius (which is instead likely to expand with time; see, e.g., Pearce et al. 1992). Being the dust shell created in the years before the 2012 explosion, we expect the smaller grains to be located at the outer edge of the dust shell as a result of forces acting on them (e.g., radiative pressure). At smaller distances we are likely dominated by the larger dust grains. Following Dwek et al. (1983), their Equation (8) (see also Draine & Salpeter 1979) the radius of the dust-free cavity for a UV–optical source with luminosity L is: $R_c = 23(\langle Q\rangle(L/L_\odot)/(\lambda_0/\mu\mathrm{m})T^5)^{0.5}$, where R_c is in units of pc; T is the temperature at the inner boundary of the dust shell that we identify with the evaporation temperature T_{ev}; $\langle Q\rangle$ is the grain emissivity: $Q = (\lambda_0/\lambda)^n$ for $\lambda \geqslant \lambda_0$ while $Q = 1$ for $\lambda < \lambda_0$. Here we adopt $n = 1$.[43] The dust grain radius is a, with $\lambda_0 \sim 2a$, which implies $R_c \propto a^{-0.5}$. For $R_c = R_{COLD} \sim 4 \times 10^{15}$ cm, $T_{ev} \sim 3000$ K and $L = L_{pk} \sim 1.7 \times 10^{43}$ erg s^{-1}, we constrain the radius of the vaporizing dust grains to be $a \lesssim (2$–$5)\,\mu$m.

Grain radii of 0.2–2 μm are typically found in dust shells, suggesting that we are possibly witnessing the vaporization of the larger grains at $R \sim R_c$. The very high vaporization temperature is only potentially compatible with materials like graphite, silicates, corundum and carbide, which have binding energy $U_0 \gtrsim 6$ eV. Even in these cases $T_{ev} \sim 2500$–3000 K requires extremely short vaporization timescales of the order of ∼1 day or less and *large grains* of the order of 1 μm (Draine & Salpeter 1979, their Equation (24)).

A more natural possibility is that of free–free emission from a power-law distribution of material at large radii (i.e., an extended outflow), ionized by SN 2009ip (Gall et al. 2012). Free–free emission is well known to produce an excess of IR emission in hot stars surrounded by dense winds (see, e.g., Wright & Barlow 1975). Free–free emission has been ruled out by Smith et al. (2013) as potential explanation of the NIR excess of SN 2009ip

[43] A value of n between 1 and 2 is usually assumed. Using $n = 2$ have no impact on our major conclusions. In particular, our estimate of the dust grain radius would be $a \approx 1\,\mu$m.

based on a mismatch between the predicted and observed slope of the continuum. However, the free–free spectral index depends on the density distribution $\rho(R)$ of the emitting material: for $\rho(R) \propto R^{-\beta}$, $F_\lambda \propto \lambda^{-(8\beta-8.2)/(2\beta-1)}$ (Wright & Barlow 1975). The mild spectral index of the NIR excess (see Figure 13) implies a mild density gradient at large radii, with $\beta < 2$ (i.e., significantly flatter than the standard wind profile expected in the case of constant mass-loss rate). This finding suggests a significant increase in the mass-loss rate of the progenitor star during the years preceding the 2012 double outburst.

8. DISCUSSION

Our analysis characterizes the 2012b episode as a low-energy, asymmetric explosion happening in a complex medium, previously shaped by multiple episodes of mass ejection by the progenitor at different times. Here we address three major questions.

1. What is the nature of the SN 2009ip double explosion?
2. What is the underlying physical mechanism?
3. What is the progenitor system of SN 2009ip?

We address these questions by considering the close similarity of SNe 2009ip and 2010mc (Section 8.1), the properties of the progenitor system of SN 2009ip (Section 8.2), the physical mechanisms that can lead to sustained mass loss (Section 8.3), and the energetics of the explosions (Section 8.4).

8.1. SN 2009ip and SN 2010mc

SN 2010mc (Ofek et al. 2013b) is the only other hydrogen-rich explosion with clear signs of interaction and a detected precursor. The similarity with SN 2009ip extends to the energetics, timescales (Figure 29), and spectral properties both during the precursor and the major rebrightening, as noted by Smith et al. (2013).

The first conclusion is that (1) the precursor and the major rebrightening are causally connected events, being otherwise difficult to explain the strict similarity between two distinct and unrelated explosions. The same conclusion is independently supported by the very short time interval between the precursor and main outburst when compared to the progenitor star lifetime, as pointed out by Ofek et al. (2013b) for SN 2010mc. A second conclusion is that (2) whatever causes the precursor plus major outburst phenomenology, this is not unique to SN 2009ip and might represent an important evolutionary channel for massive stars.

Furthermore, (3) SNe 2009ip and 2010mc must share some fundamental properties. Their evolution through the explosive phase must be driven by few physical parameters. A more complicated scenario would require unrealistic fine tuning to reproduce their close similarity. This also suggests we are sampling some fundamental step in the stellar evolution of the progenitor system. Finally, (4) whatever the physical mechanism behind, the time interval of ∼40 days (Figure 29) between the precursor explosion and the main event must be connected to some physically important timescale for the system.

We employ the fast χ^2 technique for irregularly sampled data by Palmer (2009) to search for periodicity and/or dominant timescales in the outburst history of SN 2009ip before[44] the major 2012 explosion. Details can be found in Appendix B. Applying the method above to the R-band data we find evidence

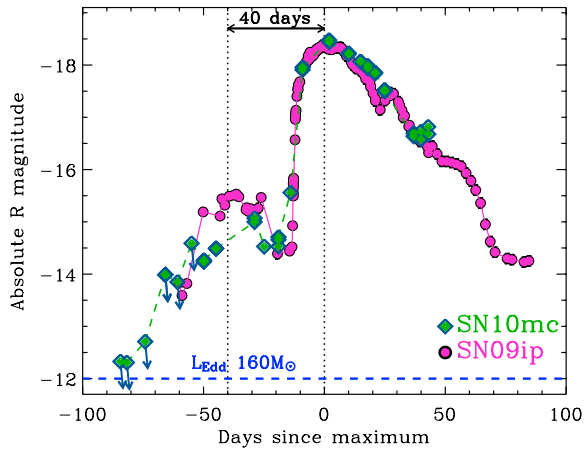

Figure 29. Comparison between SN 2009ip and the Type IIn SN 2010mc (Ofek et al. 2013b) reveals a striking similarity.

(A color version of this figure is available in the online journal.)

for a dominant timescale of ∼38 days, (with significant power distributed on timescales between 30 and 50 days), intriguingly similar to the $\Delta t \sim 40$ days between the precursor and major explosion in 2012. We emphasize that this is *not* a claim for periodicity, but the identification of a dominant variability timescale of the signal.

Our analysis identifies the presence of a fundamental timescale that regulates both the progenitor outburst history and the major explosion, and that is also shared by completely independent events like SN 2010mc. This timescale corresponds to a tiny fraction of a massive star lifetime: $\sim 10^{-8}$ for $\tau \sim 4$–6 Myr, as appropriate for a 45–85 $M_\odot$ star. We speculate on the nature of the underlying physical process in the next two sections.

8.2. The Progenitor System of SN 2009ip

Asymmetry likely plays a role in the 2012 explosion (Section 7.4), which might point to the presence of a preferred direction in the progenitor system of SN 2009ip. This suggests either a (rapidly?) rotating single star or an interacting binary as progenitor for SN 2009ip. We first update previous estimates of the progenitor mass of SN 2009ip using the latest stellar evolutionary tracks and then discuss the effects of stellar rotation and binarity.

From *HST* preexplosion images, employing the latest Geneva stellar evolutionary tracks (Ekström et al. 2012) that include important updates on the initial abundances, reaction rates and mass-loss prescriptions with respect to Schaller et al. (1992), we determine for $M_V = -10.3 \pm 0.3$ (Foley et al. 2011) a zero-age main-sequence (ZAMS) mass $M \gtrsim 60\,M_\odot$ assuming a nonrotating progenitor at solar composition, consistent with previous estimates. $M_V = -10.3$ corresponds to $L_V \sim 10^{6.1}\,L_\odot$. This implies $L_{bol} > 2 \times 10^6\,L_\odot$, thus rivaling the most luminous stars ever discovered (e.g., Crowther et al. 2010). Luminosities of a few $10^6\,L_\odot$ have been indeed associated to the group of LBV stars with typical temperature of ∼15,000–25,000 K. Adopting this range of temperature results in $L_{bol} \sim 5 \times 10^6\,L_\odot$, suggesting that any progenitor with $M < 160\,M_\odot$ was super Eddington at the time of the *HST* observations. For $(2 < L_{bol} < 5) \times 10^6\,L_\odot$ the allowed mass range is $60\,M_\odot < M_{ZAMS} < 300\,M_\odot$ (e.g., Crowther et al. 2010). Including the effects of axial rotation results in a more constrained range of allowed progenitor mass: $45\,M_\odot < M_{ZAMS} < 85\,M_\odot$ (for $\Omega/\Omega_{crit} = 0.4$).

Rapid rotation strongly affects the evolution of massive stars, in particular by increasing the global mass-loss rate (e.g.,

[44] See Martin et al. (2013) for a temporal analysis of SN 2009ip during the main episode of emission in 2012.

Maeder & Meynet 2000). More importantly, Maeder (2002) showed that the mass loss does not remain isotropic, but it is instead enhanced at the polar regions, thus favoring bipolar stellar winds (e.g., Georgy et al. 2011, their Figure 2). As a result, the formation of an asymmetric (peanut shaped) nebula around rapidly rotating stars is very likely. Additionally, rapid rotation can induce mechanical mass loss, resulting in some matter to be launched into an equatorial Keplerian disk. It is clear that any explosion/eruption of the central star will thus naturally occur in a nonisotropic medium, as we find for SN 2009ip. Rotation further leads to enhanced chemical mixing (e.g., Chatzopoulos et al. 2012; Yoon et al. 2012).

HST preexplosion images cannot, however, exclude the presence of a compact companion.[45] The massive progenitor of SN 2009ip might be part of a binary system and the repetitive episodes of eruption might be linked to the presence of an interacting companion. The close periastron passages of a companion star in an eccentric binary system has been invoked by Smith & Frew (2011) to explain the brightening episodes of ηCar in 1838 and 1843. In the context of SN 2009ip, Levesque et al. (2012) discussed the presence of a binary companion, while Soker & Kashi (2013) suggested that the 2012b explosion was the result of a merger of two stars, an extreme case of binary interaction. A binary scenario was also proposed by Soker (2013) for SN 2010mc.

A binary system would have a natural asymmetry (i.e., the preferred direction defined by the orbital plane) and a natural timescale (i.e., the orbital period) as indicated by the observations. A possible configuration suggested to lead to substantial mass loss is that of a binary system made of a compact object (neutron star) closely orbiting around a massive, extended star (Chevalier 2012 and references therein). In this picture the mass loss is driven by the inspiral of the compact object in the common envelope (CE) evolution and the expansion velocity of the material is expected to be comparable to the escape velocity for the massive star. For[46] $v \sim 1000\,\mathrm{km\,s^{-1}}$ and $M \sim 45$–$85\,M_\odot$ the radius of the extended star is $R_* < (1$–$2) \times 10^{12}$ cm (where the inequality accounts for the fact that we used the ZAMS mass). In this scenario, the mass loss is concentrated on the orbital plane of the binary (Ricker & Taam 2012), offering a natural explanation for the observed asymmetry. However, it remains unexplained how this mechanism would be able to launch material with $v \sim 10^4\,\mathrm{km\,s^{-1}}$ as observed during the 2012a episode. A potential solution might be the presence of a high-velocity accretion disk wind.

While the presence of a dominant timescale common to the eruptive and explosive phases makes the binary progenitor explanation particularly appealing, the CE model in its present formulation seems to have difficulties in explaining the observed phenomenology. Alternative scenarios are explored in Section 8.3.

8.3. Physical Mechanisms Leading to Substantial Mass Loss

The outer envelope of an evolved massive star contains ~95% of the stellar radius but only a tiny fraction of the stellar mass. The physical mechanism leading to the 2012a outburst must have been fairly deep seated to unbind more than $\sim 0.1\,M_\odot$. It is furthermore required to generate a large amount of energy (10^{48} erg plus the energy to lift the mass out of the deep gravitational potential well) and to explain the presence of a dominant timescale of ~40 days, which is also shared with the observed eruption history in the years before the explosion. The mass-loss rate of at least a few $\sim 0.1\,M_\odot\,\mathrm{yr}^{-1}$ can only be sustained for an extremely small fraction of the life of a star and in principle only for ~ years, before inducing important adjustments to the stellar structure.

We explore here different physical mechanisms that have been proposed to lead to substantial mass loss in the late stages of evolution of massive single stars and discuss their relevance for SN 2009ip. They can basically be grouped into four categories: (1) pulsational pair instability (PPI), (2) super-Eddington fusion luminosity, (3) Eddington-limit instabilities, and (4) shock heating of the stellar envelope.

PPI (Barkat et al. 1967) applies to massive stars with helium core of ~40–60 $M_\odot$. PPI leads to partial unbinding of the star, with a sequence of eruptions accompanied by the ejection of shells of material of the stellar envelope. This mechanism has been considered as a plausible explanation for SN 2009ip by Pastorello et al. (2013), Mauerhan et al. (2013) and Fraser et al. (2013) but has been rejected by Ofek et al. (2013b) and Ofek et al. (2013a) for SNe 2010mc and 2009ip (the leading argument being that PPI would lead to the ejection of much larger amounts of mass than the $\sim 10^{-1}$–$10^{-2}\,M_\odot$ they infer). According to Woosley et al. (2007), a nonrotating star with zero metallicity ($Z = 0$) and ZAMS mass 95 and 130 $M_\odot$ meets the criteria for PPI. However, with updated prescriptions for the mass-loss rate, and assumption of solar metallicity (which more closely represents our conditions of $0.4\,Z_\odot < Z < 0.9\,Z_\odot$, Section 5) Ekström et al. (2012) predict that even stars with $M = 120\,M_\odot$ will end the C-burning phase with mass $\sim 31\,M_\odot$, below the threshold of $\sim 40\,M_\odot$ to trigger PPI. While our limits on the progenitor mass of SN 2009ip in Section 8.2 do not formally rule out the PPI scenario in the nonrotating case, they definitely allow for progenitors starting with much lower mass than required for the PPI to develop ($M \gtrsim 120\,M_\odot$).

Rapidly rotating progenitors ($\Omega/\Omega_{\mathrm{crit}} > 0.5$) enter the PPI regime starting with substantially lower ZAMS mass: $\sim 50\,M_\odot$ for $Z = 0$ (Chatzopoulos & Wheeler 2012; Yoon et al. 2012). On the other hand, for $Z = Z_\odot$ even very massive rotating $120\,M_\odot$ stars develop a core with $M \sim 19\,M_\odot$, insufficient to trigger PPI (Ekström et al. 2012). In the previous sections we constrained the progenitor of SN 2009ip with ZAMS mass $45\,M_\odot < M < 85\,M_\odot$ and metallicity $0.4\,Z_\odot < Z < 0.9\,Z_\odot$. Following the prescriptions from Chatzopoulos & Wheeler (2012), adopting the most favorable conditions (i.e., $M = 85\,M_\odot$ and $Z = 0.4\,Z_\odot$) and starting with a very rapidly rotating star with $\Omega/\Omega_{\mathrm{crit}} = 0.9$, we find the final oxygen core mass to have $M \sim 35\,M_\odot$, formally below the threshold of $40\,M_\odot$ for PPI. This indicates some difficulties for rotating progenitors to reach the PPI threshold. What remains difficult to interpret both for rotating and nonrotating progenitors is the presence of a dominant timescale of ~40 days: depending on the pulse properties and the physical conditions of the surviving star, the interval between pulses can be anywhere between days to decades (Woosley et al. 2007).

Alternatively, convective motions stimulated by the super-Eddington fusion luminosity in the core of a massive star can excite internal gravity waves (g-mode nonradial oscillations; Quataert & Shiode 2012; Shiode & Quataert 2013). An important fraction of the energy in gravity waves can be converted into sound waves, with the potential to unbind several

[45] The variability argument allows us to conclude that the observed emission is however dominated by the progenitor of SN 2009ip.

[46] This is the velocity required to reach R_{bo} after ~50 days since the 2012a explosion.

$M_\odot$. For a 40 $M_\odot$ star, Quataert & Shiode (2012) estimate that 10^{47}–10^{48} erg will be deposited into the stellar envelope. If this mechanism is responsible for the ejection of material by the 2012a explosion, the velocity $v \sim 1000\,\mathrm{km\,s^{-1}}$ of the unbound material inferred from our observations implies an ejecta mass $\lesssim 0.1\,M_\odot$, consistent with our estimate of the mass of the compact shell encountered by the 2012b explosion in Section 7.2. However, this mechanism is likely to lead to a steady mass loss (E. Quataert 2013, private communication) as opposed to shell ejection and does not offer a natural explanation for the 40-day timescale involved in the process. We therefore consider the super-Eddington luminosity mechanism unlikely to apply to SN 2009ip and SN 2010mc (see, however, Ofek et al. 2013b).

With R-band observed magnitudes between ∼18 mag and ∼21 mag (Pastorello et al. 2013), SN 2009ip oscillates between ∼Eddington and super-Eddington luminosity in the years preceding the double 2012 explosion. Depending on the effective temperature of the emission, $R \sim 21$ mag corresponds to the Eddington luminosity of a star with mass 40–80 $M_\odot$. $R \sim 18$ would correspond to an Eddington limit for a star of $M = 600$–$1200\,M_\odot$. A number of instabilities have been shown to develop in stars approaching and/or exceeding the Eddington limit, allowing the super-Eddington luminosity to persist (e.g., Owocki & Shaviv 2012), potentially powering LBV-like eruptions. The eruption timescale, repetition rate and ejected mass are however loosely predicted, so that it is unclear if any of these mechanisms would apply to the eruption history of SN 2009ip and, even more importantly, how these are connected with the 2012 double explosion (which clearly differs from super-Eddington powered winds). The inferred mass-loss rate of $\dot{M} \sim 0.07\,M_\odot\,\mathrm{yr}^{-1}$ is appreciably higher than the typical mass loss of $\dot{M} \sim 10^{-4}$–$10^{-5}\,M_\odot\,\mathrm{yr}^{-1}$ associated with classical LBVs (Humphreys & Davidson 1994). This finding suggests that the true evolutionary state of the progenitor of SN 2009ip might be different from a classical LBV. With luminosity between $\sim 10^6$ and $\sim 10^7\,L_\odot$, the progenitor of SN 2009ip falls into the region where radiation pressure starts to have a major role in supporting the star against gravity (e.g., Owocki & Shaviv 2012, their Figure 12.1): we speculate that the dominance of radiation pressure over gas pressure in the envelope might have an important role in determining the repeated outbursts of SN 2009ip.

The outer layers of massive stars close to the Eddington limit and/or critical rotation are only loosely bound and might be easily ejected if enough energy is suddenly deposited. A potential source of energy deposition has been identified in thermonuclear flashes associated with shell burning (Dessart et al. 2010). Differently from the PPI, this scenario does not require the progenitor to be extremely massive. Alternatively, nonradial gravity mode oscillations above the core or near to the H-burning shell could provide fresh fuel, triggering a burst of energy (and subsequent shell ejection) in massive stars like ηCar (Guzik 2005). Both scenarios have the advantage to be basically driven by two parameters: the deposited energy and the envelope binding energy, naturally satisfying the "simplicity" criterion of Section 8.1.

Finally we mention that direct numerical simulations of precollapse hydrodynamics by Meakin (2006), Meakin & Arnett (2007) and Arnett & Meakin (2011a, 2011b) found eruptive instabilities due to the interaction of oxygen and silicon burning shells. The instabilities are related to turbulent convection (and being inherently nonlinear, are invisible to conventional linear stability analysis). These simulations specifically predicted mass ejection prior to core collapse, suggesting that precollapse evolution is far more eventful than previously thought. However, as for all the other mechanisms analyzed in this section, it is at the moment unclear how to explain the 40 day timescale.

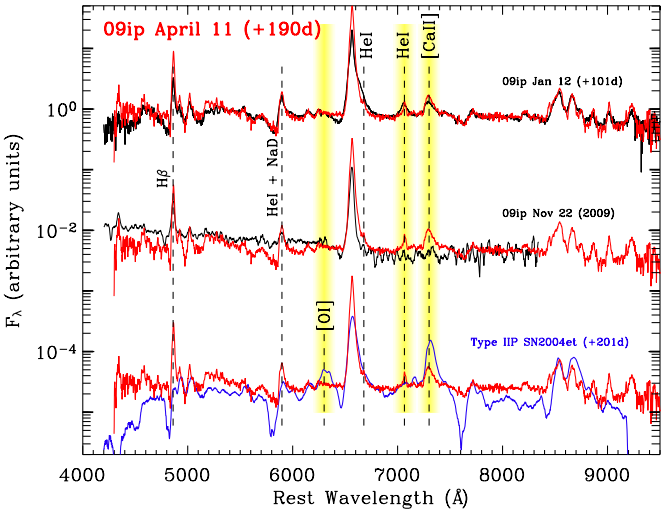

Figure 30. Our spectrum taken in 2013 April ($t_{\rm pk}$ + 190 days) shows minimal evolution with respect to ∼100 days before. The most notable difference with respect to spectra acquired after or during the eruptions is the presence of intermediate He I and [Ca II] in emission. We still do not find evidence for SN-synthesized material (e.g., [O I] 6300 Å). We refer to Sahu et al. (2006) for details on Type IIP SN 2004et.

(A color version of this figure is available in the online journal.)

8.4. The Nature of SN 2009ip Double-Explosion in 2012: The Explosive Ejection of the Stellar Envelope

Our modeling shows that the 2012b explosion is not powered by Ni radioactive decay (Section 7.1) and demonstrates that a shock breaking out from material previously ejected by the 2012a outburst can reasonably account for the observed properties of the 2012b explosion, constraining the mass of the ejecta to $M_{\rm ej} = 50.5(E/10^{51}\ \mathrm{erg})^2\,M_\odot$ (Section 7.2). This strongly suggests an explosion energy below 10^{51} erg (likely around 10^{50} erg), and brings to question the fate of SN 2009ip: a terminal SN explosion (Mauerhan et al. 2013) or a SN "impostor" (Pastorello et al. 2013; Fraser et al. 2013)?

A key prediction of the SN scenario is the presence of chemical elements produced by the SN nucleosynthesis (like oxygen) in late-time spectra, which is not expected in the case of a nonterminal explosion. Our latest spectrum acquired on 2013 April 11 ($t_{\rm pk}$ + 190 days) still shows no evidence for SN-synthesized material (Figure 30). This nondetection is consistent with (but surely not a proof of) the nonterminal explosion scenario. This spectrum, dominated by H emission lines and where the high-velocity absorption features have completely disappeared, shares some similarities with preexplosion spectra of SN 2009ip. A notable difference, however, is the presence of (intermediate width) He I and [Ca II]. The present data set therefore does not yet offer compelling evidence for a standard (i.e., resulting from the collapse of a degenerate core) SN-explosion scenario.

Interaction seems to be still dominating the emission at this time. Our late-time observations indicate a flattening in the light-curve (our latest V-band photometry acquired at $t_{\rm pk}$ + 190 days implies a decay of $\Delta V = +0.86 \pm 0.22$ over 98.5 days,

or 0.0087 ± 0.0022 mag day^{-1}), which might be caused by continued interaction of the shock with the NIR emitting material.

We propose that SN 2009ip was the consequence of the explosive ejection of the envelope of a massive star, which later interacted with material ejected during previous eruption episodes. While $E < 10^{51}$ erg is insufficient to fully unbind a massive star, its outer envelope is only loosely bound, and can be easily ejected by a lower-energy explosion. The origin of the energy deposition is not constrained as unclear is its potential relation with the possible binary nature of the system. The final fate of SN 2009ip depends on the properties of the remaining "core," and in particular, on its mass and rotation rate: if the star managed to explode its entire H envelope still retaining a super-critical core mass, it might reexplode in the future as a genuine H-poor (Ib/c) SN explosion; if instead the star partially retained its envelope, it will possibly give rise to other SN-impostor displays, on timescales that are difficult to predict. The core might also have directly collapsed to a black hole: in this case this would mark the "end." Only close inspection of the explosion site after SN 2009ip has appreciably faded will reveal if the star survived the ejection of its outer layers. Given the impressive similarity with SN 2010mc, our interpretation extends to this event as well.

9. SUMMARY AND CONCLUSIONS

The 2012 double explosion of SN 2009ip brought to light the limits of our current understanding of massive star evolution, pointing to the existence of new channels for sustained mass loss in evolved stars, whose origins have still to be identified. Our results indicate that the progenitor of SN 2009ip was in an evolutionary state that is likely to be distinct from the classical LBV state (Humphreys & Davidson 1994). Our extensive follow-up campaign and modeling allow us to identify the properties of a complex ejecta structure and an explosion environment shaped by repeating outbursts during the previous years. Our finding are as follows.

1. SN 2009ip is embedded in a subsolar metallicity environment ($0.4\,Z_\odot < Z < 0.9\,Z_\odot$) in the outskirts of its host galaxy ($d \sim 5$ kpc); it radiated $\sim 3 \times 10^{49}$ erg (2012b explosion) and reached a peak luminosity of $\sim 2 \times 10^{43}$ erg s^{-1}. The precursor released $\sim 2 \times 10^{48}$ erg.
2. The explosion is not powered by ^{56}Ni radioactive decay. From late-time photometry, the total ^{56}Ni mass is $M_{\rm Ni} < 0.08\,M_\odot$. Narrow emission lines in the optical spectra require interaction of the explosion shock with the CSM. We suggest that this interaction is also responsible for mediating the conversion of the shock kinetic energy into radiation, powering the observed light-curve.
3. Spectroscopy at optical to NIR wavelengths identifies three distinct velocity components in the ejecta with $v \sim 12{,}000$ km s^{-1}, $v \sim 5500$ km s^{-1}, and $v \sim 2500$ km s^{-1}, arguing against a continuous velocity distribution. No departure from spherical symmetry needs to be invoked for the slow-moving ($v \leqslant 5500$ km s^{-1}) ejecta. Instead, spherical symmetry is clearly broken by the high-velocity material, possibly pointing to the presence of a preferred direction in the explosion. Broad and intermediate components in the optical/NIR spectra are consistent with the view that asymmetry might also have a role in the spatial distribution of the interacting material.
4. CSM material in the region surrounding SN 2009ip, with velocity of a few to several 100 km s^{-1}, originates from abrupt episode(s) of mass ejection in the previous years. Mass loss is unlikely to have occurred in the form of a steady wind; instead, our analysis favors explosive mass ejections, likely linked to instabilities developing deep inside the stellar core.
5. We interpret the major 2012 rebrightening to be caused by the explosion shock breaking out through dense material ejected by the precursor. Our analysis constrains the onset of the explosion to be $\sim$20 days before peak. The break-out radius is $R_{\rm bo} \sim 5 \times 10^{14}$ cm. The shell extends to $R_{\rm w} \sim 1.2 \times 10^{15}$ cm, with a total mass of $M_{\rm w} \sim 0.1\,M_\odot$. The presence of a compact and dense shell is independently supported by (1) the detection of X-ray radiation with $L_{\rm X}/L_{\rm opt} < 10^{-4}$ and (2) by the late-time rise of radio emission. After break-out the optical-UV light-curve is powered by continued interaction with optically thin material characterized by a steep density profile.
6. A shock breaking out through dense material is expected to produce hard X-rays with a typical energy of 60 keV. We report a tentative detection of hard X-rays (15–150 keV range) around the optical peak and put a solid upper limit on the hard X-ray-to-optical emission from SN 2009ip: $L_{\rm X,hard}/L_{\rm bol} < 5 \times 10^{-3}$.
7. The collision of the ejecta with a massive shell(s) is expected to accelerate CRs and generate GeV gamma-rays. Using *Fermi*-LAT data we detect no GeV radiation, consistent with the picture of ejecta crashing into a compact and dense but low-mass shell of material at a small radius.
8. Our calculations indicate that the latest outburst from SN 2009ip was a bright source of neutrinos if the CR energy is comparable to the radiated energy. We demonstrate with SN 2009ip how to constrain the CR acceleration efficiency using broadband electromagnetic data and deep limits on muon neutrinos that will be available in the near future.
9. The NIR excess of emission originate from material at large radii, the origin of which has to be connected with mass-loss episodes in the previous years. Free–free emission is the most likely physical process. Dust vaporization cannot be excluded, but would require extreme parameters.
10. Finally, our modeling of the 2012b explosion implies a small ejecta mass of $M_{\rm ej} \sim 0.5\,M_\odot$, with an explosion energy below 10^{51} erg (likely around 10^{50} erg), thus raising questions about the nature of SN 2009ip: Was it a terminal SN explosion or a SN impostor?

This analysis constrains the 2012b rebrightening of SN 2009ip to be a low-energy, asymmetric explosion in a complex medium. We interpret this 2012b episode to be the explosive ejection of the envelope of the massive progenitor star that later interacted with material ejected during previous eruption episodes.

To unravel the nature of the physical mechanism behind the complex phenomenology of SN 2009ip, two key observational findings stand out: (1) its extreme similarity with SN 2010mc both in terms of timescales and energetics of the precursor bump and the main explosion; (2) the presence of a dominant timescale of $\sim$40 days, which regulates both the progenitor outburst history and major explosion (and which is also shared by completely independent events like SN 2010mc).

While it is clear that the physical process leading to the 2012a eruption must have been fairly deep seated to unbind $\sim 0.1\ M_\odot$, it is unclear if any of the proposed mechanisms for substantial episodic mass loss (i.e., PPI, super-Eddington fusion luminosity, Eddington-limit instabilities, and shock heating of the stellar envelope) would be able to fully account for the observed properties and, in particular, for the presence of dominant timescales. Indeed, the presence of dominant timescales might suggest a binary progenitor.

The mechanism behind the precursor plus major outburst is not unique to SN 2009ip (see, e.g., SN 2010mc); it is likely driven by few physical parameters and likely represents an important evolutionary channel for massive stars. Future observations will reveal if SN 2009ip was able to survive.

We are grateful to the referee, K. Davidson, for many insightful comments and suggestions that helped improve and clarify our manuscript. We are indebted to E. Dwek, E. Quataert, H. Krimm, S. Barthelmy, I. Czekala, and G. Chincarini for many interesting discussions and helpful suggestions. R. M. thanks O. Fox and E. Ofek for sending their comments on the first version of the article posted online. We would also like to thank the entire *Swift* team for their hard work and excellent support in scheduling the observations.

C.C.C. was supported at NRL by a Karles' Fellowship and NASA DPR S-15633-Y. J.V. and T.S. are supported by the Hungarian OTKA Grant NN 107637. C.G. is supported by the NASA Postdoctoral Program (NPP). M.I. and C.C. were supported by the Creative Research Initiative program of the Korea Research Foundation (KRF) grant No. 2010-000712. R.C. acknowledges support from the National Science Foundation under grant AST-0807727. M.S. gratefully acknowledges generous support provided by the Danish Agency for Science and Technology and Innovation realized through a Sapere Aude Level 2 grant. R.K. acknowledges support from the National Science Foundation under grant AST-1211196. The Dark Cosmology Centre is funded by the Danish National Science Foundation. The research of J.C.W., the Texas Supernova Group and E.C. is supported in part by NSF AST-1109801 and by StScI grant HST-AR-12820. E.C. wishes to thank the University of Texas Graduate School for the William C. Powers fellowship given in support of his studies. The work of the Carnegie Supernova Project is supported by the National Science Foundation under grant AST1008343. This work is based on observations made with ESO Telescopes at the La Silla Paranal Observatory under program ID 090.D-0719. Observations reported here were obtained at the MMT Observatory, a joint facility of the Smithsonian Institution and the University of Arizona. This article includes data gathered with the 6.5 m Magellan telescopes located at Las Campanas Observatory, Chile. Observations were obtained with the JVLA operated by the National Radio Astronomy Observatory, program12B-068. The National Radio Astronomy Observatory is a facility of the National Science Foundation operated under cooperative agreement by Associated Universities, Inc. Support for CARMA construction was derived from the Gordon and Betty Moore Foundation, the Kenneth T. and Eileen L. Norris Foundation, the James S. McDonnell Foundation, the Associates of the California Institute of Technology, the University of Chicago, the states of California, Illinois, and Maryland, and the National Science Foundation. Ongoing CARMA development and operations are supported by the National Science Foundation under a cooperative agreement and by the CARMA partner universities. The *Fermi*-LAT Collaboration acknowledges generous ongoing support from a number of agencies and institutes that have supported both the development and the operation of the LAT as well as scientific data analysis. These include the National Aeronautics and Space Administration and the Department of Energy in the United States, the Commissariat à l'Energie Atomique and the Centre National de la Recherche Scientifique/Institut National de Physique Nucléaire et de Physique des Particules in France, the Agenzia Spaziale Italiana and the Istituto Nazionale di Fisica Nucleare in Italy, the Ministry of Education, Culture, Sports, Science and Technology (MEXT), High Energy Accelerator Research Organization (KEK), and Japan Aerospace Exploration Agency (JAXA) in Japan, and the K. A. Wallenberg Foundation, the Swedish Research Council, and the Swedish National Space Board in Sweden. Additional support for science analysis during the operations phase is gratefully acknowledged from the Istituto Nazionale di Astrofisica in Italy and the Centre National d'Études Spatiales in France. This paper made use of the SUSPECT database (http://www.nhn.ou.edu/suspect/).

APPENDIX A

EQUATIONS

We solve here Equations (1), (3), and (5) from Chevalier & Irwin (2011) for the three observables: break-out radius $R_{\rm bo}$, total radiated energy $E_{\rm rad}$, and light-curve rise time $t_{\rm rise}$. In the equations below $M_{\rm ej}$ is the ejecta mass; E is the explosion energy; $\rho_{\rm w}$ is the environment density, parameterized as $\rho_{\rm w} = \dot{M}/(4\pi r^2 v_{\rm w})$, or $\rho_{\rm w} = Dr^{-2}$ with $D \equiv 5.0 \times 10^{16}({\rm g\ cm^{-1}})D_*$ and r is in cgs units; and $\dot{M}$ is the progenitor mass-loss rate. We consider here their model (a) (see their Figure 1), where the break-out happens inside the dense wind shell of radius $R_{\rm w}$ so that $R_{\rm bo} < R_{\rm w}$. For SN 2009ip it turns out that $R_{\rm bo} \lesssim R_{\rm w}$, which leads to comparable estimates of the explosion and the environment parameters even if one were to use their model (b). The system of equation is degenerate for $M_{\rm ej}/E^2$. We obtain the following:

$$M_{\rm ej} = 10\left(\frac{R_{\rm bo}}{4.0 \times 10^{14}\ {\rm cm}}\right)^{-2}\left(\frac{E_{\rm rad}}{0.44 \times 10^{50}\ {\rm erg}}\right)^{-1} \times \left(\frac{t_{\rm rise}}{6.6\ {\rm days}}\right)^{2}\left(\frac{E}{10^{51}\ {\rm erg}}\right)^{2} M_\odot \quad \text{(A1)}$$

$$D_* = \left(\frac{t_{\rm rise}}{6.6\ {\rm days}}\right)^{2}\left(\frac{R_{\rm bo}}{4.0 \times 10^{14}\ {\rm cm}}\right)^{-3}\left(\frac{E_{\rm rad}}{0.44 \times 10^{50}\ {\rm erg}}\right) \quad \text{(A2)}$$

$$\dot{M} = D_*\left(\frac{v_{\rm w}}{1000\ {\rm km\ s^{-1}}}\right) M_\odot\ {\rm yr^{-1}} \quad \text{(A3)}$$

$$k = 0.34\left(\frac{R_{\rm bo}}{4.0 \times 10^{14}\ {\rm cm}}\right)^{3}\left(\frac{E_{\rm rad}}{0.44 \times 10^{50}\ {\rm erg}}\right)^{-1} \times \left(\frac{t_{\rm rise}}{6.6\ {\rm days}}\right)^{-1}\ {\rm cm^2\ g^{-1}}, \quad \text{(A4)}$$

where $v_{\rm w}$ is the wind velocity and k is the opacity. The mass enclosed within a radius R is

$$M_{\rm w}(r < R) = 6.3 \times 10^{17}\left(\frac{R}{\rm cm}\right)\left(\frac{t_{\rm rise}}{6.6\ {\rm days}}\right)^{2} \times \left(\frac{R_{\rm bo}}{4.0 \times 10^{14}\ {\rm cm}}\right)^{-3}\left(\frac{E_{\rm rad}}{0.44 \times 10^{50}\ {\rm erg}}\right){\rm g}. \quad \text{(A5)}$$

The luminosity from continued shock-wind interaction (Chevalier & Irwin 2011, their Equation (9)) after break-out can be written as

$$L(t) = 7.1 \times 10^{43} \left(\frac{E_{\rm rad}}{0.44 \times 10^{50}\ {\rm erg}}\right) \times \left(\frac{t_{\rm rise}}{6.6\ {\rm days}}\right)^{-0.4} \left(\frac{t}{10\ {\rm days}}\right)^{-0.6} {\rm erg\ s^{-1}}. \quad (A6)$$

The radius of the wind shell is

$$R_{\rm w} = 8.3 \times 10^{13} \left(\frac{t_{\rm rise}}{6.6\ {\rm days}}\right)^{-0.8} \left(\frac{R_{\rm bo}}{4.0 \times 10^{14}\ {\rm cm}}\right) \left(\frac{t_{\rm w}}{\rm days}\right) {\rm cm}, \quad (A7)$$

where $t_{\rm w}$ is the time when the shock reaches the edge of the shell. In this scenario, the onset of the explosion is at $t_0 \approx t_{\rm peak} - 2t_{\rm rise}$.

Assuming hydrogen-rich material with $\langle \mu_{\rm p} \rangle = 1$, the column density from radius R to the observer can be written as (see Ofek et al. 2013a)

$$N(R) \approx 3.02 \times 10^{25} \left(\frac{t_{\rm rise}}{6.6\ {\rm days}}\right)^{2} \left(\frac{R_{\rm bo}}{4.0 \times 10^{14}\ {\rm cm}}\right)^{-3} \times \left(\frac{E_{\rm rad}}{0.44 \times 10^{50}\ {\rm erg}}\right) \left(\frac{R}{10^{15}\ {\rm cm}}\right)^{-1} {\rm cm^{-2}}. \quad (A8)$$

The bound–free optical depth at radius R as a function of the energy of the photons, E is $\tau_{\rm bf} = N\sigma(E)$ or

$$\tau_{\rm bf}(E) \approx 3 \times 10^{3} \left(\frac{t_{\rm rise}}{6.6\ {\rm days}}\right)^{2} \left(\frac{R_{\rm bo}}{4.0 \times 10^{14}\ {\rm cm}}\right)^{-3} \times \left(\frac{E_{\rm rad}}{0.44 \times 10^{50}\ {\rm erg}}\right) \left(\frac{R}{10^{15}\ {\rm cm}}\right)^{-1} \left(\frac{E}{\rm keV}\right)^{-2.5} \quad (A9)$$

adopting the approximated cross section as in Ofek et al. (2013a), which is valid in the X-ray energy range only. The free–free optical depth $\tau_{\rm ff}$ at radius R as a function of photon frequency ν is

$$\tau_{\rm ff}(\nu) \approx 2.6 \times 10^{8} \left(\frac{T_e}{10^{4}\ {\rm K}}\right)^{-1.35} \left(\frac{\nu}{\rm GHz}\right)^{-2.1} \left(\frac{R}{10^{15}\ {\rm cm}}\right)^{-3} \times \left(\frac{t_{\rm rise}}{6.6\ {\rm days}}\right)^{4} \left(\frac{R_{\rm bo}}{4.0 \times 10^{14}\ {\rm cm}}\right)^{-6} \left(\frac{E_{\rm rad}}{0.44 \times 10^{50}\ {\rm erg}}\right)^{2}, \quad (A10)$$

where T_e is the electron temperature.

APPENDIX B

TEMPORAL ANALYSIS

We identify the presence of a dominant timescale of ∼40 days by applying the Fast χ^2 algorithm[47] developed by Palmer (2009) to the R-band photometry obtained for SN 2009ip by Pastorello et al. (2013) in the period 2009 August–2012 April. This algorithm is suitable for irregularly sampled data with nonuniform errors, and it is designed to identify the presence of periodic signals by minimizing the χ^2 between the data and the model. We adopt a linear model for the trend. The best period was found to be $T_0 = 115$ days. However, the reduction in the χ^2 obtained for this period is comparable over a broad range of period candidates, thus proving that there it is no periodic or quasi-periodic signal. Assuming the Fourier decomposition with the fundamental period T_0, among the first seven harmonics most (52%) of the temporal power is carried by the third harmonic ($T_0/3 = 38$ days), followed by the fundamental (19%), the fifth harmonic ($T_0/5 = 23$ days, 10%), and the second and fourth harmonics ($T_0/2 = 58$ and $T_0/4 = 29$ days, 5% each). This is evidence for a dominant timescale of about 40 days, with significant power distributed on timescales between 30 and 50 days. Replicating the same analysis on the time series obtained by randomizing the observed magnitudes has the effect of washing out the excess of power on those timescales. This demonstrates that the excess of power around 40 days is not due to the data sampling.

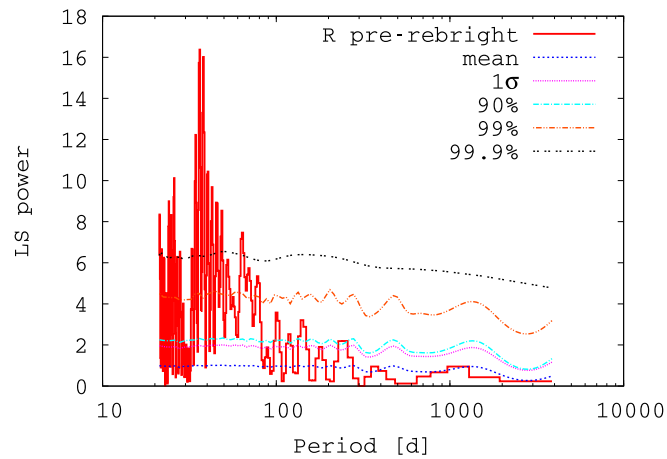

Figure 31. Lomb–Scargle periodogram of the R-band magnitude time series for the time interval 2009 August–2012 April (i.e., before the 2012a and 2012b explosions). This plot shows significant power on timescales around ∼40 days. We emphasize that this is not a claim for periodicity. Contours at various significance levels are also shown.

(A color version of this figure is available in the online journal.)

Additionally and independently, we calculated the Lomb–Scargle (LS; Lomb 1976; Scargle 1982) periodogram of the same time series. This is particularly suitable to unevenly sampled data sets and measures the power contributed by the different frequencies to the total variance. This reduces to the Fourier power spectrum in the uniform sampling limit. As shown in Figure 31, most power is concentrated between ∼30 and ∼50 days, with a peak around 40 days. To evaluate the impact of the aliasing and to quantify how significant the power is with respect to the white noise case (i.e., no preferred timescale), we carried out the following Monte Carlo simulation. We randomized the magnitudes among the same observation times and generated 10^4 synthetic profiles with the same variance as the real one. For each period we derived the corresponding confidence levels of 1σ, 90%, 99%, and 99.9%, as shown in Figure 31. Comparing the real LS periodogram with the MC generated confidence levels, we conclude that power in excess of white noise around 40 days is significant at 99.9% confidence, and we identify this timescale as the dominant one in the overall variance.

In addition, we applied both methods to the time profiles obtained for the V, H, and R filters around the 2012 outburst. We applied both a third and a fourth degree polynomial detrending. In all cases, we obtained similar results with dominant timescales in the range 30–50 days. This is a robust result which does not crucially depend on the polynomial degree used for detrending the series.

[47] http://public.lanl.gov/palmer/fastchi.html

APPENDIX C

DATA REDUCTION

C.1. Swift-UVOT Photometry and Spectroscopy

Swift-UVOT photometry in the six filters has been analyzed following the prescriptions by Brown et al. (2009). We used different apertures during the fading of the 2012a outburst to maximize the signal-to-noise ratio and limit the contamination by a nearby star. For the 2012a event we used a 3″ aperture for the b and v filters, 4″ for the u filter, and 5″ for the UV filters. We correct for point spread function (PSF) losses following standard prescriptions. At peak SN 2009ip reaches $u \sim 12.5$ mag potentially at risk for major coincidence losses. For this reason we requested a smaller readout region around maximum light. Our final photometry is reported in Table 4 and shown in Figure 2. The photometry is based on the UVOT photometric system (Poole et al. 2008) and the revised zero points of Breeveld et al. (2011).

Starting on 2012 September 27 ($t_{\rm pk} - 6$ days), a series of spectra were taken with the *Swift*-UVOT UV grism, with a cadence of one to two days, until 2012 October 28 ($t_{\rm pk}$+25 days), with a final long observation on 2012 November 2 ($t_{\rm pk}$+30 days). The spectra were extracted from the image using the UVOTPY package. The wavelength anchor and flux calibration were the recent updates valid for locations other than the default position in the center (P. Kuin et al., in preparation; details can be found online[48]). The spectra were extracted for a slit with the default 2.5σ aperture and a 1σ aperture, applying an aperture correction when needed. The wavelength accuracy is 20 Å (1σ), the flux accuracy (systematic) is within 10%, while the resolution is $R \sim 75$–110 depending on the wavelength range. The error in the flux was computed from the Poisson noise in the data, as well as from the consistency of between the spectra extracted from the images on one day. The sequence of *Swift*-UVOT spectra is shown in Figure 3. The observing log can be found in Table 1.

C.2. HST Spectroscopy

Observations with the Space Telescope Imaging Spectrograph (STIS) were taken on 2012 October 29 ($t_{\rm pk}$ + 26 days) using aperture 52x0.2E1 with gratings G230LB, G430L, and G750L with exposures times of 1200 s, 400 s, and 100 s, respectively. The STIS two-dimensional images were cleaned of cosmic rays and dead pixel signatures before extraction. The extracted spectra were then matched in flux to the STSDAS/STIS pipeline one-dimensional data product. The spectrum is shown in Figure 4. Further *HST*-COS data were acquired on 2012 November 6 ($t_{\rm pk}$+34 days, Figure 4, lower panel). Observations with the Cosmic Origin Spectrograph (COS) were acquired using MIRROR A + bright object aperture for 250 s. The COS data were then reprocessed with the COS calibration pipeline, CALCOS v2.13.6, and combined with the custom IDL coaddition procedure described by Danforth et al. (2010) and Shull et al. (2010). The total exposure time for the far-UV observation was 3100 s and 3700 s for near-UV.

C.3. Optical Photometry and Spectroscopy

Observations in the v, b, and u filters were obtained with *Swift*-UVOT and reduced as explained above. In Figure 2 we apply a dynamical color term correction to the UVOT v, b, and u filters to plot the equivalent Johnson magnitudes following the prescriptions by Poole et al. (2008). This is a minor correction to the measured magnitudes, and it is not responsible for the observed light-curve bumps. R- and I-band photometry was obtained with the UIS Barber Observatory 20 inch telescope (Pleasant Plains, IL), operated by Josch Hambasch at the Remote Observatory Atacama Desert, a Celestron C9.25 operated by TG Tan (Perth, Australia), and a C11 Schmidt-Cassegrain telescope operated by Ivan Curtis (Adelaide, Australia). Exposure times ranged from 120 s to 600 s. Images were reduced following standard procedure. The photometry was corrected to the photometric system of Pastorello et al. (2013) using the corrections of $dR = +0.046$ and $dI = +0.023$ (A. Pastorello 2012, private communication). R- and I-band photometry is reported in Table 5. A single, late-time ($t_{\rm pk}$ + 190 days) V-band observation was obtained with the Inamori-Magellan Areal Camera and Spectrograph (IMACS; Dressler et al. 2006) mounted on the Magellan/Baade 6.5 m telescope on 2013 April 11.40 (exposure time of 90 s). Data were reduced using standard tasks in IRAF[49] and calibrated to a standard star field at similar airmass.

SN 2009ip was observed with the MagE (Magellan Echellette) Spectrograph mounted on the 6.5 m Magellan/Clay telescope at Las Campanas Observatory. Data reduction was performed using a combination of Jack Baldwin's `mtools` package and IRAF echelle tasks, as described in Massey et al. (2012). Optical spectra were obtained at the F. L. Whipple Observatory 1.5 m Tillinghast telescope on several epochs using the FAST spectrograph (Fabricant et al. 1998). Data were reduced using a combination of standard IRAF and custom IDL procedures (Matheson et al. 2005). Low- and medium-resolution spectroscopy was obtained with the Robert Stobie Spectrograph mounted on the Southern African Large Telescope (SALT/RSS) at the South African Astronomical Observatory in Sutherland, South Africa. Additional spectroscopy was acquired with the Goodman High Throughput Spectrograph (GHTS) on the SOAR telescope. We also used IMACS mounted on the Magellan telescope and the Low Dispersion Survey Spectrograph 3 (LDSS3) on the Clay telescope (Magellan II). The Multiple Mirror Telescope (MMT) equipped with the "Blue Channel" spectrograph (Schmidt et al. 1989) was used to monitor the spectral evolution of SN 2009ip over several epochs. Further optical spectroscopy was obtained with the R-C CCD Spectrograph (RCSpec) mounted on the Mayall 4.0 m telescope, a Kitt Peak National Observatory (KPNO) facility. Spectra were extracted and calibrated following standard procedures using IRAF routines. We used the X-shooter echelle spectrograph (D'Odorico et al. 2006) mounted at the Cassegrain focus of the *Kueyen* unit of the Very Large Telescope (VLT) at the European Southern Observatory (ESO) on Cerro Paranal (Chile) to obtain broadband, high-resolution spectroscopy of SN 2009ip on 2012 September 30 ($t_{\rm pk} - 3$ days) and October 31 ($t_{\rm pk}$ + 28 days). The spectra were simultaneously observed in three different arms, covering the wavelength range 3000–25000 Å. We used the X-shooter pipeline (Modigliani et al. 2010) and custom IDL programs to reduce and flux calibrate the data. The spectra were also slit-loss corrected and corrected for heliocentric velocities. The spectra were not (carefully) telluric corrected. The sequence of optical spectra is shown in Figure 6. The observing log can be found in Table 2.

[48] http://www.mssl.ucl.ac.uk/~npmk/Grism

[49] IRAF is distributed by the National Optical Astronomy Observatories, which are operated by the Association of Universities for Research in Astronomy, Inc., under cooperative agreement with the National Science Foundation.

C.4. NIR Photometry and Spectroscopy

UKIRT observations in the *ZYJHK* filters started on 2012 September 23 ($t_{pk} - 10$ days) and continued on a nearly daily basis until 2012 December 31 ($t_{pk} + 89$ days), when SN 2009ip settled behind the Sun. The flux of the object was measured with AUTO-MAG of SExtractor (Bertin & Arnouts 1996), where the photometric calibration was done using Two Micron All Sky Survey (2MASS) stars within a radius of 8 arcmin from SN 2009ip. The 2MASS magnitudes of the stars were converted to the UKIRT system following Hodgkin et al. (2009). Additional NIR photometry was obtained with PAIRITEL, the $f/13.5$ 1.3 m Peters Automated Infrared Imaging TELescope at the Fred Lawrence Whipple Observatory (FLWO) on Mount Hopkins, Arizona (Bloom et al. 2006). PAIRITEL data were processed following Wood-Vasey et al. (2008) and Friedman (2012). Aperture photometry with a 3″ aperture was performed at the position of SN 2009ip. Figure 2 presents the complete SN 2009ip NIR data set. The PAIRITEL photometry can be found in Table 6. A table will the UKIRT photometry will be published in M. Im et al. (in preparation).

In addition to the X-shooter spectra above, low-dispersion ($R \approx 700$) NIR spectra were obtained with the 2.4 m Hiltner telescope at MDM Observatory on 2012 September 27 ($t_{pk} - 6$ days) and September 29 ($t_{pk} - 4$ days). The data were collected using TIFKAM. Data reduction followed standard procedures within IRAF. The spectra were corrected for telluric absorption and stellar features. Additional NIR low-resolution spectroscopy of SN 2009ip was obtained with the Folded-Port Infrared Echellette (FIRE) spectrograph (Simcoe et al. 2013) on the 6.5 m Magellan Baade Telescope on 2012 November 5, 25 and December 3. Data were reduced following Vacca et al. (2003), Foley et al. (2012) and Hsiao et al. (2013). Moderate-resolution ($R \sim 6000$) NIR spectroscopy was obtained on 2012 November 19 with FIRE in high-resolution echellette mode. Data were reduced using a custom-developed IDL pipeline (FIREHOSE), evolved from the MASE suite used for optical echelle reduction (Bochanski et al. 2009). Standard procedures were followed to apply telluric corrections and relative flux calibrations as described above. The complete sequence of NIR spectra is shown in Figure 7. The observing log can be found in Table 3.

C.5. Millimeter and Radio Observations

We obtained two sets of millimeter observations at mean frequency of ∼84.5 GHz (∼7.5 GHz bandwidth) with the Combined Array for Research in Millimeter Astronomy (CARMA; Bock et al. 2006) around maximum light, beginning on 2012 September 27.17 ($t_{pk} - 6$ days) and 2012 October 17.12 ($t_{pk} + 14$ days). We utilized 2158−150 and 2258−279 for gain calibration, 2232+117 for bandpass calibration, and Neptune for flux calibration. In ∼160 and ∼120 minute integration time at the position of SN 2009ip, we obtain 3σ upper limits on the flux density of 1.5 and 1.0 mJy, respectively. The overall flux uncertainty with CARMA is ∼20%. We observed the position of SN 2009ip with the Karl G. Jansky Very Large Array (VLA; Perley et al. 2011) on multiple epochs beginning on 2012 September 26.10 ($t_{pk} - 7$ days), with the last epoch beginning on 2012 December 2.93 ($t_{pk} + 61$ days). These observations were carried out at 21.25 GHz and 8.85 GHz with 2 GHz bandwidth in the VLA's most extended configuration (A; maximum baseline length ∼36.4 km) except for the first observations, which were obtained in the BnA configuration. In most epochs our observations of flux calibrator, 3C48, were too contaminated with radio frequency interference (RFI). Therefore, upon determining the flux of our gain calibrator J2213−2529 from the best observations of 3C48, we set the flux density of J2213−2529 in every epoch to be 0.65 and 0.63 Jy for 21.25 and 8.9 GHz, respectively. We note that this assumption might lead to slightly larger absolute flux uncertainties than usual (∼15%–20%). In addition, the source-phase calibrator cycle time (∼6 minutes) was a bit longer than standard for high frequency observations in an extended configuration, potentially increasing decoherence. We manually inspected the data and flagged edge channels and RFI, effectively reducing the bandwidth by ∼15%. We reduced all data using standard procedures in the Astronomical Image Processing System (Greisen 2003). A summary of the observations is presented in Table 7.

C.6. X-Ray Observations

Swift-XRT data have been entirely acquired in photon counting mode and analyzed using the latest HEASOFT (v6.12) release, with standard filtering and screening criteria. For $t < -11$ days no X-ray source is detected at the position of SN 2009ip down to a 3σ limit of 3×10^{-3} cps in the 0.3–10 keV energy band (total exposure of 12.2 ks). In the time interval -11 days $< t - t_{pk} < -2$ days the 0.3–10 keV count-rate limit at the SN position is $<1.1 \times 10^{-3}$ cps (exposure time of 31.4 ks). Correcting for PSF losses and vignetting and merging the two time intervals we find no evidence for X-ray emission originating from SN 2009ip in the time interval -29 days $< t - t_{pk} < -2$ days down to a limit of $<5.6 \times 10^{-4}$ cps (0.3–10 keV, exposure time of 43.6 ks). An X-ray source is detected at the level of 5σ and 4σ in the time intervals -2 days $< t - t_{pk} < +3$ days and +4 days $< t - t_{pk} < +13$ days, respectively, with PSF and vignetting corrected count-rates of $(1.6 \pm 0.3) \times 10^{-3}$ cps and $(6.8 \pm 1.8) \times 10^{-4}$ cps (0.3–10 keV, exposure time of 42 and 44 ks).

We carried out *XMM-Newton* observations starting from 2012 November 3 ($t_{pk} + 31$ days). Observations have been obtained with the EPIC-PN and EPIC-MOS cameras in full frame with a thin filter mode. The total exposures for the EPIC-MOS1 and EPIC-MOS2 are 62.62 ks and 62.64 ks, respectively, and for the EPIC-PN, the exposure time is 54.82 ks. A point-like source is detected at the position of SN 2009ip with significance of 4.5σ (for EPIC-PN) and a rate of $(2.7 \pm 0.3) \times 10^{-3}$ cps in a region of 10″ around the optical position of SN 2009ip. From 2013 January until April the source was Sun constrained for *Swift*. 10 ks of *Swift*-XRT data obtained on 2013 April 4.5 ($t_{pk} + 183$ days, when SN 2009ip became observable again) showed no detectable X-ray emission at the position of the transient down to a 3σ limit of 4.1×10^{-3} cps (0.3–10 keV).

An *XMM* EPIC-PN spectrum has been extracted with the SAS software selecting photons from a region of 10″ radius to avoid contamination from a nearby source (Figure 9). We model the spectrum with an absorption component (which combines the contribution from the Galaxy and from the SN 2009ip local environment, *tbabs* × *ztbabs* within *Xspec*) and an emission component. Both thermal bremsstrahlung and thermal emission from an optically thin plasma in collisional equilibrium (*Xspec* MEKAL model) can adequately fit the observed spectrum. In both cases we find $kT > 10$ keV and intrinsic hydrogen absorption of $NH_{int} \approx 10^{21}$ cm^{-2}. In the following we assume thermal bremsstrahlung emission with $kT = 60$ keV (this is the typical energy of photons expected from shock break-out from a dense CSM shell; see Section 7.5). We consider a non-thermal power-law emission model unlikely given the very hard

best-fitting photon index of $\Gamma = 0.87 \pm 0.15$ we obtain from this spectrum. The Galactic absorption in the direction of SN 2009ip is $N_{\rm H,MW} = 1.2 \times 10^{20}$ cm^{-2} (Kalberla et al. 2005). The best-fitting neutral hydrogen intrinsic absorption is constrained to be $\rm NH_{int} = 0.10^{+0.06}_{-0.05} \times 10^{22}$ cm^{-2}. Using these parameters, the corresponding unabsorbed (absorbed) flux is $(1.9 \pm 0.2) \times 10^{-14}$ erg s^{-1} cm^{-2} ($(1.7 \pm 0.2) \times 10^{-14}$ erg s^{-1} cm^{-2}) in the 0.3–10 keV band. The spectrum is displayed in Figure 10. A *Swift*-XRT spectrum extracted around the peak (-2 days $< t - t_{\rm pk} <$ +13 days, total exposure of 86 ks) can be fit by a thermal bremsstrahlung model, assuming $kT = 60$ keV and $\rm NH_{int} < 3.1 \times 10^{21}$ cm^{-2} at the 3σ c.l. As for *XMM*, we use a 10″ extraction region to avoid contamination from a nearby source (Figure 9). The count-to-flux conversion factor deduced from this spectrum is 3.8×10^{-11} erg s^{-1} cm^{-2} count^{-1} (0.3–10 keV, unabsorbed). We use this factor to calibrate our *Swift*-XRT light-curve. The complete X-ray light-curve is shown in Figure 8.

We note that at the resolution of *XMM* and *Swift*-XRT we cannot exclude the presence of contaminating X-ray sources at a distance $\lesssim$10″. We further investigate this issue constraining the level of the contaminating flux by merging the *Swift*-XRT time intervals that yielded a nondetection at the SN 2009ip position. Using data collected between $t_{\rm pk} - 29$ days and $t_{\rm pk} - 2$ days, complemented by observations taken between $t_{\rm pk} + 29$ days and $t_{\rm pk} + 90$ days, we find evidence for an X-ray source located at R.A. = $22^{\rm h}23^{\rm m}09\overset{\rm s}{.}19$ and decl. = $-28°56'48\overset{''}{.}7$ (J2000), with an uncertainty of $3\overset{''}{.}8$ radius (90% containment), corresponding to 1″ from SN 2009ip. The source is detected at the level of 3.4σ with a PSF, vignetting, and exposure corrected count-rate of $(3.0 \pm 0.9) \times 10^{-4}$ cps (total exposure of 110 ks, 0.3–10 keV energy band). The field is represented in Figure 9, left panel. This source contaminates the reported SN 2009ip flux at the level of $\sim 1.6 \times 10^{-4}$ cps. Adopting the count-to-flux conversion factor above, this translates into a contaminating unabsorbed flux of $\sim 6 \times 10^{-15}$ erg s^{-1} cm^{-2} (luminosity of $\sim 5 \times 10^{38}$ erg s^{-1} at the distance of SN 2009ip), representing ~10% the X-ray luminosity of SN 2009ip at peak. This source does not dominate the X-ray energy release around the peak time.

C.7. Hard X-Ray Observations

Swift-BAT data have been obtained in survey mode (15–150 keV energy range) between 2012 September 4 ($t_{\rm pk} -$ 29 days) and 2013 January 1 ($t_{\rm pk}$ + 90 days). We analyzed the data following standard procedures: sky images and source rates were obtained by processing the data with the BATSURVEY tool adopting standard screening and weighting based on the position of SN 2009ip. Fluxes were derived in the four standard energy channels, 14–24, 24–50, 50–100, and 100–195 keV. We converted the source rates to energy fluxes assuming a typical conversion factor of $(5.9 \pm 1.0) \times 10^{-7}$ erg cm^{-2} s^{-1}/count s^{-1}, estimated assuming a range of different photon indices of a power-law spectrum (Γ = 1–3). In particular, analyzing the data acquired around the optical peak we find evidence for a marginal detection at the level of 3.5σ in the time interval -0.8 days $< t - t_{\rm pk} <$ +0.2 days (corresponding to 2012 October 2.2–3.2). A spectrum extracted in this time interval can be fit by a power-law spectrum with photon index $\Gamma = 1.8 \pm 1.0$ (90% c.l.), leading to a flux of $(2.6 \pm 1.4) \times 10^{-10}$ erg s^{-1} cm^{-2} (90% c.l., 15–150 keV, and a total exposure time of 7.0 ks). We used this spectrum to flux calibrate the 5σ upper limit to the hard X-ray emission from SN 2009ip reported in Section 2.6 ($F < 7 \times 10^{-10}$ erg s^{-1} cm^{-2}).

Table 1
Log of Observed *Swift*-UVOT Spectra

Date (UT)	Time Range (UT)	Obs ID	Exposure (ks)	Roll Angle
2012 Sep 27	09:03:41–14:37:27	31486008	5.1	212.0
2012 Sep 28	13:41:01–16:53:23	31486011	3.4	215.0
2012 Sep 29	10:27:52–12:24:46	31486012	3.3	215.0
2012 Sep 30	05:48:22–17:19:31	32570001	4.9	216.0
2012 Oct 1	01:13:23–19:11:08	32570002	4.0	216.0
2012 Oct 2	14:08:21–22:05:35	31486020	5.3	229.0
2012 Oct 3	02:49:01–15:52:51	32570003	4.4	220.0
2012 Oct 4	09:10:01–14:19:17	32570004	5.1	220.0
2012 Oct 5	09:12:55–15:33:06	32570005	7.2	220.0
2012 Oct 6	04:26:57–11:09:55	32570006	6.7	220.0
2012 Oct 7	07:41:54–08:05:27	32570007	6.2	220.0
2012 Oct 8	07:44:55–12:57:21	32579001	6.2	243.0
2012 Oct 10	03:01:55–12:56:01	32579002	6.5	243.0
2012 Oct 12	06:20:54–11:31:19	32579003	5.7	243.0
2012 Oct 14	04:50:54–06:54:14	32579004	5.8	243.0
2012 Oct 16	06:32:56–11:35:19	32579005	5.7	243.0
2012 Oct 20	08:30:16–13:41:40	32579007	5.3	243.0
2012 Oct 22	09:59:14–13:30:15	32579008	3.5	243.0
2012 Oct 24	13:19:14–17:00:26	32605001	4.3	249.0
2012 Oct 26	10:10:14–13:53:54	32605002	3.7	249.0
2012 Oct 28	08:41:21–09:00:03	32605003	1.1	249.0
2012 Nov 2	17:09:16–19:03:52	32605004	11.3	249.0

C.8. GeV Observations

Fermi-LAT observations have been obtained starting from 2012 September 3 ($t_{\rm pk} - 30$ days) until 2012 October 31 ($t_{\rm pk}$ + 28 days). We note the presence of a data gap between $t_{\rm pk} - 9$ days and $t_{\rm pk} - 2$ days due to target-of-opportunity observations by *Fermi* during that time. We use events between 100 MeV and 10 GeV from the `P7SOURCE_V6` data class (Ackermann et al. 2012), which is well suited for point-source analysis. Contamination from γ-rays produced by cosmic-ray interactions with the Earth's atmosphere is reduced by selecting events arriving at LAT within 100° of the zenith. Each interval is analyzed using a region of interest of 12° radius centered on the position of the source. In each time window, we performed a spectral analysis using the unbinned maximum likelihood algorithm `gtlike`. The background is modeled with two templates for diffuse γ-ray background emission: a Galactic component produced by the interaction of cosmic rays with the gas and interstellar radiation fields of the Milky Way, and an isotropic component that includes both the contribution of the extragalactic diffuse emission and the residual charged-particle backgrounds. The models used for this analysis, `gal_2yearp7v6_v0.fits` and `iso_p7v6source.txt`, are available from the Fermi Science Support Center, http://fermi.gsfc.nasa.gov/ssc/. This analysis uses the *Fermi*-LAT Science Tools, v. 09-28-00. We fix the normalization of the Galactic component but leave the normalization of the isotropic background as a free parameter. We also include the bright source 2FGL J2158.8−3013, located at approximately $5\overset{\circ}{.}48$ from the location of SN 2009ip, and we fixed its parameters according to the values reported in Nolan et al. (2012).

APPENDIX D
OBSERVING LOGS

We provide in this Appendix the observing logs (Tables 1–3) of our observations.

Table 2
Log of Observed Optical Spectra

Date (UT)	Telescope/Inst.	Range (Å)	R ($\lambda/\Delta\lambda$)	Grating (l mm^{-1})	Aperture (arcsec)	Airmass	Exp. Time (s)
Aug 26.83	SALT/RSS	3500–10000	300	300	1.25	2.84	900
Sep 26.75	SALT/RSS	3500–10000	300	300	1.25	1.16	1200
Sep 27.99	Magellan/MagE[a]	3150.0–9400.0	3400	175	1.5	1.25	600
Sep 28.99	Magellan/MagE[b]	3150–9400	3400	175	1.5	1.23	1200
Sep 30.02	VLT/X-shooter	3000–25000	5100–8800	···	1.0/0.9/0.9[c]	1.10	744/556/800[c]
Oct 11.15	KPNO/RCSpec	3080–8760	1200	316	1.5	2.15	1200
Oct 11.93	SALT/RSS	3500–10000	300	300	1.25	1.24	300
Oct 12.16	KPNO/RCSpec	3080–8760	1200	316	1.5	2.09	1200
Oct 12.94	SALT/RSS	3500–10000	300	300	1.25	1.29	300
Oct 13.16	KPNO/RCSpec	5380–8290	2500	632	1.5	2.07	6000
Oct 13.18	FLWO/FAST	3470–7414	2700	300	3.0	2.04	1800
Oct 14.15	KPNO/RCSpec	5380–8290	2500	632	1.5	2.10	3600
Oct 14.17	MMT/Blue Channel	3350–8570	1200	300	1.0	2.03	300
Oct 14.18	MMT/Blue Channel	5860–7160	5000	1200	1.0	2.03	600
Oct 14.21	MMT/Blue Channel	3800–5120	3000	1200	1.0	2.12	900
Oct 14.21	FLWO/FAST	3469–7413	2700	300	3.0	2.07	1800
Oct 15.21	FLWO/FAST	3473–7417	2700	300	3.0	2.08	1800
Oct 15.14	KPNO/RCSpec	5380–8290	2500	632	1.5	2.11	4800
Oct 15.14	MMT/Blue Channel	3350–8570	1200	300	1.0	2.03	300
Oct 16.19	FLWO/FAST	3472–7416	2700	300	3.0	2.05	1500
Oct 17.19	FLWO/FAST	3474–7418	2700	300	3.0	2.04	1602
Oct 20.25	FLWO/FAST	3481–7422	2700	300	3.0	2.20	1500
Oct 21.25	FLWO/FAST	3475–7419	2700	300	3.0	2.80	1500
Oct 22.18	FLWO/FAST	3474–7418	2700	300	3.0	2.04	1500
Oct 23.90	SALT/RSS	3200–9000	1500	900	1.25	1.20	600
Oct 27.89	SALT/RSS	3200–9000	1500	900	1.25	1.21	600
Oct 31.13	VLT/X-shooter	3000–25000	5100–8800	···	1.0/0.9/0.9[c]	1.23	744/556/800[c]
Nov 10.85	SALT/RSS	3300–10500	300	300	1.25	1.25	600
Nov 14.06	MMT/Blue Channel	3320–8540	1200	300	1.0	2.11	900
Nov 14.08	MMT/Blue Channel	5840–7140	5000	1200	1.0	2.06	1000
Nov 14.11	MMT/Blue Channel	3780–5110	3000	1200	1.0	2.04	1500
Nov 17.04	Magellan/IMACS	4200–9300	1300	300	0.7	1.02	2700
Nov 23.81	SALT/RSS	3200–9000	1500	900	1.25	1.25	600
Dec 05.01	Magellan/IMACS	3500–9400	1300	300	0.7	1.25	27000
Dec 14.04	SOAR/GHTS	3930–7985	300	1390	0.84	1.44	1800
Dec 21.07	MMT/Blue Channel	3300–8500	300	740	1.0	2.46	2000
Jan 12.04	Magellan/LDSS3	3780–10500	650	VPH-all	1.0	2.75	1200
Apr 11.39	Magellan/IMACS	4000–10200	1600	300	0.9	1.87	1200

Notes.
[a] Observations were obtained under poor 2″ seeing conditions.
[b] 1″.5 seeing.
[c] Refers to *UBV*, VIS and NIR ranges, respectively.

Table 3
Log of Observed NIR Spectra

Date (UT)	Inst.	Range (Å)	R ($\lambda/\Delta\lambda$)	Grating (l mm^{-1})	Aperture (arcsec)	Airmass	Exp. Time (s)
Sep 27.21	MDM	9700–18000	720	···	0.7	2.00	1600
Sep 29.19	MDM	9700–24300	720	···	0.7	2.00	1600
Sep 30.20	MDM	9700–24300	720	···	0.7	2.00	1600
Nov 05.11	FIRE	8000–27400	500	···	0.6	1.24	761
Nov 19.09	FIRE	8200–25000	6000		0.6	1.28	1200
Nov 25.11	FIRE	8000–27200	500	···	0.6	1.67	1014
Dec 03.04	FIRE	8000–27200	500	···	0.6	1.31	1014

APPENDIX E

DATA TABLES

We provide in this Appendix the data tables (Tables 4–7) of our observations.

Table 4
Swift-UVOT Photometry

Date (days)	v (mag)	Date (days)	b (mag)	Date (days)	u (mag)	Date (days)	$w1$ (mag)	Date (days)	$w2$ (mag)	Date (days)	$m2$ (mag)
84.68[a]	20.50(0.30)	84.68	20.76(0.19)	84.68	20.08(0.17)	84.67	20.48(0.19)	84.68	20.77(0.17)	84.69	20.87(0.23)
1174.88	17.10(0.21)	1174.90	17.29(0.05)	1174.90	16.48(0.06)	1174.89	17.09(0.07)	1174.90	17.85(0.09)	1176.64	17.73(0.09)
1176.64	17.52(0.15)	1176.64	17.24(0.07)	1176.64	16.46(0.07)	1176.63	16.96(0.08)	1176.64	17.86(0.10)	1183.44	18.92(0.12)
1183.44	17.74(0.15)	1183.44	17.62(0.08)	1183.44	17.23(0.09)	1183.43	18.08(0.11)	1183.44	19.09(0.14)	1192.74	20.25(0.22)
1192.77	18.16(0.10)	1190.75	18.39(0.15)	1190.75	17.77(0.12)	1190.75	19.08(0.21)	1192.77	20.31(0.18)	1196.35	12.78(0.04)
1196.24	14.91(0.05)	1192.76	18.13(0.06)	1192.76	17.88(0.07)	1192.76	19.23(0.16)	1196.34	12.83(0.05)	1198.48	12.30(0.04)
1196.31	14.95(0.05)	1196.23	14.81(0.05)	1196.23	13.46(0.05)	1196.34	12.98(0.04)	1197.46	12.66(0.05)	1200.99	12.10(0.04)
1196.37	14.86(0.05)	1196.30	14.75(0.05)	1196.30	13.44(0.05)	1197.47	12.75(0.04)	1197.71	12.52(0.05)	1201.99	12.12(0.04)
1196.45	14.83(0.05)	1196.36	14.77(0.05)	1196.36	13.39(0.05)	1197.70	12.62(0.04)	1198.48	12.42(0.04)	1202.75	12.17(0.04)
1198.48	14.38(0.04)	1196.45	14.74(0.05)	1196.45	13.36(0.05)	1198.47	12.51(0.04)	1198.59	12.43(0.04)	1202.26	12.14(0.04)
1199.66	14.26(0.05)	1197.70	14.39(0.05)	1197.70	12.99(0.05)	1198.61	12.59(0.04)	1199.65	12.32(0.04)	1203.07	12.13(0.04)
1200.99	14.14(0.05)	1198.48	14.28(0.04)	1198.47	12.90(0.04)	1199.47	12.53(0.04)	1200.99	12.20(0.04)	1204.06	12.06(0.04)
1201.99	14.07(0.05)	1199.65	14.11(0.05)	1199.65	12.78(0.04)	1199.65	12.41(0.04)	1201.99	12.19(0.04)	1206.13	12.04(0.04)
1202.26	14.11(0.05)	1200.98	13.94(0.05)	1200.98	12.65(0.04)	1200.98	12.30(0.04)	1201.38	12.23(0.04)	1208.68	12.30(0.04)
1203.06	14.10(0.05)	1201.98	13.98(0.05)	1201.98	12.61(0.04)	1201.98	12.31(0.04)	1202.26	12.21(0.04)	1210.07	12.47(0.04)
1204.05	13.91(0.05)	1202.25	13.96(0.05)	1200.47	12.72(0.04)	1202.25	12.31(0.04)	1203.06	12.23(0.04)	1212.20	12.58(0.04)
1206.13	13.88(0.05)	1203.06	13.96(0.05)	1202.25	12.64(0.04)	1203.06	12.30(0.04)	1200.49	12.26(0.04)	1214.14	12.71(0.04)
1208.67	13.92(0.05)	1203.32	13.96(0.05)	1203.06	12.63(0.04)	1204.05	12.22(0.04)	1201.43	12.23(0.04)	1216.21	13.16(0.04)
1210.06	13.88(0.05)	1204.05	13.84(0.05)	1203.12	12.67(0.04)	1206.12	12.17(0.04)	1203.27	12.27(0.04)	1216.41	13.20(0.06)
1212.20	13.95(0.05)	1204.52	13.76(0.13)	1203.32	12.63(0.06)	1208.67	12.44(0.04)	1204.05	12.16(0.04)	1218.83	13.88(0.04)
1214.14	13.93(0.05)	1205.52	13.73(0.11)	1203.39	12.67(0.06)	1210.06	12.55(0.04)	1204.50	12.13(0.04)	1220.55	14.22(0.04)
1216.21	14.13(0.05)	1206.12	13.75(0.05)	1204.05	12.60(0.04)	1212.20	12.69(0.04)	1205.53	12.13(0.04)	1222.29	14.49(0.04)
1218.83	14.30(0.05)	1208.67	13.86(0.05)	1204.38	12.56(0.04)	1214.13	12.77(0.04)	1206.12	12.14(0.04)	1222.41	14.49(0.05)
1220.55	14.30(0.05)	1210.06	13.91(0.05)	1205.38	12.57(0.04)	1218.82	13.71(0.04)	1206.33	12.18(0.04)	1224.49	14.82(0.04)
1222.29	14.43(0.05)	1212.20	13.91(0.05)	1205.52	12.54(0.04)	1220.55	13.95(0.04)	1208.67	12.47(0.04)	1226.49	15.20(0.05)
1224.49	14.46(0.05)	1214.14	13.97(0.05)	1205.65	12.56(0.04)	1222.28	14.18(0.04)	1207.44	12.30(0.04)	1226.23	15.16(0.05)
1226.23	14.75(0.06)	1216.27	14.18(0.07)	1206.12	12.50(0.04)	1224.49	14.40(0.04)	1208.44	12.45(0.04)	1228.71	15.64(0.05)
1228.71	15.01(0.06)	1218.83	14.39(0.05)	1206.25	12.51(0.04)	1226.23	14.75(0.05)	1210.34	12.70(0.04)	1230.38	15.92(0.06)
1230.38	15.23(0.07)	1220.55	14.44(0.05)	1208.39	12.63(0.04)	1228.70	15.30(0.05)	1210.06	12.65(0.04)	1232.86	16.21(0.06)
1232.86	15.09(0.06)	1222.29	14.57(0.05)	1208.52	12.60(0.06)	1230.37	15.48(0.06)	1212.20	12.80(0.04)	1234.41	16.21(0.05)
1233.98	14.85(0.09)	1224.49	14.68(0.05)	1208.52	12.61(0.04)	1232.85	15.64(0.06)	1214.14	12.94(0.04)	1234.98	16.18(0.08)
1234.98	14.86(0.09)	1226.23	14.94(0.05)	1208.67	12.63(0.04)	1234.48	15.52(0.06)	1216.21	13.44(0.04)	1236.18	16.13(0.06)
1236.21	14.95(0.05)	1228.71	15.25(0.06)	1210.06	12.80(0.04)	1236.21	15.53(0.05)	1216.47	13.50(0.04)	1238.09	16.31(0.05)
1238.09	15.16(0.05)	1230.37	15.50(0.06)	1210.19	12.75(0.04)	1238.08	15.72(0.05)	1218.83	14.22(0.04)	1240.06	16.58(0.06)
1240.06	15.34(0.06)	1232.85	15.38(0.06)	1210.46	12.75(0.04)	1240.09	16.01(0.05)	1212.38	12.82(0.04)	1242.30	16.93(0.06)
1242.29	15.68(0.06)	1234.48	15.16(0.06)	1212.20	12.76(0.04)	1242.29	16.27(0.05)	1214.25	12.97(0.04)	1242.30	16.93(0.06)
1244.43	15.88(0.06)	1236.18	15.25(0.06)	1212.33	12.78(0.06)	1244.46	16.63(0.09)	1216.39	13.47(0.04)	1244.43	17.28(0.07)
1246.91	16.00(0.06)	1238.08	15.40(0.05)	1212.33	12.80(0.04)	1246.93	16.94(0.08)	1220.47	14.59(0.04)	1246.94	17.39(0.08)
1248.05	15.83(0.06)	1240.05	15.73(0.05)	1212.46	12.81(0.04)	1248.04	16.88(0.07)	1222.50	14.84(0.04)	1248.05	17.57(0.07)
1250.05	16.04(0.07)	1242.29	16.07(0.05)	1214.14	12.84(0.04)	1250.04	17.05(0.08)	1220.55	14.58(0.04)	1250.05	17.85(0.08)
1252.59	16.17(0.07)	1244.46	16.23(0.08)	1216.20	13.09(0.04)	1252.59	17.34(0.08)	1222.29	14.86(0.04)	1252.59	18.32(0.10)
1254.09	16.33(0.06)	1246.91	16.42(0.06)	1216.27	13.05(0.06)	1254.09	17.50(0.07)	1224.49	15.19(0.05)	1254.09	18.32(0.08)
1256.70	16.32(0.09)	1248.04	16.33(0.06)	1216.27	13.07(0.04)	1256.66	17.83(0.09)	1226.23	15.54(0.06)	1256.70	18.57(0.13)
1258.53	16.42(0.07)	1250.01	16.47(0.07)	1216.40	13.06(0.06)	1258.52	17.93(0.09)	1224.64	15.21(0.04)	1258.54	18.78(0.10)
1260.34	16.45(0.07)	1252.59	16.80(0.06)	1216.41	13.09(0.04)	1260.33	18.04(0.09)	1226.44	15.56(0.06)	1260.34	18.65(0.09)
1262.21	16.41(0.06)	1254.09	16.85(0.06)	1218.82	13.48(0.04)	1262.20	18.42(0.11)	1228.71	16.10(0.06)	1262.21	18.95(0.11)
1264.61	16.60(0.07)	1256.66	17.00(0.06)	1220.55	13.66(0.04)	1264.60	18.32(0.11)	1230.37	16.32(0.06)	1264.61	18.99(0.12)
1266.15	16.71(0.07)	1258.53	17.16(0.06)	1220.45	13.69(0.04)	1266.14	18.41(0.11)	1232.86	16.55(0.06)	1266.15	19.28(0.13)
1268.66	17.00(0.08)	1260.30	17.20(0.08)	1222.29	13.75(0.04)	1268.66	18.73(0.13)	1233.79	16.48(0.05)	1268.66	19.43(0.14)
1270.35	17.28(0.10)	1262.20	17.11(0.06)	1224.62	14.02(0.04)	1270.34	18.70(0.14)	1228.38	15.94(0.07)	1271.32	19.77(0.15)
1272.26	17.41(0.11)	1264.61	17.34(0.07)	1224.49	14.02(0.04)	1272.25	18.85(0.14)	1234.48	16.52(0.07)	1275.20	20.00(0.16)
1274.56	17.94(0.14)	1266.14	17.55(0.07)	1226.23	14.29(0.04)	1274.55	19.05(0.16)	1234.26	16.50(0.04)	1280.35	19.84(0.18)
1276.23	18.18(0.17)	1268.66	18.04(0.09)	1228.71	14.85(0.05)	1276.22	19.16(0.17)	1236.21	16.51(0.05)	1286.55	20.00(0.15)
1278.40	18.29(0.27)	1270.35	18.00(0.09)	1228.36	14.81(0.04)	1278.39	19.42(0.30)	1238.08	16.70(0.05)	1292.40	20.31(0.16)
1280.31	18.46(0.17)	1272.25	18.35(0.10)	1230.37	15.04(0.05)	1280.30	19.64(0.21)	1240.05	17.00(0.06)	1387.30	>21.90
1282.15	18.51(0.20)	1274.55	18.95(0.16)	1232.85	14.99(0.05)	1282.14	19.78(0.27)	1242.29	17.36(0.06)		
1284.24	18.70(0.20)	1276.23	19.05(0.17)	1233.98	14.90(0.08)	1285.14	19.78(0.19)	1244.43	17.71(0.07)		
1286.08	18.67(0.25)	1279.40	19.35(0.15)	1234.98	14.77(0.07)	1290.68	20.10(0.24)	1246.94	17.82(0.10)		
1290.69	18.72(0.18)	1283.17	19.15(0.13)	1236.18	14.87(0.05)	1294.46	19.66(0.18)	1248.05	17.87(0.08)		
1294.47	18.84(0.22)	1287.48	19.48(0.18)	1238.08	15.06(0.05)	1387.30	21.12(0.33)	1250.04	18.18(0.09)		
1387.30	20.18(0.42)	1291.36	19.44(0.20)	1240.05	15.43(0.05)			1252.59	18.49(0.10)		
		1294.46	19.61(0.20)	1242.29	15.82(0.05)			1254.09	18.72(0.10)		
		1387.30	20.32(0.20)	1244.43	16.13(0.06)			1256.66	18.86(0.14)		
				1246.91	16.23(0.06)			1258.53	19.01(0.12)		
				1248.04	16.18(0.06)			1260.34	19.27(0.13)		

Table 4
(Continued)

Date (days)	v (mag)	Date (days)	b (mag)	Date (days)	u (mag)	Date (days)	$w1$ (mag)	Date (days)	$w2$ (mag)	Date (days)	$m2$ (mag)
				1250.04	16.44(0.07)			1262.20	19.17(0.12)		
				1252.59	16.75(0.07)			1264.61	19.27(0.14)		
				1254.09	17.07(0.07)			1266.14	19.46(0.15)		
				1256.66	17.30(0.09)			1268.66	19.45(0.15)		
				1258.53	17.24(0.09)			1271.32	19.82(0.17)		
				1260.33	17.30(0.08)			1275.19	20.11(0.18)		
				1262.20	17.26(0.08)			1280.34	20.33(0.18)		
				1264.61	17.41(0.09)			1285.14	20.40(0.20)		
				1266.14	17.67(0.10)			1290.69	20.55(0.21)		
				1268.66	18.11(0.12)			1294.46	20.54(0.22)		
				1387.30	20.88(0.38)			1387.30	21.56(0.30)		

Note. [a] Dates are in MJD-55000 (days).

Table 5
R- and *I*-Band Photometry

Date (MJD)	R (mag)	Date (MJD)	I (mag)
56181.25	16.54(0.04)	56181.25	16.55(0.07)
56194.25	17.08(0.06)	56194.25	17.82(0.09)
56199.50	14.01(0.01)	56197.00	14.43(0.13)
56201.50	13.86(0.01)	56198.00	14.17(0.07)
56204.50	13.70(0.01)	56199.25	13.94(0.06)
56205.50	13.66(0.01)	56200.00	13.97(0.06)
56206.50	13.65(0.01)	56201.00	13.89(0.04)
56209.00	13.70(0.04)	56202.00	13.79(0.08)
56209.50	13.70(0.01)	56203.00	13.86(0.08)
56210.50	13.71(0.01)	56204.00	13.77(0.07)
56215.50	13.75(0.01)	56205.00	13.69(0.07)
56218.50	13.95(0.01)	56206.00	13.65(0.05)
56219.50	14.01(0.01)	56208.00	13.67(0.07)
56220.50	14.04(0.01)	56209.00	13.66(0.07)
56221.50	14.04(0.03)	56209.25	13.60(0.09)
56223.50	14.17(0.02)	56210.00	13.69(0.07)
56224.50	14.22(0.01)	56211.00	13.59(0.07)
56226.50	14.43(0.01)	56212.00	13.65(0.06)
56226.50	14.40(0.03)	56213.00	13.56(0.10)
56227.50	14.54(0.02)	56214.00	13.56(0.07)
56228.50	14.65(0.02)	56215.25	13.69(0.09)
56234.50	14.59(0.04)	56216.00	13.63(0.08)
56238.50	14.78(0.05)	56217.00	13.74(0.09)
56238.50	14.78(0.01)	56218.00	13.89(0.08)
56239.50	14.87(0.02)	56219.00	13.83(0.06)
56240.50	14.98(0.04)	56220.00	13.83(0.08)
56240.50	14.98(0.02)	56221.00	13.90(0.10)
56242.50	15.15(0.02)	56222.00	14.00(0.07)
56245.50	15.34(0.02)	56223.00	14.04(0.13)
56246.50	15.36(0.03)	56224.00	14.16(0.10)
56247.50	15.36(0.08)	56225.00	14.14(0.06)
56247.50	15.37(0.02)	56226.00	14.19(0.07)
56248.00	15.37(0.04)	56229.00	14.44(0.12)
56248.50	15.38(0.03)	56230.00	14.77(0.09)
56250.50	15.68(0.06)	56231.00	14.55(0.09)
		56233.00	14.52(0.10)
		56234.00	14.44(0.08)
		56235.00	14.53(0.08)
		56236.00	14.36(0.06)
		56237.00	14.43(0.07)
		56238.00	14.60(0.12)
		56239.00	14.74(0.08)
		56240.00	14.70(0.08)
		56241.00	14.90(0.07)
		56242.00	14.98(0.14)

Table 5
(Continued)

Date (MJD)	R (mag)	Date (MJD)	I (mag)
		56243.00	14.97(0.19)
		56244.00	14.99(0.08)
		56245.00	15.14(0.14)
		56246.00	15.26(0.08)
		56247.00	15.19(0.08)
		56248.00	15.20(0.06)
		56248.00	15.10(0.10)
		56249.00	15.00(0.09)
		56250.00	15.26(0.09)
		56251.00	15.19(0.09)

Table 6
NIR Photometry from PAIRITEL

Date (MJD)	J (mag)	Date (MJD)	H (mag)	Date (MJD)	K (mag)
56213.19	13.53(0.01)	56213.19	13.37(0.02)	56213.19	13.25(0.05)
56214.19	13.60(0.01)	56214.19	13.45(0.03)	56214.19	13.20(0.06)
56215.20	13.56(0.01)	56215.20	13.41(0.02)	56215.20	13.24(0.05)
56216.21	13.61(0.02)	56216.21	13.51(0.04)	56216.21	13.23(0.07)
56219.18	13.75(0.03)	56219.18	13.60(0.06)	56219.18	13.44(0.12)
56223.21	13.88(0.01)	56223.21	13.85(0.03)	56226.14	13.76(0.10)
56225.14	13.99(0.02)	56225.14	13.90(0.04)	56227.15	13.66(0.08)
56226.14	14.08(0.02)	56226.14	13.90(0.03)	56228.15	14.02(0.12)
56227.15	14.18(0.02)	56227.15	14.08(0.04)	56230.17	14.11(0.12)
56228.15	14.33(0.02)	56228.15	14.22(0.05)	56231.17	14.19(0.17)
56230.17	14.43(0.03)	56230.17	14.38(0.05)	56232.17	14.10(0.15)
56231.17	14.41(0.02)	56231.17	14.32(0.05)	56236.11	14.01(0.15)
56232.17	14.43(0.03)	56232.17	14.26(0.07)	56237.11	13.86(0.12)
56236.11	14.26(0.03)	56236.11	14.11(0.05)	56238.12	13.71(0.16)
56237.11	14.35(0.02)	56237.11	14.12(0.04)	56243.10	14.35(0.14)
56238.12	14.34(0.02)	56238.12	14.22(0.05)	56255.10	14.93(0.29)
56243.10	14.74(0.04)	56245.13	14.65(0.06)	56266.07	14.82(0.25)
56245.13	14.80(0.03)	56248.09	14.66(0.11)	56267.08	14.53(0.36)
56246.14	14.88(0.10)	56253.11	14.88(0.10)		
56248.09	14.88(0.04)	56255.10	14.82(0.14)		
56253.11	15.07(0.05)	56256.07	15.09(0.19)		
56255.10	15.03(0.05)	56257.08	14.96(0.12)		
56256.07	15.15(0.09)	56266.07	14.94(0.13)		
56257.08	15.15(0.05)	56267.08	15.27(0.15)		
56266.07	15.21(0.08)				
56267.08	15.22(0.06)				

Table 7
Radio and Millimeter Observations

Date (UT Start Time)		F_ν (μJy)	ν (GHz)	Instrument
2012 Sep	26.096	<115.2	21.25	VLA
2012 Sep	26.096	<46.5	8.85	VLA
2012 Sep[a]	26.63	<66	18	ATCA
2012 Sep	27.170	<1000	84.5	CARMA
2012 Oct	16.049	<70.5	21.25	VLA
2012 Oct	17.109	<104.1	21.25	VLA
2012 Oct	17.120	<1500	84.5	CARMA
2012 Oct	26.036	<36.3	8.85	VLA
2012 Nov	6.078	<59.1	21.25	VLA
2012 Nov	12.966	72.6 ± 15.2	8.85	VLA
2012 Dec	1.987	<70.5	21.25	VLA
2012 Dec	2.932	78.3 ± 21.4	8.99	VLA
2013 Mar	9.708	<9.6	9.00	VLA

Notes. Errors are 1σ and upper limits are 3σ.
[a] From Hancock et al. (2012).

REFERENCES

Ackermann, M., Ajello, M., Albert, A., et al. 2012, ApJS, 203, 4
Arnett, W. D. 1982, ApJL, 263, L55
Arnett, W. D., & Meakin, C. 2011a, ApJ, 733, 78
Arnett, W. D., & Meakin, C. 2011b, ApJ, 741, 33
Atwood, W. B., Abdo, A. A., Ackermann, M., et al. 2009, ApJ, 697, 1071
Barkat, Z., Rakavy, G., & Sack, N. 1967, PhRvL, 18, 379
Barthelmy, S. D., Barbier, L. M., Cummings, J. R., et al. 2005, SSRv, 120, 143
Benetti, S., Turatto, M., Cappellaro, E., Danziger, I. J., & Mazzali, P. A. 1999, MNRAS, 305, 811
Berger, E., Foley, R., & Ivans, I. 2009a, ATel, 2184, 1
Berger, E., Soderberg, A. M., Chevalier, R. A., et al. 2009b, ApJ, 699, 1850
Bertin, E., & Arnouts, S. 1996, A&AS, 117, 393
Bloom, J. S., Starr, D. L., Blake, C. H., Skrutskie, M. F., & Falco, E. E. 2006, in ASP Conf. Ser. 351, Astronomical Data Analysis Software and Systems XV, ed. C. Gabriel, C. Arviset, D. Ponz, & S. Enrique (San Francisco, CA: ASP), 751
Bochanski, J. J., Hennawi, J. F., Simcoe, R. A., et al. 2009, PASP, 121, 1409
Bock, D. C.-J., Bolatto, A. D., Hawkins, D. W., et al. 2006, Proc. SPIE, 6267, 626713
Breeveld, A. A., Landsman, W., Holland, S. T., et al. 2011, in AIP Conf. Ser. 1358, Gamma Ray Bursts 2010, ed. J. E. McEnery, J. L. Racusin, & N. Gehrels (Melville, NY: AIP), 373
Brimacombe, J. 2012, ATel, 4423, 1
Brown, P. J., Holland, S. T., Immler, S., et al. 2009, AJ, 137, 4517
Brown, P. J., Roming, P. W. A., Milne, P., et al. 2010, ApJ, 721, 1608
Burrows, D. N., Hill, J. E., Nousek, J. A., et al. 2005, SSRv, 120, 165
Cappellaro, E., Mazzali, P. A., Benetti, S., et al. 1997, A&A, 328, 203
Chandra, P., Chevalier, R. A., Chugai, N., et al. 2012a, ApJ, 755, 110
Chandra, P., Chevalier, R. A., Irwin, C. M., et al. 2012b, ApJL, 750, L2
Chandra, P., & Soderberg, A. 2007, ATel, 1182, 1
Chandra, P., Stockdale, C. J., Chevalier, R. A., et al. 2009, ApJ, 690, 1839
Chatzopoulos, E., Robinson, E. L., & Wheeler, J. C. 2012, ApJ, 755, 95
Chatzopoulos, E., & Wheeler, J. C. 2012, ApJ, 748, 42
Chatzopoulos, E., Wheeler, J. C., & Vinko, J. 2012, ApJ, 746, 121
Chevalier, R. A. 1982, ApJ, 259, 302
Chevalier, R. A. 1984, ApJL, 285, L63
Chevalier, R. A. 1987, Natur, 329, 611
Chevalier, R. A. 2012, ApJL, 752, L2
Chevalier, R. A., & Irwin, C. M. 2011, ApJL, 729, L6
Chevalier, R. A., & Irwin, C. M. 2012, ApJL, 747, L17
Chugai, N. N. 2001, MNRAS, 326, 1448
Chugai, N. N., & Danziger, I. J. 1994, MNRAS, 268, 173
Crowther, P. A., Schnurr, O., Hirschi, R., et al. 2010, MNRAS, 408, 731
Danforth, C. W., Keeney, B. A., Stocke, J. T., Shull, J. M., & Yao, Y. 2010, ApJ, 720, 976
Davidson, K. 1987, ApJ, 317, 760
Davidson, K., & Humphreys, R. M. 1997, ARA&A, 35, 1
Davidson, K., & Humphreys, R. M. (ed.) 2012, in Eta Carinae and the Supernova Impostors (Astrophysics and Space Science Library, Vol. 384), 43
Dessart, L., Hillier, D. J., Gezari, S., Basa, S., & Matheson, T. 2009, MNRAS, 394, 21
Dessart, L., Livne, E., & Waldman, R. 2010, MNRAS, 405, 2113
D'Odorico, S., Dekker, H., Mazzoleni, R., et al. 2006, Proc. SPIE, 6269, 626933
Draine, B. T., & Salpeter, E. E. 1979, ApJ, 231, 438
Drake, A. J., Howerton, S., McNaught, R., et al. 2012, ATel, 4334, 1
Dressler, A., Hare, T., Bigelow, B. C., & Osip, D. J. 2006, Proc. SPIE, 6269, 62690F
Dwek, E., Becklin, E. E., Brown, R. H., et al. 1983, ApJ, 274, 168
Ekström, S., Georgy, C., Eggenberger, P., et al. 2012, A&A, 537, A146
Fabian, A. C., & Terlevich, R. 1996, MNRAS, 280, L5
Fabricant, D., Cheimets, P., Caldwell, N., & Geary, J. 1998, PASP, 110, 79
Fassia, A., Meikle, W. P. S., Vacca, W. D., et al. 2000, MNRAS, 318, 1093
Foley, R. J., Berger, E., Fox, O., et al. 2011, ApJ, 732, 32
Foley, R. J., Kromer, M., Howie Marion, G., et al. 2012, ApJL, 753, L5
Fox, O. D., Chevalier, R. A., Skrutskie, M. F., et al. 2011, ApJ, 741, 7
Fox, O. D., Filippenko, A. V., Skrutskie, M. F., et al. 2013, AJ, 146, 2
Fraser, M., Inserra, C., Jerkstrand, A., et al. 2013, MNRAS, 433, 1312
Frew, D. J. 2004, JAD, 10, 6
Friedman, A. S. 2012, PhD thesis, Harvard Univ.
Gal-Yam, A., Leonard, D. C., Fox, D. B., et al. 2007, ApJ, 656, 372
Gal-Yam, A., Mazzali, P., Ofek, E. O., et al. 2009, Natur, 462, 624
Gall, C., Hjorth, J., & Leloudas, G. 2012, ATel, 4454, 1
Georgy, C., Ekström, S., Meynet, G., et al. 2012, A&A, 542, A29
Georgy, C., Meynet, G., & Maeder, A. 2011, A&A, 527, A52
Ginzburg, S., & Balberg, S. 2012, ApJ, 757, 178
Greisen, E. W. 2003, in Information Handling in Astronomy—Historical Vistas, 285, ed. A. Heck (Dordrecht: Kluwer), 109
Guzik, J. A. 2005, in ASP Conf. Ser. 332, The Fate of the Most Massive Stars, ed. R. Humphreys & K. Stanek (San Francisco, CA: ASP), 204
Hancock, P., Bannister, K., & Bell, M. 2012, ATel, 4434, 1
Hodgkin, S. T., Irwin, M. J., Hewett, P. C., & Warren, S. J. 2009, MNRAS, 394, 675
Houck, J. C., Bregman, J. N., Chevalier, R. A., & Tomisaka, K. 1998, ApJ, 493, 431
Hsiao, E. Y., Marion, G. H., Phillips, M. M., et al. 2013, ApJ, 766, 72
Humphreys, R. M., & Davidson, K. 1994, PASP, 106, 1025
Humphreys, R. M., Davidson, K., Jones, T. J., et al. 2012, ApJ, 760, 93
Kalberla, P. M. W., Burton, W. B., Hartmann, D., et al. 2005, A&A, 440, 775
Katz, B., Sapir, N., & Waxman, E. 2011, arXiv:1106.1898
Kelly, P. L., & Kirshner, R. P. 2012, ApJ, 759, 107
Kiewe, M., Gal-Yam, A., Arcavi, I., et al. 2012, ApJ, 744, 10
Kochanek, C. S., Beacom, J. F., Kistler, M. D., et al. 2008, ApJ, 684, 1336
Kochanek, C. S., Szczygiel, D. M., & Stanek, K. Z. 2011, ApJ, 737, 76
Lauberts, A., & Valentijn, E. A. 1989, Msngr, 56, 31
Leonard, D. C., Filippenko, A. V., Gates, E. L., et al. 2002, PASP, 114, 35
Levesque, E. M., Stringfellow, G. S., Ginsburg, A. G., Bally, J., & Keeney, B. A. 2012, arXiv:1211.4577
Li, W., Smith, N., Miller, A. A., & Filippenko, A. V. 2009, ATel, 2212, 1
Lomb, N. R. 1976, Ap&SS, 39, 447
Maeder, A. 2002, A&A, 392, 575
Maeder, A., & Meynet, G. 2000, A&A, 361, 159
Margutti, R., Soderberg, A., Chornock, R., & Foley, R. 2012, ATel, 4425, 1
Martin, J. C., Hambsch, F.-J., Margutti, R., et al. 2013, arXiv:1308.3682
Massey, P., Morrell, N. I., Neugent, K. F., et al. 2012, ApJ, 748, 96
Matheson, T., Blondin, S., Foley, R. J., et al. 2005, AJ, 129, 2352
Mauerhan, J. C., Smith, N., Filippenko, A. V., et al. 2013, MNRAS, 430, 1801
Maza, J., Hamuy, M., Antezana, R., et al. 2009, CBET, 1928, 1
Meakin, C. A. 2006, PhD thesis, Univ. Arizona, Arizona
Meakin, C. A., & Arnett, D. 2007, ApJ, 667, 448
Miller, A. A., Li, W., Nugent, P. E., et al. 2009, ATel, 2183, 1
Modigliani, A., Goldoni, P., Royer, F., et al. 2010, Proc. SPIE, 7737, 773728
Moran, S. M., Heckman, T. M., Kauffmann, G., et al. 2012, ApJ, 745, 66
Murase, K., Thompson, T. A., Lacki, B. C., & Beacom, J. F. 2011, PhRvD, 84, 043003
Nakar, E., & Sari, R. 2010, ApJ, 725, 904
Nolan, P. L., Abdo, A. A., Ackermann, M., et al. 2012, ApJS, 199, 31
Nozawa, T., Kozasa, T., Tominaga, N., et al. 2008, ApJ, 684, 1343
Ofek, E. O., Fox, D., Cenko, S. B., et al. 2013a, ApJ, 763, 42
Ofek, E. O., Rabinak, I., Neill, J. D., et al. 2010, ApJ, 724, 1396
Ofek, E. O., Sullivan, M., Cenko, S. B., et al. 2013b, Natur, 494, 65
Owocki, S. P., & Shaviv, N. J. 2012, in Astrophysics and Space Science Library, Vol. 384, Eta Carinae and the Supernova Impostors, ed. K. Davidson & R. M. Humphreys, 275
Palmer, D. M. 2009, ApJ, 695, 496
Pastorello, A., Cappellaro, E., Inserra, C., et al. 2013, ApJ, 767, 1
Pastorello, A., Sauer, D., Taubenberger, S., et al. 2006, MNRAS, 370, 1752
Pearce, G., Turner, K., & Rushworth, C. G. 1992, Ap&SS, 196, 337
Perley, R. A., Chandler, C. J., Butler, B. J., & Wrobel, J. M. 2011, ApJL, 739, L1
Pettini, M., & Pagel, B. E. J. 2004, MNRAS, 348, L59
Poole, T. S., Breeveld, A. A., Page, M. J., et al. 2008, MNRAS, 383, 627
Pooley, D., Immler, S., & Filippenko, A. V. 2007, ATel, 1023, 1
Pooley, D., Lewin, W. H. G., Fox, D. W., et al. 2002, ApJ, 572, 932
Prieto, J. L., Brimacombe, J., Drake, A. J., & Howerton, S. 2013, ApJL, 763, L27
Prieto, J. L., Garnavich, P. M., Phillips, M. M., et al. 2007, arXiv:0706.4088
Quataert, E., & Shiode, J. 2012, MNRAS, 423, L92
Quimby, R. M., Wheeler, J. C., Höflich, P., et al. 2007, ApJ, 666, 1093
Ricker, P. M., & Taam, R. E. 2012, ApJ, 746, 74
Roming, P. W. A., Kennedy, T. E., Mason, K. O., et al. 2005, SSRv, 120, 95
Roming, P. W. A., Pritchard, T. A., Prieto, J. L., et al. 2012, ApJ, 751, 92
Sahu, D. K., Anupama, G. C., Srividya, S., & Muneer, S. 2006, MNRAS, 372, 1315
Sanders, N. E., Soderberg, A. M., Levesque, E. M., et al. 2012, ApJ, 758, 132
Scargle, J. D. 1982, ApJ, 263, 835
Schaller, G., Schaerer, D., Meynet, G., & Maeder, A. 1992, A&AS, 96, 269
Schlegel, D. J., Finkbeiner, D. P., & Davis, M. 1998, ApJ, 500, 525
Schlegel, E. M. 1990, MNRAS, 244, 269
Schmidt, G. D., Weymann, R. J., & Foltz, C. B. 1989, PASP, 101, 713
Shiode, J. H., & Quataert, E. 2013, arXiv:1308.5978
Shull, J. M., France, K., Danforth, C. W., Smith, B., & Tumlinson, J. 2010, ApJ, 722, 1312

Simcoe, R. A., Burgasser, A. J., Schechter, P. L., et al. 2013, PASP, 125, 270
Smartt, S. J. 2009, ARA&A, 47, 63
Smith, I. A., Ryder, S. D., Böttcher, M., et al. 2007, ApJ, 669, 1130
Smith, N., Chornock, R., Silverman, J. M., Filippenko, A. V., & Foley, R. J. 2010a, ApJ, 709, 856
Smith, N., Foley, R. J., & Filippenko, A. V. 2008, ApJ, 680, 568
Smith, N., & Frew, D. J. 2011, MNRAS, 415, 2009
Smith, N., & Mauerhan, J. 2012, ATel, 4412, 1
Smith, N., Mauerhan, J. C., Kasliwal, M. M., & Burgasser, A. J. 2013, MNRAS, 434, 2721
Smith, N., Miller, A., Li, W., et al. 2010b, AJ, 139, 1451
Smith, N., & Owocki, S. P. 2006, ApJL, 645, L45
Smith, N., Silverman, J. M., Filippenko, A. V., et al. 2012, AJ, 143, 17
Soker, N. 2013, ApJL, 764, L6
Soker, N., & Kashi, A. 2013, ApJL, 764, L6
Stoll, R., Prieto, J. L., Stanek, K. Z., & Pogge, R. W. 2013, ApJ, 773, 12
Stritzinger, M., Taddia, F., Fransson, C., et al. 2012, ApJ, 756, 173
Sutherland, P. G., & Wheeler, J. C. 1984, ApJ, 280, 282
Svirski, G., Nakar, E., & Sari, R. 2012, ApJ, 759, 108
Vacca, W. D., Cushing, M. C., & Rayner, J. T. 2003, PASP, 115, 389
Valenti, S., Benetti, S., Cappellaro, E., et al. 2008, MNRAS, 383, 1485
Van Dyk, S. D., & Matheson, T. 2012, ApJ, 746, 179
van Dyk, S. D., Weiler, K. W., Sramek, R. A., & Panagia, N. 1993, ApJL, 419, L69
van Marle, A. J., Smith, N., Owocki, S. P., & van Veelen, B. 2010, MNRAS, 407, 2305
Werk, J. K., Putman, M. E., Meurer, G. R., & Santiago-Figueroa, N. 2011, ApJ, 735, 71
Wood-Vasey, W. M., Friedman, A. S., Bloom, J. S., et al. 2008, ApJ, 689, 377
Woosley, S. E., Blinnikov, S., & Heger, A. 2007, Natur, 450, 390
Wright, A. E., & Barlow, M. J. 1975, MNRAS, 170, 41
Yoon, S.-C., Dierks, A., & Langer, N. 2012, A&A, 542, A113
Zampieri, L., Mucciarelli, P., Pastorello, A., et al. 2005, MNRAS, 364, 1419